To the Graduate Council:

I am submitting herewith a dissertation written by Jianyi Wang entitled "Theoretical Aspects of ionization in Ion-Atom Collisions". I have examined the final copy of this dissertation for form and content and recommend that it be accepted in partial fullfillment of the requirements for the degree of the Doctor of Philosophy, with a major in physics.

Joachim Burgdörfer, Major Professor

We have read this dissertation
and recommend its acceptance:

Accepted for the Council:

Associate Vice Chancellor
and Dean of The Graduate School

Theoretical Aspects of Ionization in Ion-Atom Collisions

A Dissertation
Presented for the
Doctor of Philosophy
Degree
University of Tennessee, Knoxville

Jianyi Wang
December, 1991

Acknowledgements

I would like to express my deep gratitude to Dr. Joachim Burgdörfer for serving as my thesis advisor and for introducing me to the theory of atomic collisions and various related fields. He has always been open, frank, and available for help, no matter when or where the need for help arose. Discussions at critical points have been invaluable in steering me in the right direction. At the same time I have been given the freedom to explore and to discover on my own. I could not imagine a better working environment anywhere.

I would also like to thank the distinguished members on my committee Dr. John Bloor, Dr. Edward Harris, Dr. Lee Riedinger, Dr. Ivan Sellin, and Dr. Chia Shih for their effort and support in the progress of the thesis. I wish to thank Dr. Carlos Reinhold for the successful collaboration on several aspects of research presented in this thesis. I would like to thank Jörg Müller and Xiazhou Yang for interactions that have formed an important part of my learning process. I sincerely appreciate helpful conversations with Dr. Lars Andersson, Dr. Marianne Breinig, Dr. Robert DeSerio, and Dr. Stuart Elston during the course of my stay.

I wish to thank my wife Huihua for her support and endurance while bearing the difficult task of bringing up our son Greg and keeping me well fed. I also wish to thank my parents for their strong spiritual support throughout my stay abroad.

At last but not least, I gratefully acknowledge the University of Tennessee and Lanzhou University (PR China) for establishing an exchange program coordinated by Dr. Lee Riedinger (UT) and Dr. Jingye Zhang (LU), under which I had the opportunity to study at this university. Financial support from the National Science Foundation and the Science Alliance is gratefully acknowledged. Finally I would like to express my appreciation for the hospitality of Oak Ridge National Laboratory where part of the work has been performed.

Abstract

We present theoretical studies of electron emission spectra resulting from ionizing collisions between an ion (or atom) and an atom. Mechanisms for ionization are discussed and analyzed for slow and fast collisions and for two different collision systems.

In the first collision system, we consider an exactly solvable three-body model in which an electron moves in the field of two centers of zero range potentials travelling at constant speeds. The exact electron emission spectrum shows two important features:
(a) We find evidence for the existence of the so-called "$v/2$" (or ridge) electrons at intermediate collision speed. These electrons are emitted with about half the speed of the incident ion. It is shown that they are due to promotion to the continuum of the molecular orbitals. $v/2$ electron emission is strongly influenced by the relative interaction strengths of the electron with the two centers as a function of the the charge asymmetry parameter Z_P/Z_T.
(b) For fast collisions multiple scattering peaks can be seen to be a dominant feature in the ionization spectrum. Three-body effects are found to be responsible for generation of the peaks.

In the second collision system we study the ionization spectrum at large ejection angles resulting from electron loss by the incident ions (atoms). The ionization spectrum is shown to be composed of two parts: one is caused by the interaction of the projectile electron with the mean field of the target core and the other by explicit electron-electron interaction. Mean field ionization is treated in an impulse approximation. It is shown that proper treatment of the off-energy-shell scattering matrix element is required to describe experimental data. For the correlated ionization we use the concept of double scattering represented by a second Born approximation. We show that this two-step mechanism is essential in describing the electron angular and energy distribution, especially on the low energy side of the spectrum for electron loss from atomic hydrogen. For other incident ions (like He^+) we find that in addition to double scattering, three-body effects are also very important. They enhance the electron loss cross section and improve significantly the agreement between theory and experiment.

This thesis is based in part on the following publications: [18–20, 39, 40].

Contents

1 Introduction **1**
- 1.1 Target Ionization 1
- 1.2 Projectile Ionization 4
- 1.3 Plan of the Thesis 6

2 The δ-Model: Static Properties **8**
- 2.1 Introduction 8
- 2.2 The δ-Atom 11
  - 2.2.1 The Green's Functions in One Dimension 12
  - 2.2.2 The Bound State of the δ-Atom 14
  - 2.2.3 The Continuum States of the δ-Atom 17
- 2.3 The δ-Molecule 19
  - 2.3.1 The Bound States of the δ-Molecule 19
  - 2.3.2 The Continuum States of the δ-Molecule 22

3 Dynamical Evolution **24**
- 3.1 General Remarks 24
- 3.2 The Asymptotically Bound Solutions 26
  - 3.2.1 The Entrance Channel 26
  - 3.2.2 The Exit Channels 32
- 3.3 The Asymptotic Continuum Solutions 33
- 3.4 Probability Calculation 35
- 3.5 The δ-Model in 3D 37

4 Ionization Spectra for the δ-Model **38**
- 4.1 Total Probability 38

4.2 Forward and Backward Binary Electrons . . . 43
4.3 Missing Cusp . . . 45
4.4 $v/2$ Electron Emission . . . 47
4.4.1 Mechanism . . . 47
4.4.2 Three-body Effects . . . 54
4.5 Multiple Scattering Peaks . . . 59

5 Projectile Ionization in the Target Mean Field 65
5.1 Overview . . . 65
5.2 Mean Field and Correlation . . . 67
5.3 Approximation Methods for Mean Field Ionization . . . 71
5.3.1 Impulse Approximation . . . 71
5.3.2 On-Shell Approximations . . . 74
5.3.3 Continuum Distorted Wave Method . . . 78
5.3.4 The CTMC Method . . . 80
5.4 Elastic Scattering . . . 81
5.5 Asymmetric Collisions: H^0 and He^+ on Ar . . . 86
5.5.1 Doubly Differential Cross Sections . . . 87
5.5.2 Singly Differential Cross Sections . . . 89
5.5.3 Angular dependence of the peak position . . . 90
5.6 Symmetric Collisions: He^+ on He . . . 93
5.6.1 Two-Center Effects . . . 93
5.6.2 Angular Distribution . . . 96

6 Projectile Ionization by Electron-Electron Interaction 98
6.1 Scattering Correlation . . . 98
6.2 Approximation Method to Correlation . . . 99
6.2.1 Second Born Approximation: Double Scattering . . . 99
6.2.2 Evaluation of Cross Sections . . . 102
6.3 Correlated Ionization for Near Symmetric Collisions: H^0 and He^+ on He . . . 108
6.3.1 H^0 + He . . . 108
6.3.2 He^+ + He . . . 111

6.3.3 Correlated Ionization for heavy targets 113

7 Conclusions **117**

Bibliography **120**

Appendices **129**

A Evaluation of $\frac{\partial\psi}{\partial t}$ and $\frac{\partial^2\psi}{\partial x^2}$ in 3.2.1 **130**

B Second Born Approximation **133**

C Peaking Approximation **136**

D Dalitz Integral **138**

Curriculum Vitae **140**

List of Figures

2.1 Possible Exit Channels of the δ-Model 10
2.2 Wave Function of the δ-Atom 16
2.3 The Energy Level Diagram of the δ-Molecule 20

3.1 Wave Function as A Function of Time 31

4.1 Total Probabilities. 39
4.2 Capture probability as a function of $1/v$. 41
4.3 Ionization Spectrum at $v = 1$. 44
4.4 Missing Cusps 46
4.5 $v/2$ Electron Emission 48
4.6 Dependence of $v/2$ Electron Emission on v 49
4.7 Population of Quasi-molecular States 51
4.8 Ionization Spectrum in 3D 53
4.9 Dependence of $v/2$ Electron Emission on Z_P/Z_T 55
4.10 Peak Position of $v/2$ Emission 56
4.11 Yield of $v/2$ Electron Emission 58
4.12 Multiple Scattering Peaks in 1D 60
4.13 Born Approximation 62
4.14 Multiple Scattering Peaks in 3D 64

5.1 Geometry of Collision System 67
5.2 The Effective Potential 82
5.3 Elastic Scattering Cross Sections 83
5.4 Partial Wave Decomposition 84
5.5 Classical Deflection Function 85
5.6 DDCS for H^0 on Ar 87
5.7 On-Shell Approximations for He^+ + Ar 88

5.8 SDCS for H^0 and He^+ on Ar 90
5.9 Angular Variation of the Peak Position 91
5.10 Anomalous Behavior of Elastic Cross Sections 92
5.11 DDCS of He^+ + He at 180^0 94
5.12 DDCS of He^+ + He at Several Angles 95
5.13 SDCS for He^+ + He 96

6.1 Schematic Diagrams of Multiple Scattering 101
6.2 Closure Approximation 107
6.3 Correlated DI for H^0 + He 109
6.4 Correlated Ionization for He^+ on He 111
6.5 SDCS for He^+ + He Including Correlated DI 112
6.6 Correlated DI for H^0 on Ar 115

Chapter 1

Introduction

1.1 Target Ionization

One of the possible outcomes in ion-atom collisions is the ejection of free electrons. It is called ionization because the atom, after being stripped of electrons, becomes an ion. The study of ionization mechanisms provides detailed information on the dynamical evolution of the collision. It is of fundamental importance in many areas of physics as well as other branches of science.

Consider the following simple ionization process,

$$\mathrm{P}^{Z_P+} + \mathrm{T} \rightarrow \mathrm{P}^{Z_P+} + \mathrm{T}^{+} + e^{-}. \tag{1.1}$$

Eq. (1.1) represents a projectile P of charge $+Z_P$ colliding with a target T. After the collision, the target is ionized with a free electron emitted. Although the fundamental laws of motion and the atomic forces are usually presumed to be well known, the dynamics involved is far more complex than it might seem. In its simplest form, assuming a bare projectile and a single-electron target, we face a three-body problem. No analytical solution to such a general three-body system exists in terms of known functions. One therefore has to invoke various assumptions and approximations depending on the projectile-target system and impact energies under consideration in order to treat the reaction (1.1) theoretically. With these approximations it is possible to calculate the angular and energy distributions of the ejected electrons. These distributions are also known as *doubly differential cross*

sections (DDCS or $d^2\sigma/dE\,d\Omega$). It is this quantity that is often measured in state of the art experiments.

In the case of fast, bare ion impact ionization of atomic targets, the experimentally measured DDCS exhibits several common features [1, 2]. They are characterized in momentum space by three distinct structures on top of a smooth background:

1. A low energy secondary electron peak centered around the target [3]. These electrons are ejected in low lying continuum states of the target nucleus via soft (distant) collisions with the projectile.

2. The electron capture to continuum peak centered around the projectile [4, 5, 6]. Unlike in the usual rearrangement collisions the electron is captured into a continuum state of the projectile instead of a bound state.

3. Binary encounter (BE) electrons resulting from a head-on collision of the target electron with the projectile. The electron acquires a large momentum and travels with up to twice the speed of the projectile in the forward direction.

This traditional picture of the velocity distribution is qualitatively well understood. Recent theoretical studies suggest a possible amendment to that picture at low to intermediate impact energies. Two independent investigations using classical trajectory Monte Carlo [7, 8, 9] and coupled-channel methods [10] have found evidence for an enhancement of the ionization spectrum at about half of the projectile speed v. It is consequently termed $v/2$ electron emission [7, 11]. Since these electrons travel at $v/2$ in the forward direction, they are "in between" the target and the projectile in the momentum space as well as in the coordinate space. They appear to be "stranded" at a point in between the two Coulomb centers without any substantial force acting on the electrons. Another term is therefore the "saddle-point" electrons. The saddle point is the point between the target and the projectile where the force on the ejected electron is zero. For symmetric collisions, the saddle point moves exactly at $v/2$. We point out, however, that both "$v/2$" and "saddle-point" are not to be taken literally. The enhancement does not peak in general exactly at $v/2$ and the electrons are not necessarily related to

the dynamics at the saddle point. It is clearly an indication of a true three-body effect caused by simultaneous interactions of comparable strengths of the electron with the target and the projectile.

The identification of this new mechanism remains to be confirmed by experimental evidence. As of yet, there is little consensus among experiments on the existence of $v/2$ electrons. The first observation of a sharp ridge [11] extending in velocity space from 0 to v for collisions of protons on helium has been later attributed to an experimental artifact due to target-gas background [12]. In another experiment [13, 14] for the same collision system a $v/2$ hump has been observed at 20^0 . Its position has been measured as a function of the nuclear charge of the projectile. The charge dependence of the $v/2$ hump could not be confirmed by other measurements [15]. It is still being debated [16, 17] as to whether the origin of the hump near $v/2$ is purely a kinematic effect due to the data presentation (when the differential cross section is plotted as $d^2\sigma/dv\,d\Omega$ instead of $d^2\sigma/dE\,d\Omega$).

This controversy has motivated us to investigate the ionization near $v/2$ using an exactly solvable model. We shall study the ionization spectra for a one-dimensional (1D) and a three-dimensional (3D, zero impact parameter) ion-atom scattering model problems in which the long-ranged Coulomb potentials are replaced by zero-ranged potentials represented by Dirac delta functions. In the following we shall refer to this model as the $\delta-$model. This model is chosen for two reasons. First, it is one of the few exactly solvable quantum-mechanical three-body problems. When restricted to zero impact parameter, the 3D model problem is, to the author's knowledge, the only three-body problem that yields exact solutions in three-dimensional space. It is therefore possible to study the ionization mechanisms without invoking any approximations which may potentially distort any three-body effect. Considering the small intensity of the $v/2$ electrons as claimed in the experiment, it is of crucial importance that the theoretical description be as accurate as possible. Second, zero-ranged potentials in the $\delta-$model problem represent the opposite extreme to the long-ranged Coulomb interactions. It allows the identification of features specifically related to interactions at short distances, as opposed to post-collisional interactions of the Coulomb type.

The structures embedded in the ionization spectrum are rather rich [18, 19]. At intermediate energies, we find evidence for $v/2$ electrons in this $\delta-$model problem. At high energies, multiple scattering peaks [20] dominate

the spectrum as a result of the electron bouncing forth and back between the two centers.

1.2 Projectile Ionization

Projectile ionization occurs when the projectile carries bound electrons into a collision. Traditionally it is also referred to as electron loss because the emitted electrons are lost by the projectile. We shall use projectile ionization and electron loss interchangeably. Electron loss has been studied both experimentally and theoretically for almost two decades [21, 22, 23, 24]. However, detailed angular and energy distributions of the emitted electrons have been measured only very recently [25, 26, 27]. There are two prominent features present in the DDCS in velocity space:

1. The electron loss to continuum (ELC) cusp [28, 29] centered around the projectile velocity. In the projectile rest frame these electrons mirror the slow secondary electrons emitted in target ionization.

2. The electron loss peak (ELP) [30, 31] centered approximately around v encompassing an angular range from small angles in the forward direction to 180^0 in the backward direction. Qualitatively it can be understood as a result of elastic scattering of electrons initially loosely bound to the projectile (to zeroth order approximation).

It is important to realize the interrelation which exists between projectile ionization and target ionization. If the reference frame is chosen such that the projectile is at rest [30], then projectile ionization becomes target ionization in the usual sense, albeit by a structured particle impact. In particular, the usual binary encounter peak in the forward direction (item 3 on discussion of target ionization) will appear near $\sim v$ in the backward direction in the target rest frame. We can therefore refer to the electron loss peak as the backward binary peak. This interrelation is useful for a unified description of target and projectile ionization. Note that for projectile ionization no prominent electron capture to continuum peak (corresponding to item 2 on discussion of target ionization) appears since the neutral ionizing particle (the target) can not capture electrons as effectively as a Coulomb potential can.

The most important difference between projectile ionization and target ionization lies in the fact that the ionizing particle (the target) is structured

since most target systems consist of neutral atoms or molecules. The simplest projectile ionization is a four-body collision,

$$P^{(Z_P-1)+} + T \rightarrow P^{Z_P+} + e^- + T^*. \tag{1.2}$$

Unlike target ionization (Eq. (1.1)), projectile ionization ((1.2)) can occur with the target being left either in the ground state or in any excited states denoted by T^* (including continuum states, i.e. ionization). One major difficulty for the experimental observation is the separation of projectile electron loss from simultaneously occurring target ionization. Theoretically, the description is complicated by the large number of exit channels resulting from structured particle impact (We will discuss this aspect in detail in a later chapter). That is probably one reason why, after almost twenty years of the first experimental observation of electron loss [21, 22], the theory of projectile ionization is still in a developing stage.

The most prominent feature of projectile ionization is the change of the shape of the loss peak from a ELC cusp in the forward direction to a broad distribution in the backward direction. The shape and magnitude of the ELC cusp has been extensively studied both experimentally and theoretically. Many theoretical calculations have been performed and compared with experimental data. These calculations [32, 33, 34, 35] have provided a qualitative, and many times quantitative, explanation of this experimentally observed feature. Recent studies of projectile electron loss at backward angles have revealed large discrepancies between theory and experiment [25, 36]. Systematic disagreement was observed for the angular distributions of electrons ejected at angles larger than 100^0, with the measurements being consistently higher than the calculations by up to a factor of ≈ 3 for collisions of He^+ with He and Ar [25]. The discrepancy is particularly intriguing considering the good agreement between theory and experiment at small angles where post-collisional distortions are much more important than at backward angles. Electron emission into large angles through a hard binary collision is thought to be one of the simplest mechanisms for ionization for which even classical binary encounter theory has been successfully applied [3]. The investigation of this discrepancy is one of the central aspects of this thesis.

We shall give a theoretical description of the electron loss processes for a hydrogen-like projectile (H^0 , He^+) on He and Ar. The electron loss has in general two components, mean field and correlated ionization [37, 38]. The

former describes the projectile ionization by a screened target core. The latter treats explicitly the interaction between the projectile-electron and the target-electron. For the mean field ionization we formulate an impulse approximation [39] with the exact off-energy-shell transition amplitude in a time-dependent approach. For the correlated ionization, we use the concept of multiple scattering developed in the δ-model problem. It is calculated in a second order Born approximation [40] which includes a single scattering and a double scattering.

In comparing theoretical calculations with experimental data, we find good agreement when the mean field and the correlated ionization are both taken into account.

1.3 Plan of the Thesis

We shall present first the target ionization spectrum of the δ-model problem. In Chapter 2 we will outline the model problem with zero-ranged potentials. The bound and continuum states of the isolated one-center problem (referred to in the following as the "delta atom") will be discussed. We then solve the molecular eigenvalue problem with two centers at a fixed distance and show the existence of binding and antibinding molecular orbitals. In Chapter 3 we present the derivation of the time-evolution of the scattering states in the field of the two moving centers. An expression for the ionization probability will be derived. Some general properties and similarities to the 3D Coulomb problem will be pointed out. In Chapter 4 the ionization spectrum will be presented and the $v/2$ electron component will be identified. This emission mechanism will be discussed in terms of promotion to the continuum via molecular orbitals. We shall also show the existence and give an explanation of multiple scattering peaks in the ionization spectrum.

We then investigate the projectile ionization spectrum. In Chapter 5 we shall derive the impulse approximation for the mean field ionization. We will discuss various forms of on-energy-shell approximations and show their connections to the exact off-energy-shell impulse approximation. Spectra resulting from H^0 and He^+ on Ar will be shown and compared with experimental data. Two-center effects using continuum distorted waves and classical trajectory Monte Carlo methods will also be discussed for more symmetric collisions. Having seen the mean field ionization, we examine in Chapter 6

the role of correlated ionization. A second Born approximation for the latter process will be derived. Cross sections will be calculated for H^0 and He^+ on H, He and Ar. The contributions from single and double collisions will be compared with each other. Finally, the sum of contributions from correlated and mean field ionizations for He^+ on He will be compared with experimental data. Conclusions will be drawn in Chapter 7.

Except where explicitly noted, atomic units (a.u.) [41] are used throughout the thesis. To improve the readability, lengthy derivations will be kept to a minimum necessary for a coherent presentation in the main text. Additional technical details will be given in appendices.

Chapter 2

The δ-Model: Static Properties

2.1 Introduction

The fundamental starting point in solving quantum mechanical scattering problems is to seek solutions to the Schrödinger equation. It is well known that for two-body elastic scattering, a limited number of cases exist which yield exact analytical solutions in both one-dimensional (1D) and three-dimensional (3D) space, e.g. the 1D square-wells and the 3D spheres, the 1D and 3D Coulomb scattering. There are, however, very few exactly-solvable quantal three-body systems in either 1D or 3D space. It is of great importance that such systems be investigated not only for their intrinsic merits, but also for comparison with real systems. Essential ideas as well as delicate details can often be extracted from the exact behavior of these model systems.

One of the much-studied three-body systems consists of a particle interacting with two centers by zero-range potentials. The potential is represented by a Dirac δ function. We shall refer to the potential as the δ-potential. Since the introduction of this δ-potential by Fermi in 1934, it had found wide applications early on in nuclear physics. Breit investigated the scattering of protons by neutrons assuming the interaction to be zero-ranged [42]. This method was also applied to the diffraction of neutrons by crystals by Goldberger *et al.* [43]. Bethe *et al.* [44, 45] considered the photo-disintegration of deuterons using the same potential.

The usefulness of the δ-potential was realized later in atomic physics [46].

Armstrong [47] calculated the photo-detachment cross section for H^- in a way similar to the photo-disintegration of deuterons [44]. Dettmann *et al.* [48] used the δ-potential as a counter-example to disprove the claimed divergence behavior [49] of the Born series in capture collisions. More recently, the δ-potential has been used to simulate the ionization of a bound system in strong electric fields [50, 51] and tunneling through a time-dependent barrier [52]. It is also of interest in connection with nonlinear dynamics.

We are interested in the scattering aspect of the δ-potential as applied to atomic physics, particularly to ionizing collisions. Here one can take advantage of the fact that in ion-atom collisions, the nuclei are much heavier than the electrons. If one is only interested in the electronic processes, the nuclei can be regarded as infinitely heavy (to a very good degree of approximation). The motion of the nuclei proceeds at constant speed along a straight-line trajectory. The interaction between the two nuclei can be neglected because it gives rise only to an irrelevant phase factor [3]. This approach is usually called the semi-classical approximation (SCA). The three-body problem is reduced to an effective one-body problem with a time-dependent Hamiltonian operator. In one dimension the Hamiltonian reads

$$H = -\frac{1}{2}\frac{\partial^2}{\partial x^2} - Z_T\delta(x) - Z_P\delta(x - R(t)). \tag{2.1}$$

Eq. (2.1) represents the Hamiltonian of an "electron" moving in the field of two centers. One center is at the origin and the other at an internuclear distance $R(t) = vt$. Following the conventions in ion-atom collisions, the former will be referred to as the "target" and the latter as the "projectile". In (2.1) the target rest frame has been chosen such that the projectile travels at constant speed v from left to right. The electron interacts with the target and the projectile via an attractive, zero-range potential represented by a Dirac δ function. The strengths of the interactions are determined by the "nuclear charges" of the target (Z_T) and the projectile (Z_P). We shall refer to the system described by Eq. (2.1) as the δ-model.

A number of electronic processes are possible in the δ-model. They are schematically illustrated in Fig. 2.1. At the start of the collision ($t = -\infty, R = -\infty$), the system is prepared in a state in which an electron is bound to the target (Fig. 2.1 (a)). The existence of one bound state in a δ-potential will be shown in the next section. Also note that there exists at least one bound state for any attractive potential in one dimension. The pro-

Before collision

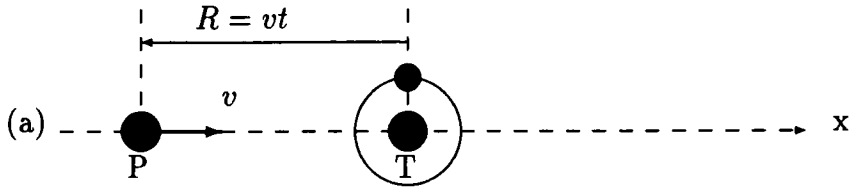

After collision

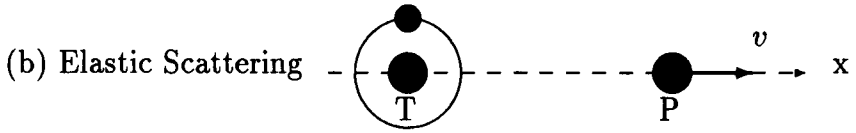

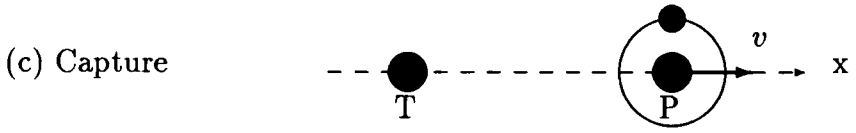

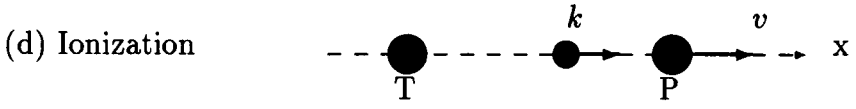

Figure 2.1: Possible Exit Channels of the δ-Model. Note that the motion of the "electron" is strictly one-dimensional. The circular electronic orbit is shown for illustrative purposes only.

jectile approaches the target for $t < 0$. As it reaches the vicinity of the target, significant perturbation of the initial state occurs. After the point of closest approach at $R(t = 0) = 0$, the projectile recedes from the target for $t > 0$ and eventually moves to infinity at the end of the collision ($t = +\infty, R = +\infty$). As a result of the projectile impact, the electron has certain probabilities of remaining bound in the target $P_{elastic}$ (elastic scattering, Fig. 2.1 (b)), being captured by the projectile $P_{capture}$ (Fig. 2.1 (c)), or being ionized $P_{ionization}$ (Fig. 2.1 (d)). Of course the total probability for elastic scattering, capture and ionization must be unity, i.e.

$$P_{elastic} + P_{capture} + P_{ionization} = 1. \tag{2.2}$$

The exact solutions to Eq. (2.1) for asymptotic bound states were first obtained by Zhdanov [53] for the case of $Z_T = Z_P$. The elastic scattering and the capture have been studied by a number of authors. $P_{elastic}$ and $P_{capture}$ have been calculated by Däppen [54] for symmetric collisions $Z_P = Z_T$. Later, Danared [55] has extended the calculations to asymmetric collisions $Z_P \neq Z_T$. Of course $P_{ionization}$ can be readily obtained from (2.2) once $P_{elastic}$ and $P_{capture}$ are known.

Unlike the elastic scattering and the capture probabilities, however, the total ionization probability alone does not give a complete description of the ionization process. More detailed information can be obtained from the momentum distribution of the ejected electron. That distribution, or the ionization spectrum, is what we will calculate and will explain in the following chapters.

In the remainder of this chapter, we discuss the static properties of the isolated δ-potential as well as the "molecule" described by the Hamiltonian operator (2.1) for a fixed R. Similarities between the isolated δ-potential and the hydrogen atom will also be pointed out.

2.2 The δ-Atom

The system consisting of an electron in the field a δ-potential is known as the "delta-hydrogen" atom [56]. We shall simply refer to it as the δ-atom. Its Hamiltonian operator is given by

$$H_{\delta-atom} = -\frac{1}{2}\frac{\partial^2}{\partial x^2} - Z\delta(x) \tag{2.3}$$

where the nuclear charge is denoted by Z. A review of the properties of the δ-atom is presented in this section.

2.2.1 The Green's Functions in One Dimension

Due to the nature of the zero-range potential, it is easiest to solve static problems involving the δ-potentials by the method of Green's functions. We start with the free particle Green's function satisfying the equation

$$\left[-\frac{1}{2}\frac{\partial^2}{\partial x^2} - k^2/2 + i\eta\right] G_0^+(x,x') = \delta(x-x') \tag{2.4}$$

where the momentum k is related to the energy (E) of the particle by $E = k^2/2$, the infinitesimally small η ensures the asymptotic outgoing boundary conditions. With $G_0^+(x,x')$ defined by (2.4), the general solution to the Schrödinger's equation

$$\left[-\frac{1}{2}\frac{\partial^2}{\partial x^2} + V(x)\right] \psi(x) = E\psi(x) \tag{2.5}$$

can be written in the form of an integral equation,

$$\psi(x) = \phi(x) - \int dx' G_0^+(x,x') V(x') \psi(x'). \tag{2.6}$$

In (2.5) and (2.6), $V(x)$ represents a short range but otherwise arbitrary potential. $\phi(x)$ is the solution to the free particle Schrödinger's equation (by setting $V(x) = 0$ in Eq. (2.5)), i.e. a plane wave,

$$\phi(x) = \frac{1}{\sqrt{2\pi}} \exp(ikx). \tag{2.7}$$

$G_0^+(x,x')$ can be determined [57] directly by a Fourier transform on both sides of Eq. (2.4). The Fourier transform of $G_0^+(x,x')$ can be written as

$$G_0^+(x,x') = \int \tilde{G}(\omega,x') \exp(i\omega x) d\omega. \tag{2.8}$$

Substituting (2.8) into (2.4) and using the identity $\delta(x) = \int \exp(i\omega x) d\omega/2\pi$ yields

$$\tilde{G}(\omega,x') = \frac{1}{\pi} \frac{\exp(-i\omega x')}{\omega^2 - k^2 + i\eta}. \tag{2.9}$$

Evaluating Eq. (2.8) with $\tilde{G}(\omega)$ in (2.9) by contour integration and taking into account the outgoing boundary conditions, the following expression can be obtained,

$$G_0^+(x,x') = \frac{1}{\pi}\int d\omega \frac{\exp(i\omega(x-x'))}{\omega^2 - k^2 + i\eta} \tag{2.10}$$

$$= \frac{i}{k}\exp(ik|x-x'|). \tag{2.11}$$

Eq. (2.11) constitutes the free particle Green's function. It will be used in solving the δ-atom problem in next section. The Green's function of the δ-atom can be obtained in analogy to that of the free particle. From the δ-atom Hamiltonian (2.3), one can define the corresponding Green's function G_a^+ as

$$\left[-\frac{1}{2}\frac{\partial^2}{\partial x^2} - Z\delta(x) - k^2/2 + i\eta\right] G_a^+(x,x') = \delta(x-x'). \tag{2.12}$$

Using a Fourier transform similar to (2.8),

$$G_a^+(x,x') = \int \tilde{G}_a(\omega,x')\exp(i\omega x)d\omega \tag{2.13}$$

and noting the two δ functions in (2.12), $\tilde{G}_a(\omega,x')$ can be expressed as

$$\tilde{G}_a(\omega,x') = \frac{1}{\pi}\frac{\exp(-i\omega x') + ZG_a^+(0,x')}{\omega^2 - k^2 + i\eta}. \tag{2.14}$$

The first term in the numerator of (2.14) results from $\delta(x-x')$ in (2.12) and is the same as in (2.9). The second term is due to the additional $-Z\delta(x)$ potential in (2.12). It is a consequence of the identity $\delta(x)G_a^+(x,x') = \delta(x)G_a^+(0,x')$.

With Eq. (2.13) and (2.14), a contour integration can be carried out to obtain the δ-atom Green's function

$$G_a^+(x,x') = \frac{1}{\pi}\int d\omega \frac{\exp(-i\omega x') + ZG_a^+(0,x')}{\omega^2 - k^2 + i\eta}\exp(i\omega x) \tag{2.15}$$

$$= \frac{i}{k}\left[\exp(ik|x-x'|) + ZG_a^+(0,x')\exp(ik|x|)\right] \tag{2.16}$$

$G_a^+(0,x')$ can be solved by setting $x=0$ on both sides of (2.16) and the final result for $G_a^+(x,x')$ reads

$$G_a^+(x,x') = \frac{i}{k}\left[\exp(ik|x-x'|) - \frac{Z}{Z+ik}\exp(ik(|x|+|x'|))\right] \qquad (2.17)$$

$G_a^+(x,x')$ given by (2.17) agrees with that obtained by more involved methods such as summation over the eigenstates of the δ-atom [56].

The δ-atom Green's function G_a^+ shows some remarkable structural resemblance to the more familiar Coulomb Green's functions in both one- and three-dimensions [56, 58]. The Coulomb potential $-Z/x$ is particularly interesting because it satisfies the same dilatation symmetry as the δ-potential, i.e. $V(\lambda x) = V(x)/\lambda$. We quote without proof the Green's function for Coulomb potential $-Z/x$ in asymptotic region ($x > x'$ and $x, x' \to +\infty$) [56]

$$\begin{aligned} G_c^+(x,x') \sim & \frac{i}{k}\times \\ & \left\{\exp\left[ik(x-x') + i\frac{Z}{k}(\ln(kx) - \ln(kx'))\right]\right. \\ & \left. -\frac{\Gamma(1-i\frac{Z}{k})}{\Gamma(1+i\frac{Z}{k})}\exp\left[ik(x+x') + i\frac{Z}{k}(\ln(kx)+\ln(kx'))\right]\right\} \end{aligned} \qquad (2.18)$$

Apart from the logarithmic phases $\exp(i\frac{Z}{k}\ln(kx))$ characteristic of the long-range behavior of Coulomb potentials Eq. (2.18) is structurally the same as (2.17).

2.2.2 The Bound State of the δ-Atom

It is well known that the δ-atom has one bound state [59]. It can be determined in a straight-forward manner using the Green's function.

The solution to the δ-atom Hamiltonian (Eq. (2.3)) follows from Eq. (2.6) with $V(x) = -Z\delta(x)$ and $G_0^+(x,x')$ given by Eq. (2.11). For bound states the wave function must vanish at $x = \pm\infty$, which requires the inhomogeneity $\phi(x)$ in (2.6) to vanish. The bound state wave function $\psi_0(x)$ satisfies

$$\begin{aligned} \psi_0(x) &= -\int dx' \frac{i}{k}\exp(ik|x-x'|)(-Z\delta(x'))\psi_0(x') \\ &= \frac{iZ}{k}\exp(ik|x|)\psi_0(0). \end{aligned} \qquad (2.19)$$

The eigenvalue equation for k can be obtained from Eq. (2.19) by setting $x = 0$, namely,

$$\psi_0(0) = \frac{iZ}{k}\psi_0(0). \tag{2.20}$$

There is only one k value that satisfies (2.20), $k = iZ$. The eigenenergy E_0 and the normalized eigenfunction of the bound state are given by

$$E_0 = k^2/2 = -Z^2/2, \tag{2.21}$$

$$\psi_0(x) = \sqrt{Z}\exp(-Z|x|). \tag{2.22}$$

The eigenenergy E_0 is exactly the same as for the ground state of the hydrogenlike atoms. $\psi_0(x)$ in coordinate space is shown in Fig. 2.2 for the case of $Z = 1$. It decreases exponentially with increasing $|x|$. The first derivative of $\psi_0(x)$ with respect to x is discontinuous at $x = 0$. The eigenfunction of the hydrogen atom also shows the same coordinate dependence upon replacing $|x|$ by $|\vec{r}|$. We may also estimate the diameter of the δ-atom from (2.22) to be about $2/Z$. The orbital speed of the electron can be obtained by using virial theorem

$$2\langle T\rangle - n\langle V\rangle = 0, \tag{2.23}$$

where $\langle T\rangle$ and $\langle V\rangle$ represent the average kinetic and potential energy, respectively. Eq. (2.23) holds for the class of potentials that are n-th order homogeneous in coordinate space, $V(\lambda x) = \lambda^n V(x)$ (dilatation symmetry). Obviously $n = -1$ for both the δ-potential and the Coulomb potential. The average potential of the δ-atom can be calculated as

$$\langle V\rangle = \int \psi_0^*(x)[-Z\delta(x)]\psi_0(x)dx = -Z^2. \tag{2.24}$$

Upon substitution of (2.24) into (2.23), we obtain

$$\langle T\rangle = Z^2/2. \tag{2.25}$$

From the above relation, one can conclude that the orbital speed of the electron in the δ-atom is about Z. The same conclusion is also true for hydrogenlike atoms in the ground state.

The wave function in momentum space is obtained by a Fourier transform of (2.22)

$$\tilde{\psi}_0(p) = \sqrt{\frac{2}{\pi}}\frac{Z^{3/2}}{Z^2 + p^2}. \tag{2.26}$$

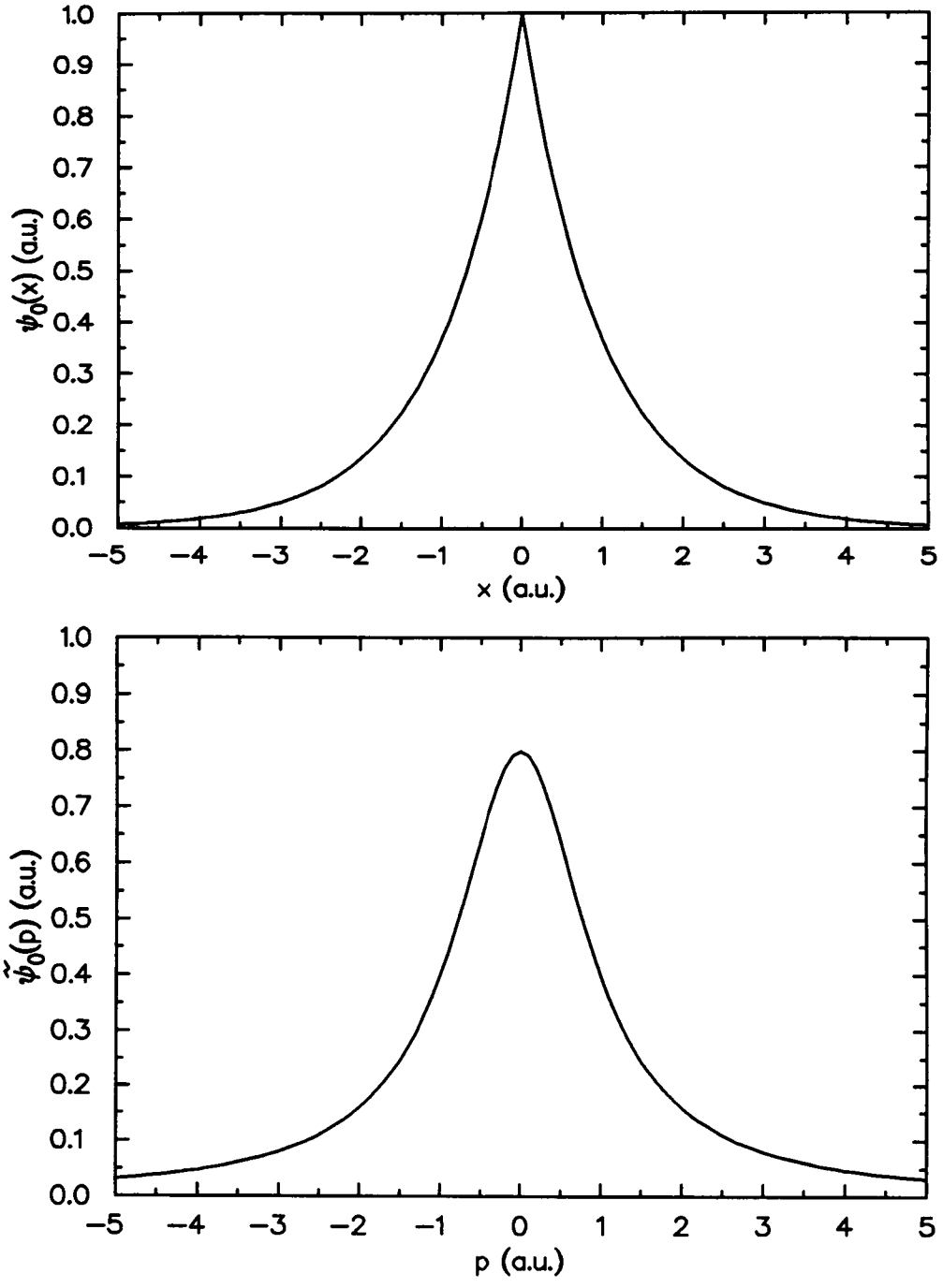

Figure 2.2: Wave function of the δ-atom in coordinate space (upper figure) and in momentum space (lower figure).

$|\tilde{\psi}_0(p)|^2$ gives the probability density of the electron with momentum p. The momentum distribution of a given state is usually referred to as the Compton profile which can be probed directly by Compton scattering or, in our case, by examining ionization spectra (see Chapter 4). The particular form of $\tilde{\psi}_0(p)$ for the δ-atom gives rise to a Lorentzian shape shown in Fig. 2.2. The momentum distribution peaks at 0, which implies that it is most probable to find electrons with zero momentum. As we shall see in Chapter 4, this observation leads directly to the interpretation of the binary encounter electron peak.

The power of using Green's functions in solving zero-range potential problems is clearly shown in the above simple procedure. Since the δ-potential localizes at one point, it effectively eliminates the integral present in integral equations. What is usually left is a set of linear algebraic equations that yields either the eigenenergies for bound states or the reflection and transmission coefficients for continuum states, as will be seen in the following sections.

2.2.3 The Continuum States of the δ-Atom

It has been demonstrated in the last section that there exists only one bound state for the δ-atom. There must be, on the other hand, an infinite number of continuum states. They can be conveniently derived by Green's function method.

From Eq. (2.6), the continuum wave function $\psi_k(x)$ consists of the incident wave and the scattered wave,

$$\begin{aligned}\psi_k(x) &= \phi(x) - \int dx' \frac{i}{k} \exp(ik|x-x'|)(-Z\delta(x'))\psi_k(x') \\ &= \frac{1}{\sqrt{2\pi}} \exp(ikx) + \frac{iZ}{k} \exp(ik|x|)\psi_k(0). \end{aligned} \tag{2.27}$$

Again $\psi_k(0)$ can be solved by setting $x = 0$ in (2.27),

$$\psi_k(0) = \frac{1}{\sqrt{2\pi}} \frac{ik}{Z+ik}. \tag{2.28}$$

Note that instead of yielding the eigenvalue equation as is the case for the bound state (Eq. (2.20)), this procedure leads in the present case to the

determination of the reflection coefficient $(iZ\psi_k(0)/k)$. $\psi_k(0)$ does not play the role of a normalization constant any more (compare (2.19) with (2.27)). Of course, the overall normalization of $\psi_k(x)$ is determined by the choice of $\phi(x)$.

The explicit continuum wave function for the δ-atom is

$$\psi_k(x) = \frac{1}{\sqrt{2\pi}} \left[\exp(ikx) - \frac{Z}{Z+ik} \exp(ik|x|) \right]. \tag{2.29}$$

The second term in (2.29) represents the scattered wave. It is an outgoing wave with respect to the origin. Physically it describes the partial reflection in the backward direction $\sim \exp(-ikx)$ and the partial transmission in the forward direction $\sim \exp(ikx)$ of the incident particle.

It is instructive to define a "normalization factor" $N_\delta(k)$ near the origin for the continuum states in analogy to the Coulomb factor $N_c(k)$ (the Gamov factor for an attractive potential),

$$N_\delta(k) = 2\pi \left|\psi_k(x \to 0)\right|^2 = \frac{k^2}{Z^2+k^2} \tag{2.30}$$

and

$$N_c(k) = (2\pi)^3 \left|\psi_c(\vec{r} \to 0)\right|^2 = \exp(\frac{\pi Z}{k}) \left|\Gamma(1+i\frac{Z}{k})\right|^2 \tag{2.31}$$

where $\psi_c(\vec{r})$ denotes the Coulomb continuum wave function [3]. In Chapter 1 the ECC and the ELC cusps in ion-atom collisions have been discussed qualitatively as a result of the attraction between the Coulomb center and the electron. Here we can go one step further in the explanation by noting the limiting values of $N_c(k)$ as $k \to 0$ from (2.31), namely,

$$N_c(k \to 0) \sim \frac{2\pi Z}{k}. \tag{2.32}$$

The $1/k$ singularity gives an enhancement for small k known as the cusp. In contrast, it is clear from Eq. (2.30) that $N_\delta(k)$ approaches zero as $k \to 0$, or more precisely,

$$N_\delta(k \to 0) \sim k^2/Z^2. \tag{2.33}$$

This indicates that there should be a depletion of electrons near the cusp region in the ionization spectra of δ-atoms. As will be shown later, this conclusion is indeed confirmed by the calculations of the spectra. In spite of the attractive nature of the δ-potential, the missing cusps are partially due to the lack of density of states across the continuum.

2.3 The δ-Molecule

If two δ-potentials are placed together, a "molecule" is formed, referred to in the following as the δ-molecule. Its Hamiltonian is given by Eq. (2.1), but with R fixed (not dependent on t) which corresponds to a Born-Oppenheimer approximation. The molecular states play an important role in slow collisions. The bound and continuum states of the molecule are discussed in this section.

2.3.1 The Bound States of the δ-Molecule

The same procedure for obtaining the bound state of the δ-atom can be utilized here for the δ-molecule. Following the argument in obtaining Eq. (2.19), we have for the wave function $\Psi_0(x)$,

$$\begin{aligned}\Psi_0(x) &= -\int dx' \frac{i}{k} \exp(ik|x-x'|)\left[-Z_T\delta(x') - Z_P\delta(x'-R)\right]\Psi_0(x') \\ &= \frac{i}{k}\left[Z_T \exp(ik|x|)\Psi_0(0) + Z_P \exp(ik|x-R|)\Psi_0(R)\right]. \qquad (2.34)\end{aligned}$$

We point out that (2.34) is formally identical to (2.19) except the additional term due to the other center at $x = R$. Setting $x = 0$ and $x = R$ respectively in (2.34) and regrouping the terms involving $\Psi_0(0)$ and $\Psi_0(R)$ yields

$$\begin{aligned}[\kappa - Z_T]\Psi_0(0) &- Z_P \exp(-\kappa R)\Psi_0(R) &= 0 \\ -Z_T \exp(-\kappa R)\Psi_0(0) &+ [\kappa - Z_P]\Psi_0(R) &= 0\end{aligned} \qquad (2.35)$$

where substitution has been made of $k = i\kappa$ which in turn is related to the eigenenergy by $E = k^2/2 = -\kappa^2/2$.

The necessary condition for a non-null set of solutions to Eq. (2.35) is that the following determinant be zero,

$$\begin{vmatrix} \kappa - Z_T & -Z_P \exp(-\kappa R) \\ -Z_T \exp(-\kappa R) & \kappa - Z_P \end{vmatrix} = 0 \qquad (2.36)$$

The determinant (2.36) can be reduced to an algebraic equation of the form

$$(\kappa - Z_T)(\kappa - Z_P) - Z_T Z_P \exp(-2\kappa R) = 0, \qquad (2.37)$$

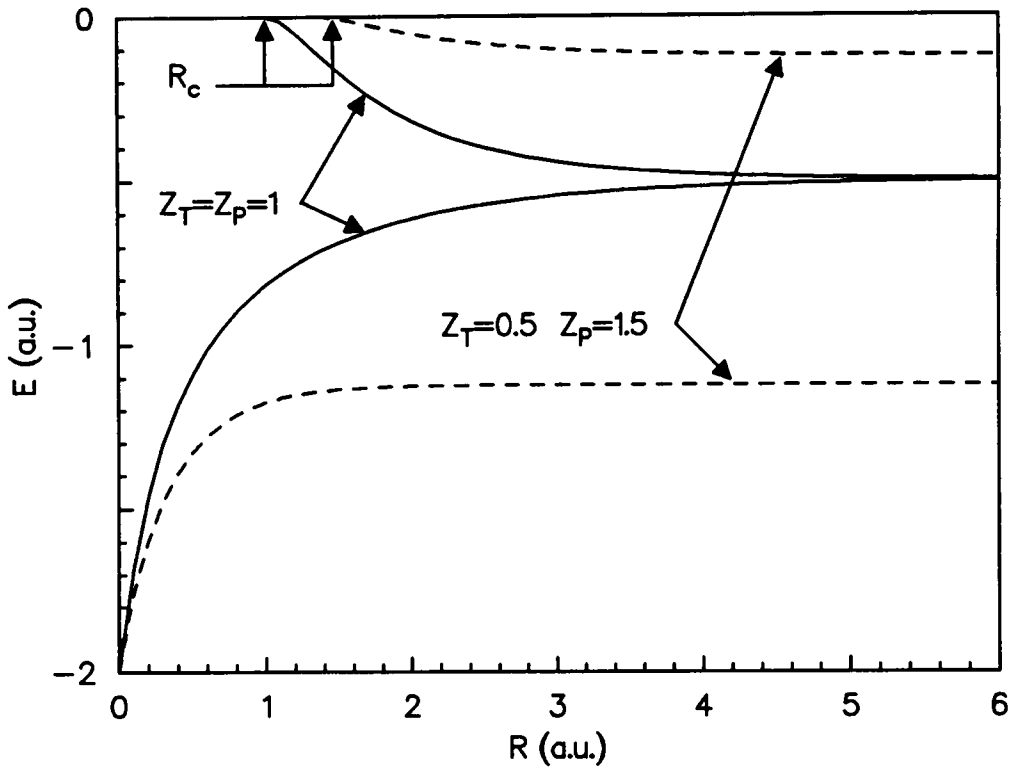

Figure 2.3: The energy level diagram of the δ-molecule as a function of the internuclear distance R for $Z_T = Z_P = 1$ (——) and for $Z_T = 0.5, Z_P = 1.5$ (- - -).

which can be solved numerically for a fixed R by standard root-finding techniques [60].

The energy level diagram of the molecular states is displayed in Fig. 2.3 as a function of the internuclear distance R. Two important features are evident. First, the number of bound states changes from one, when R is less than some critical distance R_c, to two when $R > R_c$. The ground state will be referred to as the binding orbital, and the excited state the anti-binding orbital. The anti-binding orbital is gradually "promoted" into the continuum as R approaches R_c. The existence of such a critical distance for arbitrary Z_T, Z_P can be shown as follows. Close to the continuum, the energy of the anti-binding state becomes small $\kappa \ll 1$. The exponential term in (2.37) can be expanded in powers of κ. Retaining terms up to second order in κ

produces

$$(\kappa - Z_T)(\kappa - Z_P) - Z_T Z_P(1 - 2\kappa R + 2\kappa^2 R^2) \sim 0. \tag{2.38}$$

Solving (2.38) for κ gives

$$\kappa = \frac{2Z_T Z_P R - Z_T - Z_P}{2Z_T Z_P R^2 - 1}. \tag{2.39}$$

Eq. (2.39) is valid only for small κ. When the following condition

$$R = R_c = \frac{Z_T + Z_P}{2Z_T Z_P} \tag{2.40}$$

is satisfied, we find from (2.39) $\kappa = 0$. This proves that for every pair of Z_T and Z_P, there exists a R_c for which the antibinding orbital enters the continuum.

Second, as R increases, the two energies approach their asymptotic limits defined by the isolated atomic eigenenergies $-Z_T^2/2, -Z_P^2/2$, respectively (see Fig. 2.3). This is to be expected because in the limit of $R \to \infty$, they are simply two separated atoms. For homonuclear diatomic δ-molecule $Z_T = Z_P$, the gerade state (even parity) and the ungerade state (odd parity) are degenerate at large R. The degeneracy implies that given a bound state in an isolated center, the bound state will have an equal mixing of the two molecular orbitals no matter how far away the other (identical) center is. The equal population of the two orbitals, even when the target (Z_T) and the projectile (Z_P) are far apart, is important for our discussion of the ionization mechanisms of $v/2$ electrons. Also note that the anti-binding orbital approaches the asymptotic limit from above ($\kappa < \min(Z_T, Z_P)$) while the binding orbital from below ($\kappa > \max(Z_T, Z_P)$).

After having obtained the eigenenergies of the δ-molecule we determine the eigenfunctions. Eq. (2.35) defines the relationship between $\Psi_0(0)$ and $\Psi_0(R)$. Substitution of (2.35) into (2.34) determines the eigenfunction within an multiplication constant that can be fixed by normalization. The final normalized eigenfunction for the bound states is

$$\Psi_0(x) = C\left[Z_T \exp(-\kappa|x|) + (\kappa - Z_T)\exp(2\kappa R)\exp(-\kappa|x - R|)\right] \tag{2.41}$$

with

$$C = \left\{\kappa\left[Z_T^2 + (\kappa - Z_T)^2 \exp(4\kappa R) + 2Z_T(\kappa - Z_T)(1 + 2\kappa R)\right]\right\}^{-1/2} \tag{2.42}$$

and κ to be determined from (2.37).

$\Psi_0(x)$ given by (2.41) consists of a sum of two exponential terms, one at each center. Although each term resembles an atomic orbital ((2.22)), the molecular eigenfunction ((2.41)) is in general not a linear combination of atomic orbitals (commonly known as LCAO) because κ is equal to neither Z_T nor Z_P for finite R, which means κ is not an atomic eigenenergy. However for $R \gg 1$, κ lies very close to the atomic eigenenergy (Fig. 2.3). To a good degree of approximation, the molecular states can be expanded in terms of LCAO. This type of expansions are useful for large impact parameter collisions in coupled-channel calculations [61].

2.3.2 The Continuum States of the δ-Molecule

We conclude the discussion of the static δ-molecule by briefly presenting the continuum states wave functions. The molecular Hamiltonian (2.1) can be regrouped as follows,

$$\begin{aligned} H &= H_0 + V_1(x) && (2.43) \\ &= H_{\delta-atom} + V_2(x) && (2.44) \end{aligned}$$

where $H_0 = -\partial^2/\partial x^2$, $V_1(x) = -Z_T\delta(x) - Z_P\delta(x-R)$, $H_{\delta-atom} = -\partial^2/\partial x^2 - Z_T\delta(x)$, and $V_2(x) = -Z_P\delta(x-R)$. There is now a choice as to what combination of Green's function and potential to use. The combination of the δ-atom Green's function $G_a^+(x,x')$ ((2.17)) with the potential $V_2(x)$ is preferred over that of the free particle Green's function $G_0^+(x,x')$ ((2.11)) with $V_1(x)$. The reason for choosing the former combination is two-fold. First we already know the continuum waves of the δ-atom ((2.29)). Second, it reduces the dimensionality of the linear equations from 2 to 1.

According to Eq. (2.6), the continuum wave function of the δ-molecule with the choice of $H_{\delta-atom}$ and $V_2(x)$ can be written as

$$\begin{aligned} \Psi_k(x) &= \psi_k(x) - \int dx' G_a^+(x,x')(-Z_P\delta(x'-R))\Psi_k(x') \\ &= \psi_k(x) + Z_P G_a^+(x,R)\Psi_k(R) && (2.45) \end{aligned}$$

where $\psi_k(x)$ is given by (2.29) with Z replaced by Z_T, and $G_a^+(x,x')$ is given by (2.17). By setting $x = R$ in (2.45) one can solve for $\Psi_k(R)$ and the result

is

$$\Psi_k(R) = k\frac{(1-\frac{Z_T}{Z_T+ik})\exp(ikR)}{k-iZ_P[1-\frac{Z_T}{Z_T+ik}\exp(2ikR)]}, \tag{2.46}$$

$$\begin{aligned}\Psi_k(x) &= \frac{1}{\sqrt{2\pi}}[\exp(ikx) \\ &- \frac{Z_T}{Z_T+ik}\left(1+\frac{iZ_P}{k}\exp(ikR)\Psi_k(R)\right)\exp(ik|x|) \\ &+ \frac{iZ_P}{k}\Psi_k(R)\exp(ik|x-R|)\Big]\end{aligned} \tag{2.47}$$

The important point of (2.47) is that it represents the incident free particle $\exp(ikx)$ being scattered into two outgoing waves $\exp(ik|x|)$ and $\exp(ik|x-R|)$. There is another linearly independent solution with incoming scattered waves $\exp(-ik|x|)$ and $\exp(-ik|x-R|)$. In the formulation of formal scattering theory both outgoing and incoming solutions can be treated on equal footing [3]. The latter point will be illustrated later when we calculate the ionization spectrum.

Chapter 3

Dynamical Evolution

3.1 General Remarks

In the previous chapter the static properties of the δ-model have been discussed when the internuclear distance R is fixed at a constant. We now delve into the dynamical solution when $R = vt$ is changing as a function of time. All information of the three-body dynamics rests upon the determination of time evolution of Eq. (2.1).

It turns out to be convenient to choose a reference frame such that the projectile and the target are moving with equal speeds. In this frame, which we shall refer to as the "center of velocity" (c.v.) frame, the target travels toward the negative $-\hat{x}$ direction at $v/2$, and the projectile toward the positive $+\hat{x}$ direction at $v/2$. Eq. (2.1) can be expressed in a more symmetric fashion in the c.v frame as the following,

$$H = -\frac{1}{2}\frac{\partial^2}{\partial x^2} - Z_T\delta(x + vt/2) - Z_P\delta(x - vt/2). \tag{3.1}$$

Our strategy is to seek the solutions to the Schrödinger equation

$$H\psi(x,t) = i\frac{\partial}{\partial t}\psi(x,t), \tag{3.2}$$

and to calculate various quantities of interest in the c.v. frame. Afterwards we transform the results back to the laboratory frame where the target is at rest. Since Eq. (3.2) is Galilei invariant, scalar quantities such as the elastic scattering and capture probabilities will be the same in both frames. But the

differential ionization probability as a function of the electron momentum will be translated by $+v/2$ under this transformation. Thus, the $v/2$ electrons in the laboratory frame will appear near 0 in the c.v. frame.

Before solving Eq. (3.2), let us examine the dilatation symmetry of the Hamiltonian operator (3.1). Substitution of (3.1) into (3.2) yields

$$\left[-\frac{1}{2}\frac{\partial^2}{\partial x^2} - Z_T\delta(x+vt/2) - Z_P\delta(x-vt/2)\right]\psi(x,t) = i\frac{\partial}{\partial t}\psi(x,t). \quad (3.3)$$

There are three independent parameters entering Eq. (3.3), i.e. Z_T, Z_P, and v. Dilatation symmetry helps us to reduce the set of independent parameters. To investigate the existence of such symmetries, we make the following dilatation transformations $x = \alpha x'$ and $t = \beta t'$ into Eq. (3.3) and arrive at

$$\left[-\frac{1}{2\alpha^2}\frac{\partial^2}{\partial x'^2} - Z_T\delta(\alpha x' + v\beta t'/2) - Z_P\delta(\alpha x' - v\beta t'/2)\right]\psi' = \frac{i}{\beta}\frac{\partial}{\partial t'}\psi' \quad (3.4)$$

where it is understood that $\psi' \equiv \psi(x',t')$. Multiplying both sides of (3.4) by β and setting $\beta = \alpha^2$ reduces (3.4) to

$$\left[-\frac{1}{2}\frac{\partial^2}{\partial x'^2} - \beta Z_T\delta(\sqrt{\beta}x' + v\beta t'/2) - \beta Z_P\delta(\sqrt{\beta}x' - v\beta t'/2)\right]\psi' = i\frac{\partial}{\partial t'}\psi'. \quad (3.5)$$

Using the relation $\delta(ax) = \delta(x)/a$, Eq. (3.5) can be simplified further by pulling v out of and absorbing β into the argument of the δ-functions,

$$\left[-\frac{1}{2}\frac{\partial^2}{\partial x'^2} - Z'_T\delta(x'/v\sqrt{\beta} + t'/2) - Z'_P\delta(x'/v\sqrt{\beta} - t'/2)\right]\psi' = i\frac{\partial}{\partial t'}\psi' \quad (3.6)$$

where the substitutions

$$Z'_T = Z_T/v, Z'_P = Z_P/v \quad (3.7)$$

have been made. If β is chosen to be $1/\sqrt{Z_T Z_P}$, then (3.6) is reduced to the following scaled equation

$$\left[-\frac{1}{2}\frac{\partial^2}{\partial x'^2} - Z'_T\delta(\sqrt{Z'_T Z'_P}x' + t'/2) - Z'_P\delta(\sqrt{Z'_T Z'_P}x' - t'/2)\right]\psi' = i\frac{\partial}{\partial t'}\psi' \quad (3.8)$$

Obviously, Eq. (3.8) depends only on two independent parameters Z'_T and Z'_P ((3.7)). Further reduction is not possible. This dilatation symmetry significantly reduces the dimensions of parameter space from three to two.

3.2 The Asymptotically Bound Solutions

3.2.1 The Entrance Channel

The solutions of (3.3) will be derived for the entrance channel where the electron is initially bound to the target. We follow closely the method originally developed by Zhdanov *et al.* [53] who solved the problem for symmetric collisions $Z_T = Z_P$. Our treatment provides a generalization to arbitrary Z_P and Z_T.

Let us start with the time-dependent bound state of the δ-atom. It is given by the static bound state (2.22) times a phase factor determined by a Galilei transform [62] of the state since the target is moving at a speed $-v/2\hat{x}$ in the c.v. frame. Taking into account the translation factor [62] resulting from the transform above, the complete initial state is given by

$$\phi_T(x,t) = \sqrt{Z_T}\exp(-ivx/2 - iv^2t/8 + iZ_T^2/2 - Z_T|x + vt/2|). \qquad (3.9)$$

The translation factor can be easily identified from (3.9) as $\exp(-ivx/2 - iv^2t/8)$. The $\exp(-ivx/2)$ signifies a shift of momentum by $-v/2$, while $\exp(-iv^2t/8)$ acts like a phase factor due to the "kinetic energy" $((v/2)^2/2)$ resulting from the shift of momentum.

We have seen in the last chapter that the static solutions of the δ-molecule consist of a sum of two exponential terms, one localized at each center (see Eq. (2.41)). This suggests that it may be possible to express the dynamical solutions as a series centered around the target and the projectile which are moving toward each other. It leads to a trial solution of the form

$$\begin{aligned}\psi(x,t) &= \exp(ivx/2 - iv^2t/8)\sum_n a_n u_n(x_P,t) \\ &+ \exp(-ivx/2 - iv^2t/8)\sum_n b_n w_n(x_T,t) \qquad (3.10)\end{aligned}$$

where $x_P = |x - vt/2|$ and $x_T = |x + vt/2|$ denote the relative coordinates with respect to the projectile and the target, respectively. a_n and b_n are time independent coefficients which, together with $u_n(x_P,t)$ and $w_n(x_T,t)$, are to be determined. The translation factors in front of the sums in (3.10) reflect the nuclear motion, so (3.10) can be viewed as an expansion around the projectile and the target. The partial derivatives of ψ with respect to t

and x can be calculated from (3.10) and substituted into (3.3) to yield (see details in Appendix A)

$$i\frac{\partial u_n}{\partial t} + \frac{1}{2}\frac{\partial^2 u_n}{\partial {x_P}^2} = 0. \tag{3.11}$$

$$i\frac{\partial w_n}{\partial t} + \frac{1}{2}\frac{\partial^2 w_n}{\partial {x_T}^2} = 0. \tag{3.12}$$

$$\sum_n \left[\exp(ivx/2)a_n\left(\frac{\partial u_n}{\partial x_P} + Z_P u_n\right) + \exp(-ivx/2)b_n Z_P w_n\right]_{x=vt/2} = 0. \tag{3.13}$$

$$\sum_n \left[\exp(-ivx/2)b_n\left(\frac{\partial w_n}{\partial x_T} + Z_T w_n\right) + \exp(ivx/2)a_n Z_T u_n\right]_{x=-vt/2} = 0. \tag{3.14}$$

Note that Eqs. (3.11) and (3.12) behave like a free particle while Eqs. (3.13) and (3.14) give the constraints (or boundary conditions) at the δ-potentials ($x = \pm vt/2$). It is a direct result of the fact that the Hamiltonian (3.3) describes the motion of a free particle everywhere except at $x = \pm vt/2$. Eqs. (3.11) and (3.12) can be solved to obtain u_n and w_n which are of the form

$$u_n = \exp(-p_n x_P + ip_n^2 t/2) \tag{3.15}$$

$$w_n = \exp(-q_n x_P + iq_n^2 t/2) \tag{3.16}$$

where p_n and q_n remain to be determined. With (3.15) and (3.16), $\partial u_n/\partial x_P$ and $\partial w_n/\partial x_T$ are readily available. They can be inserted into (3.13) and (3.14) to give

$$\begin{aligned} 0 &= a_0(Z_P - p_0)\exp(ip_0^2 t/2) \\ &+ \sum_{n=0}^{\infty}\Big[a_{n+1}(Z_P - p_{n+1})\exp(ip_{n+1}^2 t/2) \\ &\quad + b_n Z_P \exp(iq_n^2 t/2 - q_n|vt| - iv^2 t/2)\Big]. \end{aligned} \tag{3.17}$$

$$\begin{aligned} 0 &= b_0(Z_T - q_0)\exp(iq_0^2 t/2) \\ &+ \sum_{n=0}^{\infty}\Big[b_{n+1}(Z_T - q_{n+1})\exp(iq_{n+1}^2 t/2) \\ &\quad + a_n Z_T \exp(ip_n^2 t/2 - p_n|vt| - iv^2 t/2)\Big]. \end{aligned} \tag{3.18}$$

Because of the $|vt|$ term in (3.17) and (3.18), our method here can yield solutions only for one half of the time domain, $-\infty < t \leq 0$ or $0 \leq t < +\infty$. For the entrance channel where the system starts at $t = -\infty$, the former is appropriate. For the exit channel to be discussed in the next section, the latter will be used. Eqs. (3.17) and (3.18) read for $t < 0$

$$0 = a_0(Z_P - p_0)\exp(ip_0^2 t/2) + \sum_{n=0}^{\infty}\left[a_{n+1}(Z_P - p_{n+1})\exp(ip_{n+1}^2 t/2) + b_n Z_P \exp(i(q_n - iv)^2 t/2)\right]. \quad (3.19)$$

$$0 = b_0(Z_T - q_0)\exp(iq_0^2 t/2) + \sum_{n=0}^{\infty}\left[b_{n+1}(Z_T - q_{n+1})\exp(iq_{n+1}^2 t/2) + a_n Z_T \exp(i(p_n - iv)^2 t/2)\right]. \quad (3.20)$$

Obviously Eq. (3.19) is satisfied if the first term and each term in the sum are identically zero for all t, which leads to the recurrence relation

$$\begin{aligned} p_0 &= Z_P \\ p_{n+1} &= q_n - iv, \quad a_{n+1} = \frac{Z_P}{p_{n+1} - Z_P} b_n. \end{aligned} \quad (3.21)$$

Similar relations follow from (3.20)

$$\begin{aligned} q_0 &= Z_T \\ q_{n+1} &= p_n - iv, \quad b_{n+1} = \frac{Z_T}{q_{n+1} - Z_T} a_n. \end{aligned} \quad (3.22)$$

The complex "momenta" p_n and q_n, and hence the exact forms of u_n and w_n ((3.15) and (3.16)), are uniquely determined by the recurrence relations (3.21) and (3.22). However, to calculate the wave function ψ ((3.10)), one needs to know the coefficients a_0 and b_0 as well. One can already guess that they must be related to the initial conditions. To illustrate this, we examine the asymptotic behavior of u_n and w_n as $t \to -\infty$. Note that p_n and q_n as determined from (3.21) and (3.22) have the forms of

$$\begin{aligned} &p_n = Z_P - inv \ \ (n \text{ even}), \quad p_n = Z_T - inv \ \ (n \text{ odd}) \\ &q_n = Z_T - inv \ \ (n \text{ even}), \quad q_n = Z_P - inv \ \ (n \text{ odd}). \end{aligned} \quad (3.23)$$

When (3.23) is substituted into (3.15) and (3.16), u_n and w_n can be expressed as

$$\begin{aligned} u_n &= \exp(-p_n x_P + i(Z_{P,T}^2 + n^2v^2)t/2 + Z_{P,T}nvt) \\ w_n &= \exp(-q_n x_T + i(Z_{T,P}^2 + n^2v^2)t/2 + Z_{T,P}nvt) \end{aligned} \tag{3.24}$$

where the first subscript $s1$ in $Z_{s1,s2}$ should be taken for even n and the second subscript $s2$ for odd n. It is clear from (3.24) that in the asymptotic region $t \to -\infty$, all but u_0 and w_0 vanish because of the exponentially decaying term $\exp(Z_{P,T}nvt)$. In particular u_0 and w_0 are, up to a constant, simply the asymptotic bound states to the projectile and the target, respectively,

$$\begin{aligned} u_0 &= \exp(-Z_P x_P + iZ_P t/2) \\ w_0 &= \exp(-Z_T x_T + iZ_T t/2) \end{aligned} \tag{3.25}$$

Therefore the wave function expansion (3.10) approaches asymptotically

$$\psi(x, t \to -\infty) = exp(ivx/2 - iv^2t/8)a_0u_0 + exp(-ivx/2 - iv^2t/8)b_0w_0. \tag{3.26}$$

Since we are interested in the solution evolving from the initial bound state of the target, we require $a_0 = 0$. Furthermore, by comparing (3.26) and (3.9) it can be seen that $b_0 = \sqrt{Z_T}$. Once a_0 and b_0 are fixed, the remaining coefficients a_n and b_n for $n \geq 1$ can be generated from (3.21) and (3.22). If we denote the solution corresponding to the asymptotically bound state of the target by ψ_T^+, we have (from (3.10), (3.15) and (3.16))

$$\begin{aligned} \psi_T^+(x,t) = \exp(ivx/2 - iv^2t/8) \sum_n a_n \exp(-p_n|x - vt/2| + ip_n^2 t/2) \\ + \quad \exp(-ivx/2 - iv^2t/8) \sum_n b_n \exp(-q_n|x + vt/2| + iq_n^2 t/2) \end{aligned} \tag{3.27}$$

where p_n, q_n, a_n, and b_n are given by the recurrence relations

$$\begin{aligned} &p_0 = Z_P, \quad q_0 = Z_T \\ &p_{n+1} = q_n - iv, \quad q_{n+1} = p_n - iv \\ &a_0 = 0, \quad b_0 = \sqrt{Z_T} \\ &a_{n+1} = \frac{Z_P}{p_{n+1} - Z_P} b_n, \quad b_{n+1} = \frac{Z_T}{q_{n+1} - Z_T} a_n. \end{aligned} \tag{3.28}$$

We point to some interesting properties of the solution ((3.27)) just found: First of all, ψ_T^+ remains bounded for $-\infty \leq x \leq +\infty$ at any instance $t < 0$. This is so because p_n and q_n ((3.28)) always have a positive real part Z_T or Z_P, depending on n, so that $\exp(-p_n|x-vt/2|)$ and $\exp(-q_n|x-vt/2|)$ always remain bounded. This should be the case because of probability conservation. In other words, once the solution is normalized such as the initial bound state, it must remain so for all times. The second and more interesting observation is that there exist an infinite number of quasi-stationary states ("resonances") with life times of $\tau = 1/Z_T nv$, $n \geq 1$ (see Eq. (3.24)). By examining (3.28) it is clear that

$$a_n \neq 0 \text{ only for odd } n, b_n \neq 0 \text{ only for even } n. \tag{3.29}$$

Therefore ψ_T^+ ((3.27)) is composed of only odd n terms of u_n and even n terms of w_n. But according to (3.23) or (3.28), $p_n = Z_T - inv$ when n is odd and $q_n = Z_T - inv$ when n is even. As a result the exponentially decaying terms ((3.24)) are limited to the form of $\exp(Z_T nvt)$. Due to the rapid decay, the quasi-stationary states are significant only for small t's, i.e. when the projectile is close to the target. The lifetime τ might be qualitatively explained as the time a wave packet of speed $2nv$ needs to travel across the target of the size $\sim 2/Z_T$ (see (2.22)). Multiple scattering would be responsible for generation of these wave packets (to be discussed in detail in the next section).

The wave function $\psi_T^+(x,t)$ at different instances is graphically presented in Fig. 3.1 for $Z_P = Z_T = 1$. $\psi_T^+(x,t)$ as given by (3.27) is valid only for $t \leq 0$. Solutions for $t > 0$ can be constructed similarly [53]. At $t = -4$ the projectile is far away and the electron is still bound to the target without substantial distortion. As the projectile comes close ($t = -1$), some electrons are captured by the projectile. When the positions of the projectile and of the target coincide ($t = 0$), the electronic cloud is greatly disturbed. At $t = 1$ the dispersion of the electron density continues and the binary electrons (with speed of $\sim 2v$ between $x = 3, 4$) become visible. At $t = 4$ the projectile leaves the interaction zone with more electrons in the projectile bound state than in the target bound state, i.e. a higher probability of capture than elastic scattering. The charge density near $x \sim 8$ is mainly composed of binary electrons well seperated from the projectile. There is little change for later times $t > 4$.

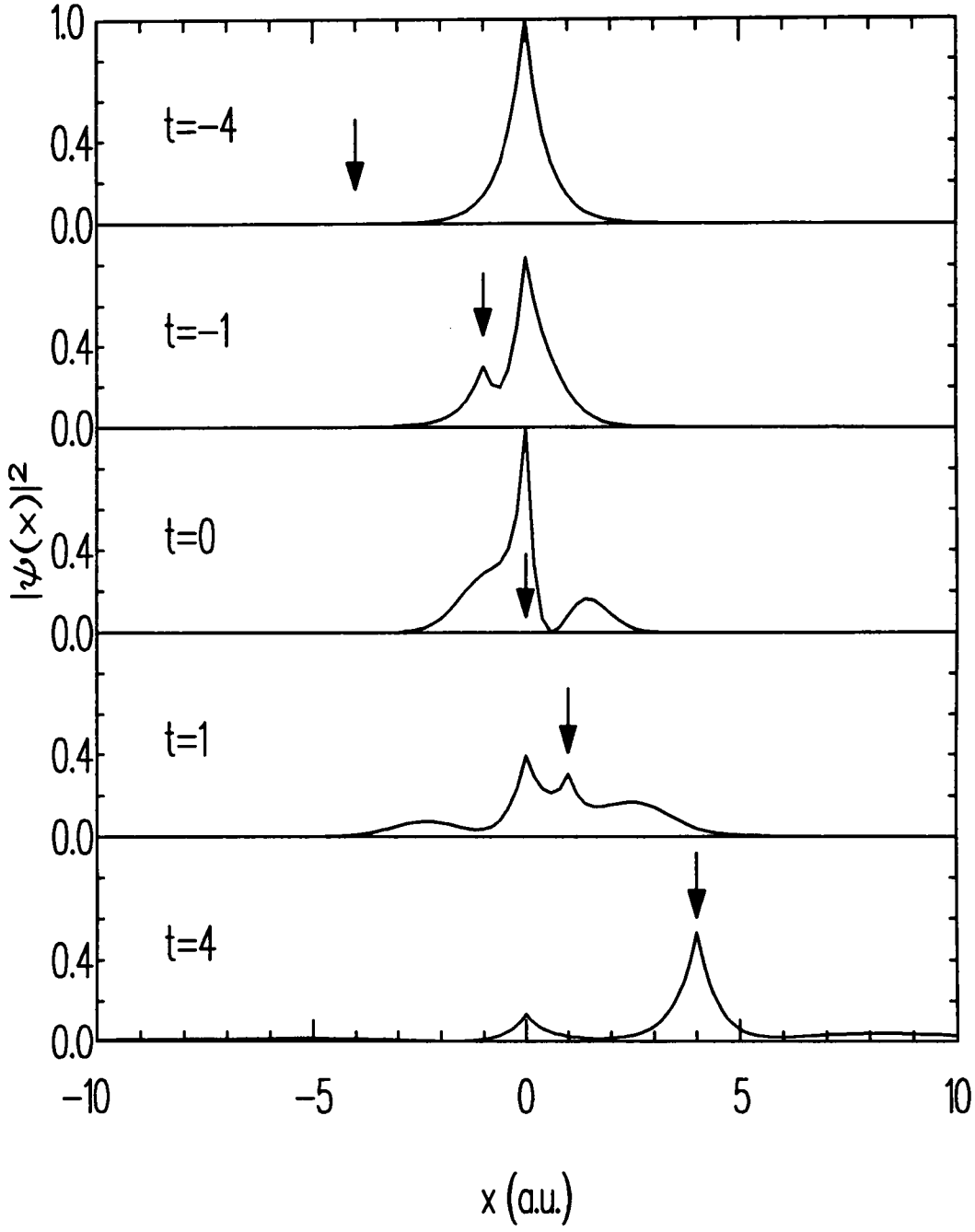

Figure 3.1: The exact time dependent wave function in coordinate space (labframe) as a function of time. The target is at origin ($x = 0$). The arrows indicate the position of the projectile at time t.

3.2.2 The Exit Channels

In this section we are interested in obtaining solutions corresponding to elastic scattering and capture in the exit channels. For elastic scattering, we seek the solution ψ_T^- which has the asymptotic behavior

$$\psi_T^-(x, t \to +\infty) = \sqrt{Z_T}\exp(-ivx/2 - iv^2t/8 + iZ_T^2/2 - Z_T|x + vt/2|), \quad (3.30)$$

which is a bound state of the target. Similarly, the asymptotic limit for capture must be a bound state of the projectile

$$\begin{aligned}\psi_P^-(x, t \to +\infty) &= \phi_P(x, t) \\ &= \sqrt{Z_P}\exp(ivx/2 - iv^2t/8 + iZ_P^2/2 - Z_P|x - vt/2|). \quad (3.31)\end{aligned}$$

Exactly the same procedure as that of the entrance channel can be repeated here to yield Eqs. (3.17) and (3.18). Keeping in mind that we are now in the positive time domain, we replace $|vt|$ by vt in (3.17) and (3.18) to obtain two conditions similar to (3.19) and (3.20)

$$\begin{aligned}0 = {} & a_0(Z_P - p_0)\exp(ip_0^2t/2) + \\ & \sum_{n=0}^{\infty}\left[a_{n+1}(Z_P - p_{n+1})\exp(ip_{n+1}^2t/2) + b_nZ_P\exp(i(q_n + iv)^2t/2)\right]. \quad (3.32)\end{aligned}$$

$$\begin{aligned}0 = {} & b_0(Z_T - q_0)\exp(iq_0^2t/2) + \\ & \sum_{n=0}^{\infty}\left[b_{n+1}(Z_T - q_{n+1})\exp(iq_{n+1}^2t/2) + a_nZ_T\exp(i(p_n + iv)^2t/2)\right]. \quad (3.33)\end{aligned}$$

In analogy to (3.21) and (3.22) the following relations must hold to satisfy (3.32) and (3.33)

$$\begin{aligned}p_0 &= Z_P \\ p_{n+1} &= q_n + iv, \quad a_{n+1} = \frac{Z_P}{p_{n+1} - Z_P}b_n. \quad (3.34)\end{aligned}$$

Similar relations follow from (3.20)

$$\begin{aligned}q_0 &= Z_T \\ q_{n+1} &= p_n + iv, \quad b_{n+1} = \frac{Z_T}{q_{n+1} - Z_T}a_n. \quad (3.35)\end{aligned}$$

Again, we are left with the choices of a_n and b_n, which will be determined by the initial (asymptotic) behavior. For elastic scattering ((3.30)) we set $a_0 = 0$ and $b_0 = \sqrt{Z_T}$. ψ_T^- is then given by

$$\psi_T^-(x,t) = \exp(ivx/2 - iv^2t/8)\sum_n a_n \exp(-p_n|x - vt/2| + ip_n^2t/2)$$
$$+ \quad \exp(-ivx/2 - iv^2t/8)\sum_n b_n \exp(-q_n|x + vt/2| + iq_n^2t/2) \quad (3.36)$$

where p_n, q_n, a_n, and b_n are given by the recurrence relations

$$\begin{aligned} &p_0 = Z_P, \quad q_0 = Z_T \\ &p_{n+1} = q_n + iv, \quad q_{n+1} = p_n + iv \\ &a_0 = 0, \quad b_0 = \sqrt{Z_T} \\ &a_{n+1} = \frac{Z_P}{p_{n+1} - Z_P} b_n, \quad b_{n+1} = \frac{Z_T}{q_{n+1} - Z_T} a_n. \end{aligned} \quad (3.37)$$

For capture ((3.31)) we set $a_0 = \sqrt{Z_P}$ and $b_0 = 0$. ψ_P^- is then given by

$$\psi_P^-(x,t) = \exp(ivx/2 - iv^2t/8)\sum_n a_n \exp(-p_n|x - vt/2| + ip_n^2t/2)$$
$$+ \quad \exp(-ivx/2 - iv^2t/8)\sum_n b_n \exp(-q_n|x + vt/2| + iq_n^2t/2) \quad (3.38)$$

where p_n, q_n, a_n, and b_n are given by the recurrence relations

$$\begin{aligned} &p_0 = Z_P, \quad q_0 = Z_T \\ &p_{n+1} = q_n + iv, \quad q_{n+1} = p_n + iv \\ &a_0 = \sqrt{Z_P}, \quad b_0 = 0 \\ &a_{n+1} = \frac{Z_P}{p_{n+1} - Z_P} b_n, \quad b_{n+1} = \frac{Z_T}{q_{n+1} - Z_T} a_n. \end{aligned} \quad (3.39)$$

Analogous properties to ψ_T^+ also exist for ψ_T^- and ψ_P^- and will not be repeated here. We shall apply the three solutions to calculations of elastic scattering, capture, and ionization probabilities.

3.3 The Asymptotic Continuum Solutions

We have presented so far the exact solutions to (3.3) for asymptotically bound states. As will be seen later we also need the solution corresponding

to the asymptotic continuum states to calculate the ionization spectra. We shall seek a solution analogous to (3.10), but with an incident wave. Such a solution can be written as

$$\begin{aligned}\psi_k^-(x,t) &= \frac{1}{\sqrt{2\pi}}\exp(ikx - ik^2t/2) + \exp(ivx/2 - iv^2t/8)\sum_n a_n u_n(x_P,t) \\ &+ \exp(-ivx/2 - iv^2t/8)\sum_n b_n w_n(x_T,t). \qquad (3.40)\end{aligned}$$

The first term is just the incident plane wave. The sum represents the scattered waves. Thus $\psi_k^-(x,t)$ is structurally analogous to the continuum states of the δ-molecule (2.45).

To determine the unknown coefficients in (3.40), one can proceed in the same way as above. Then the functional forms of u_n and w_n are given by (3.15) and (3.16), respectively. The equations governing q_n, w_n, a_n, and b_n turn out to be

$$\begin{aligned}0 = &\frac{Z_P}{\sqrt{2\pi}}\exp(-i(k - v/2)^2t/2) + a_0(Z_P - p_0)\exp(ip_0^2t/2) + \\ &\sum_{n=0}^{\infty}\left[a_{n+1}(Z_P - p_{n+1})\exp(ip_{n+1}^2t/2) + b_n Z_P \exp(i(q_n + iv)^2t/2)\right]. \qquad (3.41)\end{aligned}$$

$$\begin{aligned}0 = &\frac{Z_T}{\sqrt{2\pi}}\exp(-i(k + v/2)^2t/2) + b_0(Z_T - q_0)\exp(iq_0^2t/2) + \\ &\sum_{n=0}^{\infty}\left[b_{n+1}(Z_T - q_{n+1})\exp(iq_{n+1}^2t/2) + a_n Z_T \exp(i(p_n + iv)^2t/2)\right]. \qquad (3.42)\end{aligned}$$

Comparing Eqs. (3.41) and (3.42) with (3.32) and (3.33) reveals that there is an additional term which is due to the incident plane wave. Eqs. (3.41) and (3.42) yield the following recurrence relations

$$\begin{aligned}&p_0 = \pm i|k - v/2|, \quad q_0 = \pm i|k + v/2| \\ &p_{n+1} = \pm(q_n + iv), \quad q_{n+1} = \pm(p_n + iv) \\ &a_0 = \frac{1}{\sqrt{2\pi}}\frac{Z_P}{p_0 - Z_P}, \quad b_0 = \frac{1}{\sqrt{2\pi}}\frac{Z_T}{q_0 - Z_T} \qquad (3.43) \\ &a_{n+1} = \frac{Z_P}{p_{n+1} - Z_P}b_n, \quad b_{n+1} = \frac{Z_T}{q_{n+1} - Z_T}a_n.\end{aligned}$$

In contrast to the recurrence relations for the bound states ((3.34) and (3.35)), the values of a_0 and b_0 are no longer arbitrary. Instead the signs of the p_n and q_n are undetermined. The latter is related to the incoming and outgoing boundary conditions for continuum waves. Indeed, by looking at the functional forms of u_n and w_n ((3.15) and (3.16)), one can construct a solution with incoming boundary conditions such that the scattered waves always travel inward to the target (or to the projectile), i.e., a wave of the form $\exp(-ip|x \pm vt/2|)$. We thus need to choose the signs of p_n and q_n such that the imaginary parts remain positive,

$$\begin{aligned} p_0 &= i|k - v/2|, \quad q_0 = i|k + v/2| \\ p_{n+1} &= q_n + iv, \quad q_{n+1} = p_n + iv. \end{aligned} \tag{3.44}$$

Eq. (3.44) has a very interesting interpretation in terms of multiple scattering briefly mentioned in the last section. Let us look at the p_n series first. An electron of momentum k has a relative speed of $|k - v/2|$ in the projectile rest frame. After a head-on collision with the infinitely heavy projectile (at rest) the electron reverses its momentum with the same magnitude, which is equal to p_0 (apart from the factor i which is immaterial because of the definition for u_n and w_n). An electron of momentum p_0 in the projectile rest frame has a momentum of $p_0 + iv$ in the target rest frame since the relative speed between the frames is v. After being scattered by the target, the electron once again reverses its momentum, but keeps its magnitude, or $q_1 = p_0 + iv$. That is exactly what is predicted from the recurrence relations (3.44). The same interpretation can be assigned to the p_1 term. Therefore $n = 1$ terms represent a double scattering, a scattering at the projectile (p_0) followed by a scattering at the target (q_1), and vice versa. Higher order members of the series with $n > 1$ correspond to multiple scattering sequences. We shall find evidence for the scattering sequences and application of this concept in projectile ionization in the next chapter.

3.4 Probability Calculation

Having obtained various solutions corresponding to different asymptotic conditions, we are ready to calculate all quantities of interest.

The transition amplitude is the projection of the exact wave function

$\psi_i(t)$ onto the final state ϕ_f

$$a_{fi} = \lim_{t \to +\infty} \langle \phi_f(t) | \psi_i(t) \rangle. \tag{3.45}$$

a_{fi} can be expressed alternatively as

$$\begin{aligned} a_{fi} &= \lim_{t \to +\infty, t' \to -\infty} \langle \phi_f(t) | U(t,t') | \phi_i(t') \rangle \\ &= \lim_{t \to +\infty, t' \to -\infty} \langle \phi_f(t) | U(t,0) U(0,t') | \phi_i(t') \rangle \\ &= \langle \psi_f^-(0) | \psi_i^+(0) \rangle \end{aligned} \tag{3.46}$$

where $U(t,t')$ is the time evolution operator defined by the operator equation

$$H(t)U(t,t') = i\frac{\partial U(t,t')}{\partial t}, \tag{3.47}$$

$\psi_f^-(0) = U(0,+\infty)\phi_f(+\infty)$ is the exact state propagated backward in time from the final state, and $\psi_i^+(0) = U(0,-\infty)\phi_i(-\infty)$ is the exact state propagated forward in time from the initial state. We note from (3.46) that for calculation of transition amplitudes it is sufficient to know only the wave functions at $t = 0$.

We wish to calculate transition amplitudes for elastic scattering, capture and ionization. The initial state is the same and only the final states vary. Accordingly, $\psi_i^+(0)$ is given by $\psi_T^+(t=0)$ ((3.27)). For elastic scattering ψ_f^- should be replaced by ψ_T^- ((3.36)),

$$a_{elastic} = \langle \psi_T^-(0) | \psi_T^+(0) \rangle, \quad P_{elastic} = |a_{elastic}|^2 \tag{3.48}$$

where $P_{elastic}$ denotes the elastic scattering probability. For capture ψ_f^- should be replaced by ψ_P^- ((3.38)),

$$a_{capture} = \langle \psi_P^-(0) | \psi_T^+(0) \rangle, \quad P_{capture} = |a_{capture}|^2 \tag{3.49}$$

where $P_{capture}$ denotes the capture probability. From conservation of probability (2.2), the total ionization probability is simply

$$P_{ionization} = 1 - P_{elastic} - P_{capture}. \tag{3.50}$$

The differential ionization amplitude $a(k)$ can be calculated by projecting the wave function at $+\infty$ onto the continuum portion of the Hilbert space as

$$a(k) = \lim_{t \to +\infty, t' \to -\infty} \langle k(t) | \hat{P}(t) U(t,t') | \phi_i(t') \rangle \tag{3.51}$$

where $\phi_i(t)$ is the initial state and $|k(t)\rangle$ is the plane wave

$$\langle x|k(t)\rangle = \frac{1}{\sqrt{2\pi}} \exp(ikx - ik^2t/2), \tag{3.52}$$

and $\hat{P}$ is the continuum projection operator

$$\hat{P} = 1 - |\phi_T(t)\rangle\langle\phi_T(t)| - |\phi_P(t)\rangle\langle\phi_P(t)| \tag{3.53}$$

where $\phi_{T,P}(t)$ are bound states of the target and the projectile, given by (3.9) and (3.31) respectively. Proceeding in the same fashion as we did for (3.46), one finds

$$\begin{aligned} a(k) &= \langle\psi_k^-(0)|\psi_T^+(0)\rangle - a_{elastic}\langle\psi_k^-(0)|\psi_T^-(0)\rangle - a_{capture}\langle\psi_k^-(0)|\psi_P^-(0)\rangle \\ p(k) &= |a(k)|^2 \end{aligned} \tag{3.54}$$

where $p(k)$ denotes the differential ionization probability of momentum k, and $a_{elastic}$ and $a_{capture}$ are given by (3.48) and (3.49). The total ionization probability is then given by

$$P_{ionization} = \int_{-\infty}^{+\infty} p(k)dk. \tag{3.55}$$

It can serve as a numerical check by comparison with the result obtained from (3.50).

3.5 The δ-Model in 3D

For practical purposes the δ-model in three dimensions (3D) is exactly solvable only for zero impact parameter. The Schrödinger equation of 1D δ-model (3.3) can be generalized to 3D (for zero impact parameter) as

$$\left[-\frac{1}{2}\nabla^2 - Z_T\delta(\vec{r} + vt/2\hat{z}) - Z_P\delta(\vec{r} - vt/2\hat{z})\right]\psi(\vec{r},t) = i\frac{\partial}{\partial t}\psi(\vec{r},t) \tag{3.56}$$

where $\vec{r}$ is the coordinates of the electron. Details about calculations of the corresponding wave function and ionization probability can be found in Ref. [63].

Chapter 4

Ionization Spectra for the δ-Model

The exact solutions to the δ-model discussed in Chapter 3 enable us to calculate various quantities of interest without invoking any approximation. Numerical results for total elastic, capture and ionization probabilities are presented in this chapter. The differential ionization probability $p(k)$ is studied in detail. The $v/2$ electrons will be identified and its underlying emission mechanism is discussed. Peaks in $p(k)$ will be shown to originate from a multiple scattering sequence.

4.1 Total Probability

It is clear from Chapter 3 that it is easier to evaluate the total ionization probability $P_{ionization}$ than $p(k)$ because of the unitarity requirement (3.50). We therefore discuss first results for elastic, capture, and total ionization probabilities.

In view of the reduced parameter set (3.7), it is natural to look at the probabilities as a function of v for a given pair of Z_P and Z_T. We pick three representative cases which cover both symmetric and asymmetric collisions, $Z_P = Z_T$, $Z_T > Z_P$, and $Z_T < Z_P$. In Fig. 4.1 $P_{elastic}$, $P_{capture}$, and $P_{ionization}$ are plotted as a function of the collision speed v for three different nuclear charge ratios $\gamma = Z_P/Z_T$. The elastic scattering ($P_{elastic}$) and capture ($P_{capture}$) show a considerable amount of structure in all cases, particularly

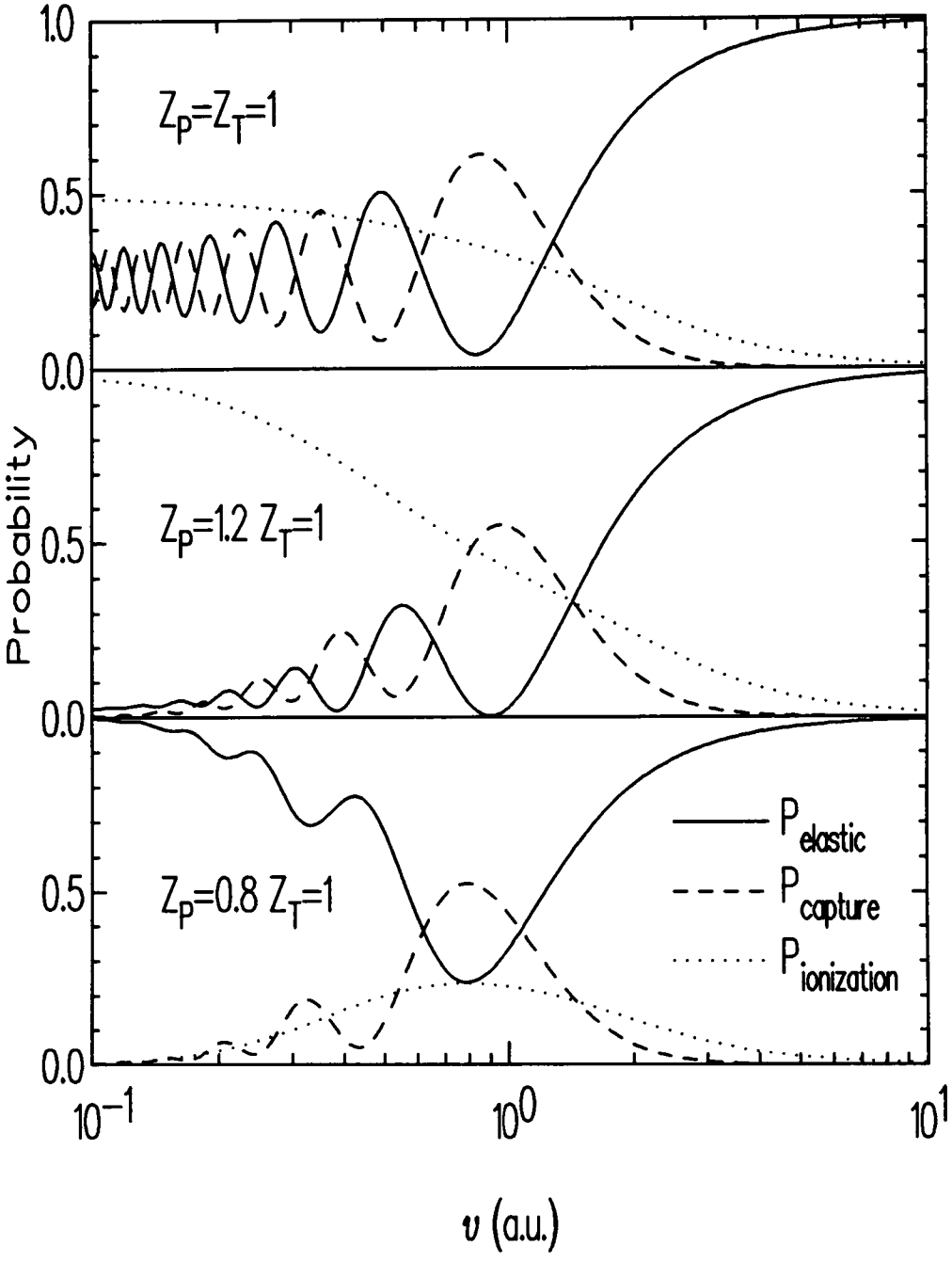

Figure 4.1: Absolute total probabilities $P_{elastic}$, $P_{capture}$, and $P_{ionization}$ as a function of the projectile speed v for three collision systems $Z_P = Z_T$, $Z_P > Z_T$, and $Z_P < Z_T$.

at intermediate to small v's. The total ionization probability ($P_{ionization}$, obtained from Eq. (3.50)) displays much less pronounced structures.

Closer examination of Fig. 4.1 shows that $P_{elastic}$ approaches unit probability at large v for all γ's. In the limit $v \gg 1$, the effective interaction time between the electron and the projectile becomes very short. The projectile just flies by very quickly without significantly disturbing the target system. As a result there is a high probability that the target state remains undisturbed, i.e., elastic scattering. This explains the almost unit probability for elastic scattering and the very small probabilities for capture and ionization. Of course, the effective (scaled) interaction time depends on the projectile charge Z_P. A larger Z_P translates into a longer interaction time at a given v. Physically one would expect the smaller the Z_P, the faster $P_{elastic}$ will approach the asymptotic unit probability. If one looks at Fig. 4.1 more carefully for large v, one indeed notices (judging from the gap between $P_{elastic}$ and the maximum value 1 around $v \sim 7$) that the approach to unity is fastest when $\gamma = 0.8$ (bottom figure), a little slower for $\gamma = 1$ (top figure), and the slowest for $\gamma = 1.2$ (middle figure).

As v decreases, $P_{elastic}$ starts to develop oscillatory structures which become denser as $v \to 0$. Obviously, the capture probability $P_{capture}$ follows the elastic scattering probability in a complementary manner (Fig. 4.1). When $P_{elastic}$ reaches a local maximum, $P_{capture}$ reaches a local minimum, and vice versa. This produces a relatively smooth behavior for the total ionization probability as a function of v. It is quite remarkable that these oscillations have been observed experimentally in ion-atom collision for elastic scattering [64] and for capture [65] (for a 3D Coulomb problem!). The oscillatory behavior has been explained theoretically as an interference effect between molecular states [66, 67]. Within a two-state approximation (p. 147 of Ref. [3]) the capture probability behaves like

$$P = \sin^2(C/v) \tag{4.1}$$

for a fixed impact parameter at small v, C being a constant which depends on the impact parameter. It predicts that $P_{capture}$ is a periodic function of $1/v$. It also implies that the valleys have a value of 0 and peaks have a value of 1.

Fig. 4.2 displays the capture probability as a function of $1/v$ for the resonant collision $Z_P = Z_T$. It can be seen that the nearly equal-spaced

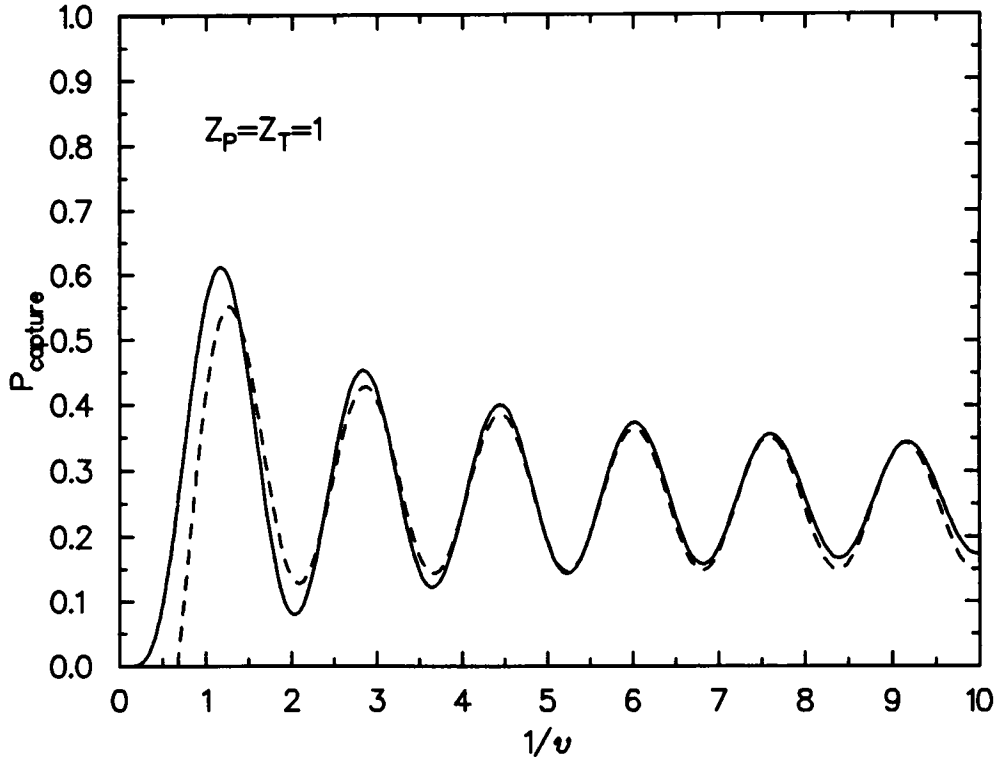

Figure 4.2: Capture probability as a function of $1/v$. —— $P_{capture}$, - - - Fitted according to Eq. (4.2) (see text).

peaks and valleys in $P_{capture}$ confirm this prediction as did the experiment [65]. However, the valleys are not zero and the peaks not unity as a simple sinusoidal wave would imply. In addition, the oscillations are damped toward smaller v (Fig. 4.2). The damping also shows up in the experimental data which has led to the following empirical formula [65]

$$P = A(v) + B(v)\sin^2(C/v + \alpha) \tag{4.2}$$

where $A(v)$ and $B(v)$ are slowly varying functions of $v \ll 1$, and α is a constant phase shift. The term $A(v)$ in Eq. (4.2) would give a finite value to the valleys and $B(v)$ plays the role of a damping factor. Curiously enough, a simple fit with $A(v) = 0.15 - 0.1v^2$, $B(v) = 0.15 + 0.4v$, $C = 2$, and $\alpha = 2.1$ reproduces the damped oscillatory behavior very well for small v. It is clear that similar fitting could be carried out for $P_{elastic}$. It is no

coincidence that Eq. (4.2) works so well. A better approximation taking approximately into account the coupling to the continuum states has been shown to be in excellent agreement with experiment (p. 202 of Ref. [3]). The treatment of the δ-model, which includes the coupling to the continuum exactly, provides therefore additional strong support to the validity of the empirical formula (4.2). It appears remarkable that the 1D δ-model can reproduce all the essential features of the quantum oscillations in near symmetric ion-atom collisions (for 3D Coulomb systems!). The obvious reason is that in both cases a strongly coupled two-state system ($1s\sigma/2p\sigma$ for the 3D Coulomb problem, binding/antibinding states for the 1D δ-model) dominates the dynamical evolution while the coupling to other states provides only "background" contributions.

The oscillations due to interference effects are expected to be strongest when the collision is symmetric. This is indeed what Fig. 4.1 shows. In the case of $Z_P = Z_T$, the oscillations are weakly damped compared to the asymmetric cases $Z_P \neq Z_T$.

The ionization probability, on the other hand, is rather smooth as a function of v in all cases (Fig. 4.1). The asymptotic behavior $v \to 0$ depends strongly on the charge asymmetry parameter γ. For the symmetric collision ($Z_P = Z_T, \gamma = 1$), $P_{ionization}$ tends to $\frac{1}{2}$ as $v \to 0$. This can be understood in the Born-Oppenheimer approximation in which the wave function is expanded in terms the ground state $|g\rangle$ and the excited state $|e\rangle$ (neglecting coupling to the continuum)

$$\psi(t) = C_g(t)|g\rangle + C_e(t)|e\rangle \tag{4.3}$$

where C_g and C_e are the state amplitudes. When $\gamma = 1$, the molecular orbitals are initially degenerate ($R = -\infty$, see Fig. 2.3). There is an equal amplitude mixing of the ground state and the excited state, i.e. $C_g(-\infty) = C_e(-\infty) = 1/\sqrt{2}$. As the two nuclei slowly move closer and eventually approach $R(t) \sim R_C$, the antibinding (excited state) orbital is promoted into the continuum (Fig. 2.3). As a result, the electron has a $|C_e|^2 = 50\%$ chance of being ionized (Fig. 4.1). If the electron initially is in the excited state $C_g(-\infty) = 0$ and $C_e(-\infty) = 1$, as is the case of $Z_P > Z_T, \gamma > 1$, $P_{ionization}$ will reach 1. When $Z_P < Z_T, \gamma < 1$, then $C_g(-\infty) = 1$ and $C_e(-\infty) = 0$, no ionization is expected. Consequently we find pure elastic scattering.

4.2 Forward and Backward Binary Electrons

The total ionization probability discussed in the previous section is obtained without any use of the scattering states (3.40). Full information on ionization is contained in the differential ionization probability $p(k)$ (Eq. (3.54)). Unlike the integral probabilities, $p(k)$ depends on the reference frame being used because the momentum k is subject to a Galilei transformation. We shall present the results in the usual laboratory frame in which the target is at rest. A Galilei transformation between the laboratory frame and the c.v. frame (see section 3.1) gives the following relationships

$$\begin{aligned} k &= k' + v/2 \\ p(k) &= p(k' + v/2) = p'(k') \end{aligned} \tag{4.4}$$

where k' and p' denote the electron momentum and ionization probability in the c.v. frame, respectively.

We first study the ionization spectra at an intermediate collision speed where $v/Z_T \sim 1$. Figure 4.3 displays the differential ionization probability $p(k)$ as a function of k/v. As a numerical check, the total ionization probability obtained by integrating $p(k)$ over k in the range of [-5,5] was found to agree with that calculated from Eq. (3.50) to within a relative accuracy of 10^{-4}. This directly verifies the numerical procedures employed as well as the consistency of the scattering states (Eq. (3.40)).

At $v = 1$ the collision speed is comparable to the orbital speed of the electron for $Z_T = 1$ (see (2.25)). One usually speaks of the intermediate speed region in atomic collisions when $v \sim Z_T$. In this region several features in Fig. 4.3 are evident. First and foremost, there is a broad hump in the forward direction around $k/v \sim 2$. It is mainly due to a hard collision between the massive projectile and the electron. Classically an electron initially at rest acquires a speed of $2v$ after such a hard, binary collision with the heavy projectile. Since the Compton profile, and hence the initial momentum distribution of the electron (see (2.26) and Fig. 2.2), peaks at $p = 0$, the ionization spectrum around $k/v \sim 2$ reflects that distribution. The exact position and the shape of the binary peak depends on many factors at intermediate collision speeds. The width of the Compton profile is the main reason that the binary hump in this case is smeared out. Since

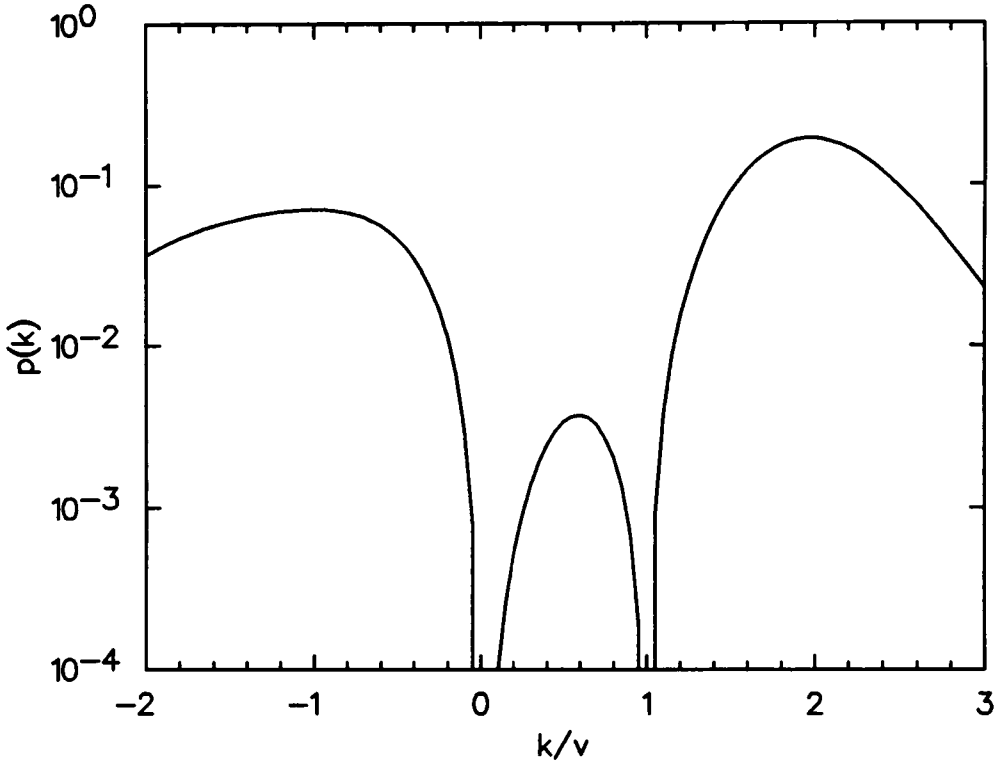

Figure 4.3: Differential ionization spectrum $p(k)$ as a function of k/v at $v = 1$, $Z_P = Z_T = 1$.

the broad binary peak is not clearly separated from the projectile and the target, simultaneous interactions with the two centers also distort the shape considerably. In addition, the binary electron must escape the target after the collision. Consequently the binary peak position will be shifted toward lower k than $2v$ because a portion of the ejected kinetic energy must be used to liberate the electron (its binding energy).

Also evident in Fig. 4.3 is another broad peak in the backward direction at $k/v \sim -1$. In the projectile rest frame this peak mirrors the binary peak in the laboratory frame discussed above. It can be interpreted as a sequence of capture and ionization. Referring back to Fig. 3.1 it is seen that the capture process starts to occur as the projectile approaches the target. Imagine that we are sitting in the projectile rest frame. The target is moving toward the projectile in the negative $\hat{x}$ direction. The bound state of the projectile,

which is initially empty, starts to be filled through the capture process. When the target comes close to the projectile, the captured electron suffers a hard collision with the target. In the same way a forward binary electron is created by projectile impact in the laboratory frame, a backward binary electron is produced by target impact in the projectile rest frame. The backward binary electron is separated from the target by v in momentum space, just as the forward binary electron is separated from the projectile by v. Since the creation of the backward binary electrons involves two steps, the magnitude with which it happens is expected to be smaller than the forward binary electron. This is clearly evidenced in Fig. 4.3.

The backward electron production requires electrons bound to the projectile prior to a close collision with the target. For bare projectile ions, this can be achieved only by capture before the hard collision. Since the capture probability quickly vanishes with increasing v (see Fig. 4.1), the backward binary peak will be small for large v's. If, however, the projectile carries electrons into the collision as it does in projectile ionization (to be discussed in detail in Chapters 5 and 6), one finds that the backward binary peak dominates at backward angles at high collision speeds.

From Fig. 4.3 (ignoring for the moment the structure between $0 \leq k/v \leq 1$) we can infer that emission in the forward direction is strongly favored. The area under the forward binary peak dominates the total emission spectrum. The strong presence of the binary encounter peak in the electron emission spectrum is due to the short ranged nature of the δ-potential and due to the confinement of motion in one dimension. For the same reason, the backward binary peak is clearly visible.

4.3 Missing Cusp

Figure 4.3 also shows that $p(k)$ decreases very rapidly near $k \sim 0$ and $k \sim v$. In fact $p(k)$ is identically zero at $k = 0$ and $k = v$. This indicates that the ionization spectrum of the δ-model does not have the cusp structure usually associated with target ionization in a Coulomb field, i.e. electron loss to continuum (ELC, $k \sim 0$) and electron capture to continuum (ECC, $k \sim v$).

The origin of the missing cusps can be traced to the property of the δ-potential. We recall from Chapter 2 that the δ-atom supports only one bound state. The density of states vanishes near the ionization limit. Furthermore, if

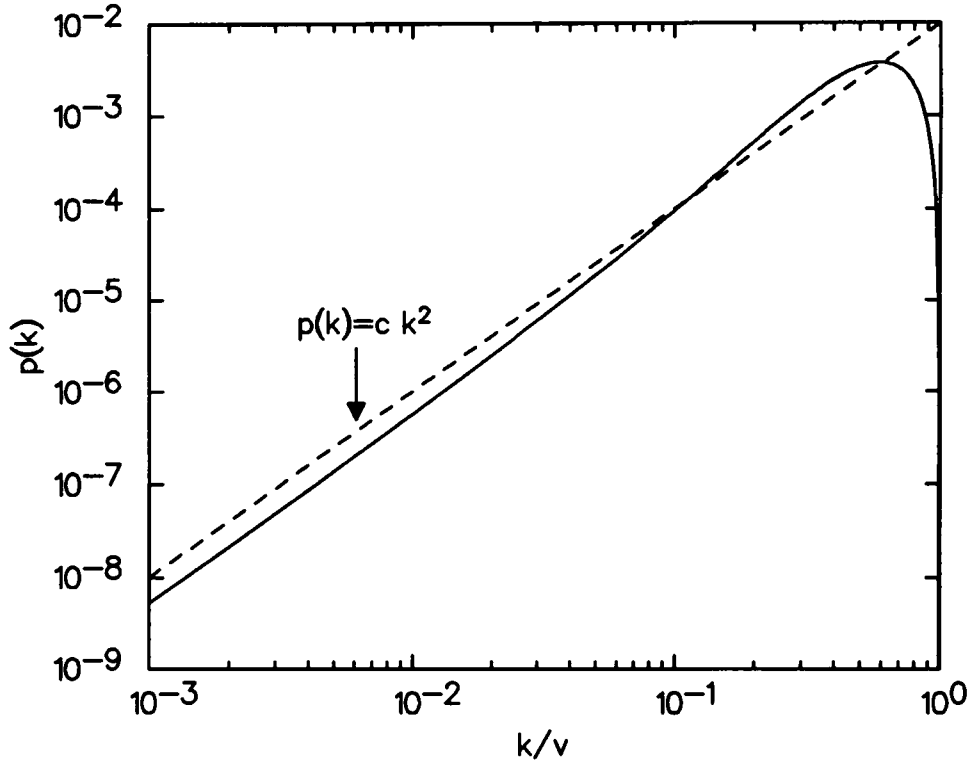

Figure 4.4: The ionization spectrum (——) near the target ionization threshold $k = 0$ and the projectile ionization threshold $k = v$ showing the missing cusps. The dashed line (- - -) shows the ck^2 dependence of the normalization factor according to Eq. (2.33).

the motion is restricted to 1D, as is the case in our 1D δ-model, the resulting normalization factor of the low lying continuum states behaves like k^2 for small k (Eq. (2.33)). Figure 4.4 displays the ionization spectrum near the normal ELC cusp $k \sim 0$. Clearly $p(k)$ decreases quickly with decreasing k. One expects that as $k \to 0$, $p(k)$ would approach a straight line of slope 2 on a logarithmic scale because of the normalization factor. Fig. 4.4 confirms this behavior of $p(k)$ for small k. For $k \leq 0.05$, $p(k)$ closely follows the straight line ck^2. When k is small enough (about $k < 0.01$), no significant deviation from the k^2 law can be detected by visual inspection. This demonstrates that the the missing cusp is a consequence of pure two-body final state interactions [68] because in the limit $k \to 0$, the behavior of $p(k)$ is completely determined

by one center(the target). Similarly if one examines $p(k)$ near the ECC ($k \sim v$, not shown in Fig. 4.4), a $(k-v)^2$ behavior can be found.

It is interesting to compare the missing cusps of the δ-model to the anticusps of antiparticles, such as the antiproton. It has been speculated that for ionization by antiproton impact, the usual ECC cusp would be replaced by a "dip" [69, 70]. Again it owes its origin to the normalization factor. It can be shown that the Coulomb normalization factor (Eq. (2.32)) approaches $N_c(k \to 0) = (2\pi|Z|/k)\exp(-2\pi|Z|/k)$ for antiparticles ($Z < 0$, the Gamov factor for repulsive Coulomb interaction). As $k \to 0$ it rapidly decreases to zero (an essential singularity at $k = 0$), thereby creating a depletion of electrons, usually referred to as an "anticusp". The obvious reason is that the repulsive potential strongly suppresses electrons with small relative momentum. The repulsive potential has one feature in common with the δ-potential in that the density of bound states near the continuum vanishes because a repulsive potential posseses no bound states. In the case of the attractive δ-potential, $-Z\delta(x)$, on the other hand, the interaction at $x = 0$ is so strong that the electron of $k \sim 0$ will be recaptured into the bound state. As we shall see later the recapture mechanism does not operate in the 3D δ-model where the motion is not confined in 1D.

4.4 $v/2$ Electron Emission

4.4.1 Mechanism

Another structure, already seen in Fig. 4.3 in the last section but not yet discussed, is the peak in between the missing cusps. The peak is roughly near $k/v \sim 0.6$ (Fig. 4.3), which is very close to $v/2$. The fact that $p(k)$ peaks near $v/2$ at intermediate collision speeds immediately leads us to the possible identification of the $v/2$ electrons in the ionization spectrum. However, before we can make a definite statement caution must be exercised as will become clear in the following.

What makes the identification as $v/2$ electron emission difficult is the appearance of missing cusps (Fig. 4.3). It has been shown in the last section that $p(0) = p(v) = 0$. Elementary calculus asserts that there is at least one maximum in the interval $[0, v]$ for the positive definite smooth function $p(k)$. One has to be certain that the maximum of $p(k)$ near $k = v/2$ is not a trivial

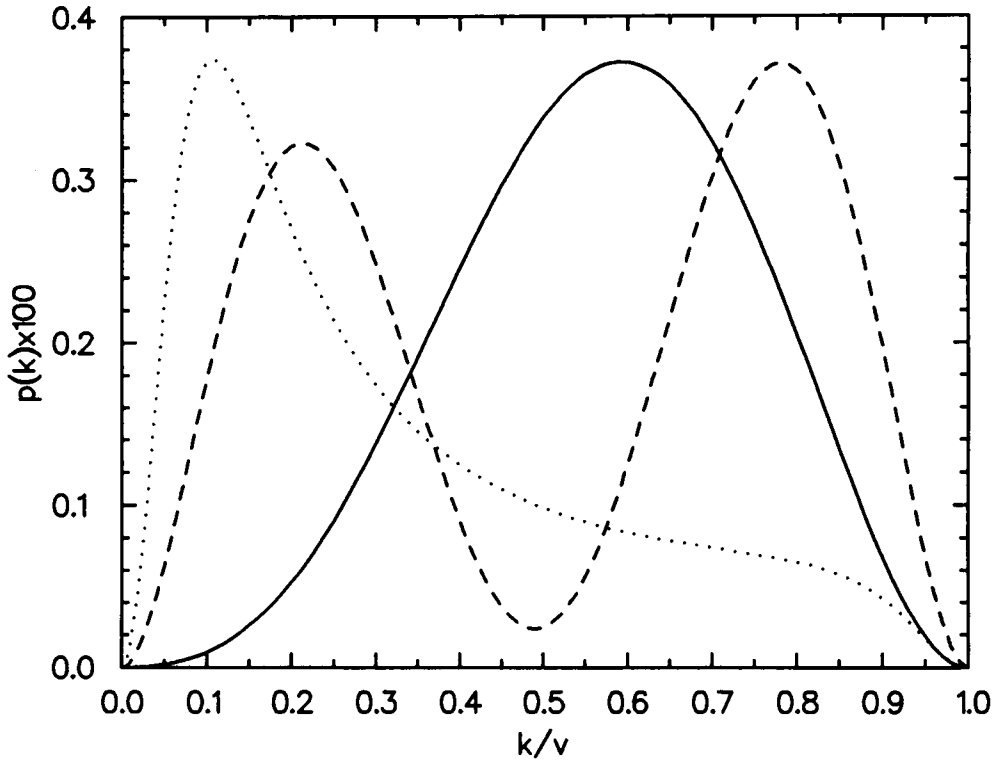

Figure 4.5: The ionization spectra between $k = 0$ and $k = v$ for $Z_T = Z_P = 1$ at three collision speeds. $v = 1$ (——), $v = 0.3$ (- - -), and $v = 10$ ($\cdots\cdots$). The latter two curves are normalized to the $v = 1$ curve such that the maxima are equal in magnitude.

consequence of vanishing probability of $p(k)$ at $k = 0, v$. We therefore show in Fig. 4.5 the spectra in the interval $[0, v]$ for three collision speeds. Large differences exist among the three cases. At an intermediate speed ($v = 1$), there is a single, well defined peak around 0.6. The single peak bifurcates into two peaks at low speed ($v = 0.3$). At high speeds ($v = 10$), a very skewed peak appears at low momentum $k \sim 0.1$. In addition, there is also a shoulder structure near $k = 0.9$. The double peaks at low speed are due to interference effect between the two centers. The wave function expansion (3.40) converges very slowly with respect to the summation index n for small v because of the recurrence relations (3.43). There are many quasi-stationary states with long life times ($\sim 1/nv$, see Eq. (3.24)). Provided the collision is

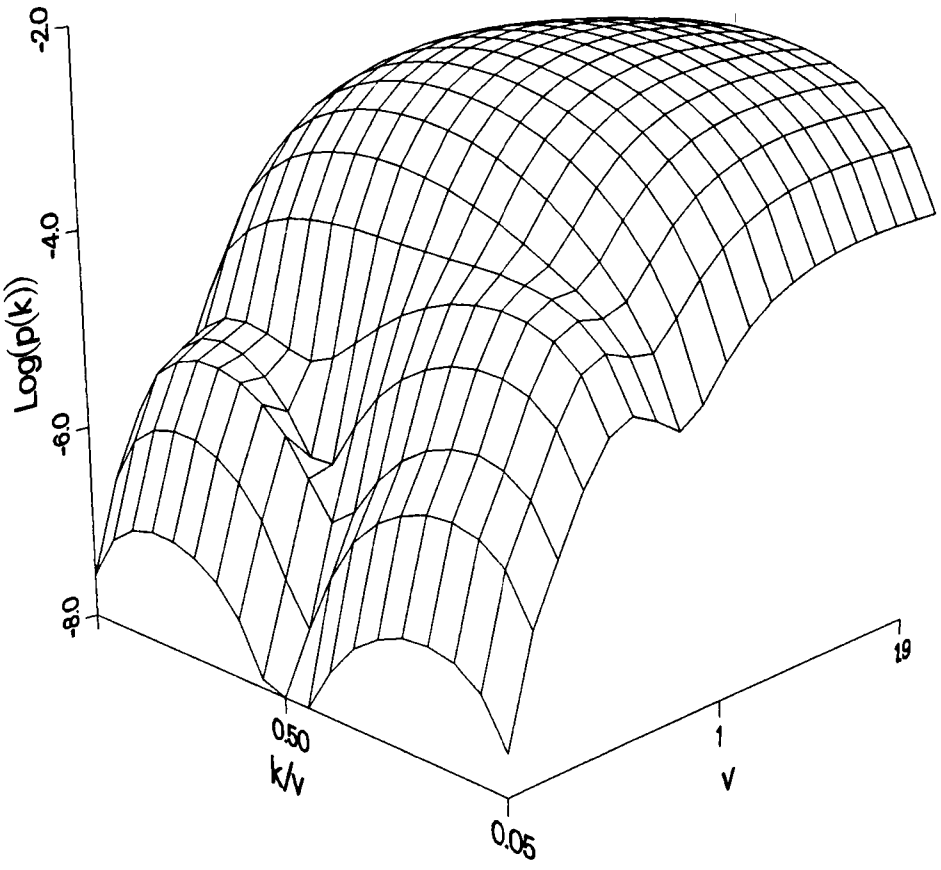

Figure 4.6: Surface plot of ionization spectrum between $k = 0.05v$ and $k = 0.95v$ for $Z_T = Z_P = 1$ as a function of the collision speed $v \in [0.1, 2]$.

slow enough and symmetric enough ($Z_P \sim Z_T$), interference becomes strong.

The dependence of $p(k)$ ($k \in [0, v]$) on v is better illustrated in Fig. 4.6 in which $\log p(k)$ is presented as a surface plot of k and v. At low speeds $v \leq 0.7$ the formation of double peaks sets in. Let us for the sake of brevity refer to the peak at smaller k as the low velocity peak, and the peak at larger k as the high velocity peak. At first the low velocity peak is larger than the high velocity peak. As v decreases, the relative heights of the peaks are inverted with the high velocity peak becoming larger than the low velocity peak. If a cut is made at $v = 0.3$ in Fig. 4.6, the dashed line in Fig. 4.5 will be recovered, which shows that the high velocity peak at $k/v \sim 0.8$ is larger than the low velocity peak at $k/v \sim 0.2$. The valley (Fig. 4.6) between the two peaks

also becomes deeper as $v \to 0$, an indication of stronger interference. The double peaks disappear above the intermediate collision speed ($v > 0.7$). The highest single peak can be found around $v \sim 1.7$.

Figs. 4.5 and 4.6 demonstrate that the ionization spectrum depends sensitively on the collision dynamics operating at different speeds. Only at intermediate speeds does the spectrum show a peak around $k = v/2$ ($k' \sim 0$ in c.v. frame). The regime of v in which $v/2$ electron emission is observed is consistent with approximate calculations performed on real 3D systems [8, 9, 10]. In view of the sensitive dependence on the collision speeds, we are justified to identify this feature as the $v/2$ electron emission. We can define the integral probability of $v/2$ electron emission as the area in the interval $[0, v]$ as

$$P_{v/2} = \int_0^v p(k)dk. \tag{4.5}$$

This definition is appropriate for the δ-model because of the missing cusps, which will not contain spurious contributions from other sources like the Coulomb cusps. At $v = 1.7$, where the $v/2$ peak is the highest (Fig. 4.6), the $P_{v/2}$ is about 3% of the total ionization probability.

The identification of $v/2$ electrons in the δ-model is a clear indication that such a feature is not exclusively due to long range potentials as had been previously thought [11, 14]. The mechanism with which the $v/2$ electrons are produced in short range interactions can be understood in terms of quasi-molecular states. As has been shown in Chapter 2 (see Fig. 2.3), the δ-molecule has at large internuclear distances two bound states, the binding state and the antibinding state. The latter is promoted into the continuum at a critical distance R_c (Eq. (2.40)). In the collision process the static molecular picture is not exactly valid anymore because the system is time dependent. However, provided that the collision speed v is not too large, we can describe the collision in the Born-Oppenheimer approximation (BOA) [3]. In the BOA the electronic Hamiltonian at time t is solved assuming a fixed internuclear separation R. The states thus obtained are referred to as the quasi-molecular states. The collision dynamics is then represented in terms of couplings between quasi-molecular states. The population of the quasi-molecular states at time t can be calculated by projecting the exact scattering state (Eq. (3.10)) onto the states of the quasi-molecule.

The probabilities for occupying the binding and the antibinding orbitals of the quasi-molecule are shown in Fig. 4.7. On the incoming part of the

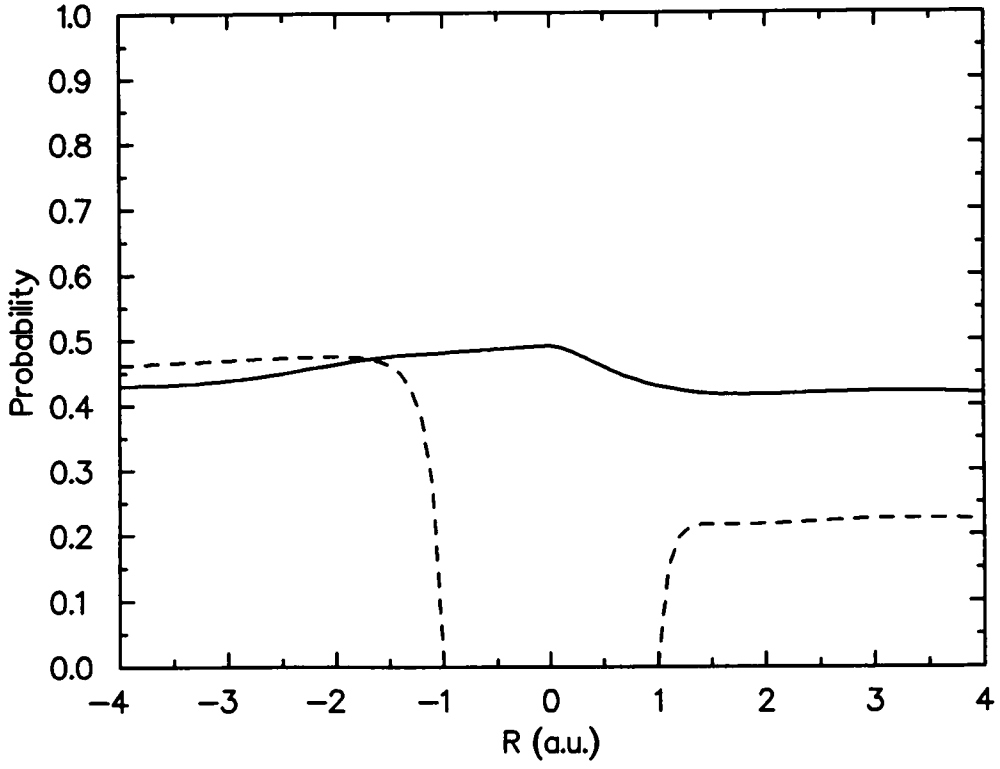

Figure 4.7: Population probability of quasi-molecular states as a function of internuclear distance for $Z_P = Z_T = v = 1$. ——, binding state; - - -, antibinding state.

trajectory of the projectile ($R < 0$), the occupation probability approaches approximately $\frac{1}{2}$ at larger negative R. We recall that the molecular states are degenerate at large $|R|$ (Fig. 2.3). If the incident speed is small, we expect the probability to be very close to $\frac{1}{2}$. The fact that the probability is not very close to the expected value $\frac{1}{2}$ (from Fig. 4.7), even at $R = -4$ where the initial electronic state at the target is hardly perturbed (see Fig. 3.1), is a direct measure of the influence of the Galilei translation factor (Eq. (3.9)) missing in the representation of the quasi-molecular states. The treatment of translation factors in a BOA has been the subject of intense research [71]. We point out that the present exact treatment of the δ-model would allow, within the simple model, a detailed test of several proposed "switching" functions for the treatment of translation factors within the framework of a BOA basis

expansion. As the projectile and the target approach each other at the critical distance $R = -R_c$ the occupation of the antibinding state drops sharply to zero (dashed line in Fig. 4.7), indicating the promotion to continuum. At the same time the occupation probability of the binding state increases only slightly (solid line). This also indicates that electron emission occurs predominantly by direct promotion of the antibinding state into the continuum states. On the outgoing part of the trajectory ($R > 0$), the population of the binding state decreases at small distances $R < R_c$ before the antibinding state is restored at $R = R_c$, thereby enhancing the ionization probability. Once the antibinding state is restored $R > R_c$, it is rapidly filled by recapture, however with a significantly reduced occupation number as compared to the incoming part of the trajectory. The forward-backward asymmetry as well as the almost discontinuous edge in the population amplitude of the binding state at $R = 0$ illustrate the non-adiabaticity of the collision process. The interference between the two molecular orbitals is responsible for producing the structures in the ionization spectrum (Fig. 4.5). Subtracting from unity the sum of the two occupation numbers (at $R = 4$ in Fig. 4.7) and taking into account the influence of the translation factors yields ~ 0.3 for the total ionization probability. This number agrees well with the exact total ionization probability ~ 0.32 (as read off from Fig. 4.1 at $v = 1$). While in detail quite different, the quasi-molecular orbital promotion mechanism for ionization is present both in the 1D δ-model and the 3D Coulomb problem. This mechanism is effective at small distances irrespective of the long range nature of the potential. The low-energy portion of the quasi-molecular ionization spectrum ($k' \sim 0$ in c.v. frame) leads to the enhancement near $v/2$ in the labframe. This ionization process at small distances can be considered to be the likely candidate for the primary mechanism generating the wavepacket which is then subject to post-collisional distortion [11, 72] in the 3D Coulomb problem.

Having discussed the $v/2$ emission in the 1D δ-model we now examine the same model in 3D. The momentum can now have any direction. Since the $v/2$ electron emission is expected to be confined to forward angles, Fig. 4.8 displays only the spectrum at 0^0 and 180^0 . Comparing Figs. 4.3 and 4.8 reveals the most noticeable difference, i.e., the 3D case has no missing cusps. The exact zero of $p(0)$ and $p(v)$ in 1D is absent in 3D since the recapture mechanism for a one-dimensionally confined motion does not operate. Again this is due to the final state interactions as it can be shown that the nor-

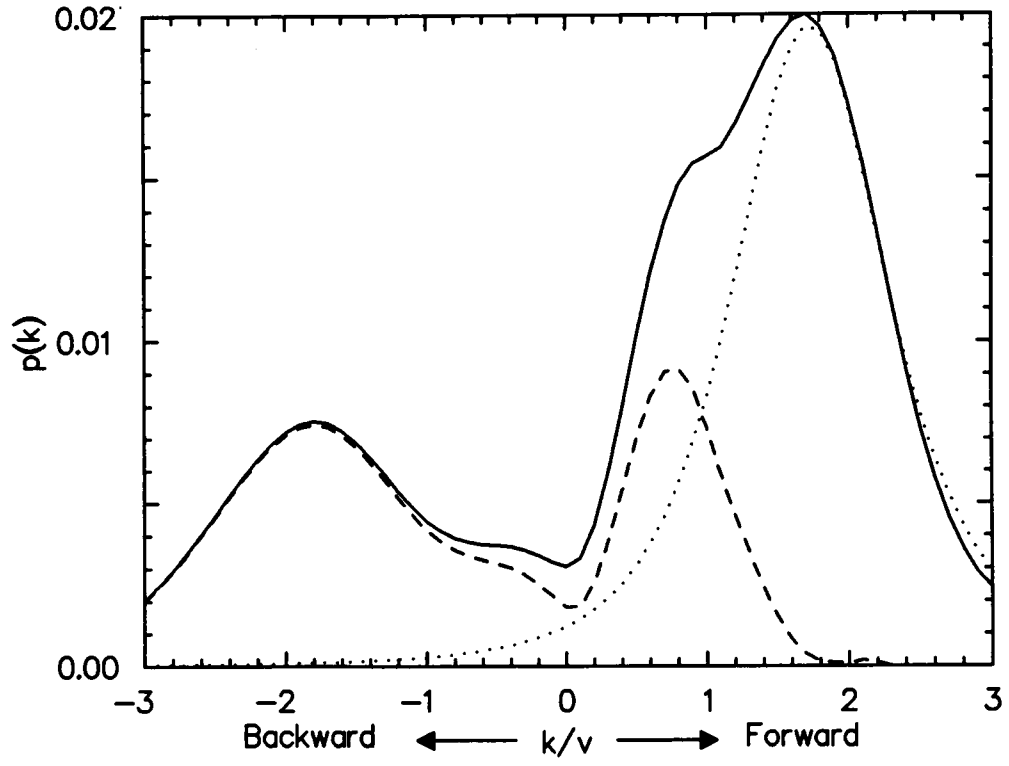

Figure 4.8: Differential ionization spectrum $p(k)$ of the 3D δ-model in forward ($k > 0$, 0^0) and backward ($k < 0$, 180^0) directions as a function of k/v at $v = 1$, $Z_P = Z_T = 1$. The exact spectrum (——) is decomposed into two parts, the binary encounter peak ($\cdots\cdots$), and the residual part (- - -) determined by subtracting the binary peak from the whole spectrum (see text).

malization factor (or the so-called "enhancement" factor [68]) given by the inverse of the Jost function for the 3D δ-potential is 1 [73]. Therefore there is no ECC at $k = v$ or ELC at $k = 0$ because the potentials are of short range. But in both cases the spectra are characterized by forward $k \sim 2v$ and backward $k \sim -2v$ binary peaks.

Due to the lack of missing cusps the identification of $v/2$ electrons in 3D is not as obvious as in 1D. However the spectrum in Fig. 4.8 does possess a shoulder in $0 < k < v$ (This structure was present but not analyzed in Ref. [63]). At $Z_T = v = 1$ the forward binary is a rather broad and overlaps with the $v/2$ electrons. It is desirable to separate the two spectra to get

a clearer picture. To do so, we need to decompose the spectrum into a binary electron component and a residual component. Since the forward binary peak is due to a head-on collision with the projectile, the appropriate procedure would be to subtract the first Born approximation from the whole spectrum. Unfortunately, in the 3D δ-model (unlike the 1D case) the first Born approximation for the ionization probability at zero impact parameter is logarithmically divergent. We therefore choose instead the Compton profile of the initial state, centered at $2v$ in the forward direction. The overall intensity is treated as the only adjustable parameter for the binary electrons (dotted line ($\cdots\cdots$) in Fig. 4.8). The residual spectrum (dashed line) shows a peak at $k \sim 0.8v$ in close agreement with the 1D case. It is a clear indication of $v/2$ ionization mechanism in 3D. The existence and the position of the peaks have been verified by replacing the Compton profile with a Lorentzian line shape for the binary peak. The difference spectrum in $k \in [0, v]$ is rather insensitive to the method of subtraction. The enhancement of the spectrum near $k \sim -0.5v$ is probably due to the collisional reflection of the $v/2$ electron wavepacket at the target but no conclusive evidence has been found.

4.4.2 Three-body Effects

In the last section we have discussed the ionization spectrum for the symmetric collisions $Z_P = Z_T$ and its dependence on the collision speed v. The $v/2$ electron emission is thought to be an intrinsic three-body effect [10] caused by comparable interaction strengths [18]. We focus our discussion of three-body effects here on the $v/2$ electron emission. The same effects in ion-atom collisions are often referred to as two-center effects. We shall discuss this aspect in a later chapter in connection with projectile ionization.

To see how the $v/2$ emission evolves as the interaction strengths change, we show in Fig. 4.9 the spectrum in $k \in [0, v]$ as a function of the asymmetry parameter $\gamma = Z_P/Z_T$ at the intermediate collision speed $v = 1$. The intensity of the emission varies greatly as a function of γ. The highest yield of $v/2$ electrons happens at $\gamma = 0.5$. It drops sharply to zero at $\gamma = 0$ since for $Z_P = 0$ there is no interaction and thereby no ionization. The intensity also decreases rapidly from $\gamma = \frac{1}{2}$ to $\gamma = 2$, at which point it levels off slowly as γ increases further. The fact that most intensity is concentrated in the interval $\gamma \in [\frac{1}{2}, 2]$ is a clear indication that the $v/2$ emission is caused by comparable interaction strengths. The shape and the peak position also

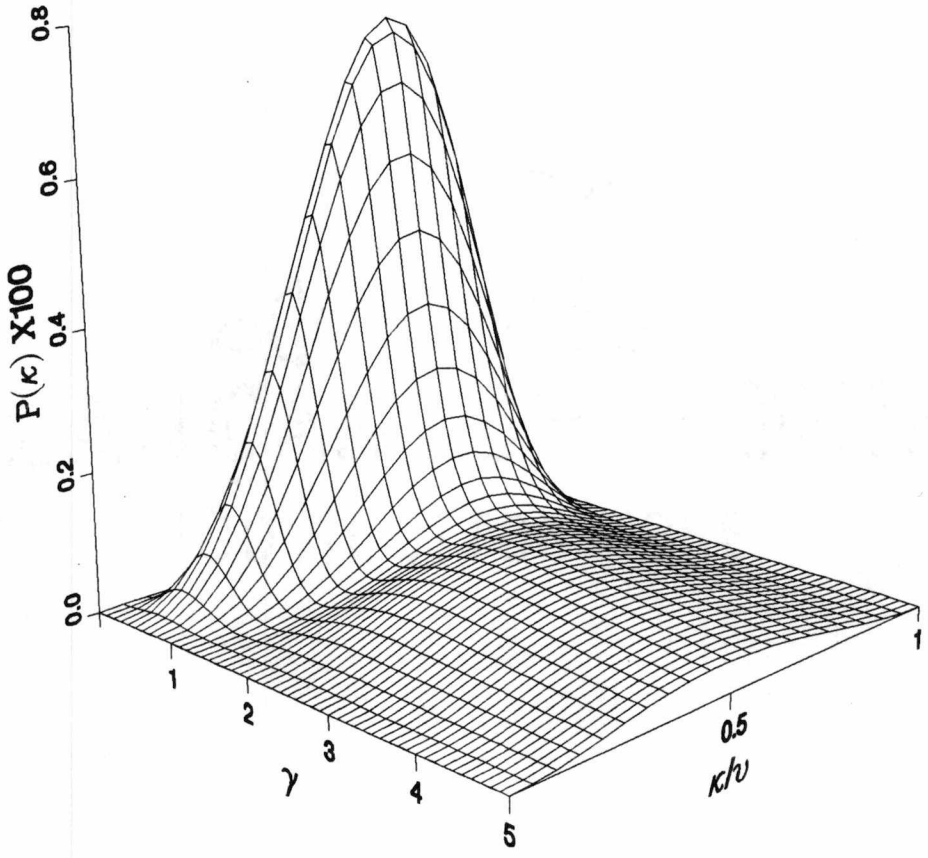

Figure 4.9: Surface plot of ionization spectrum between $k = 0$ and $k = v$ for $v = 1$ as a function of the collision asymmetry parameter $\gamma = Z_P/Z_T$.

changes considerably over the entire range of γ. One can see that the width of the peak broadens and the top of the ridge shifts to smaller k as γ increases. The precise peak position k_{max} of $v/2$ emission is shown in Fig. 4.10. At $v = 1$, k_{max} is not a monotonic function of γ. It decreases first but rises to a local maximum at $\gamma \sim 1.5$, and then slowly decreases again. The overall trend is to shift the peak position to lower k for increasing γ, i.e. the weaker the projectile charge ($\gamma \to 0$), the closer the peak lies to the projectile ($k_{max} \to v$) in momentum space. On the other hand, if the interaction with the projectile becomes stronger, k_{max} tends to be further away from the projectile. The dependence of the $v/2$ peak position possesses a striking similarity to the corresponding peak shift reported experimentally

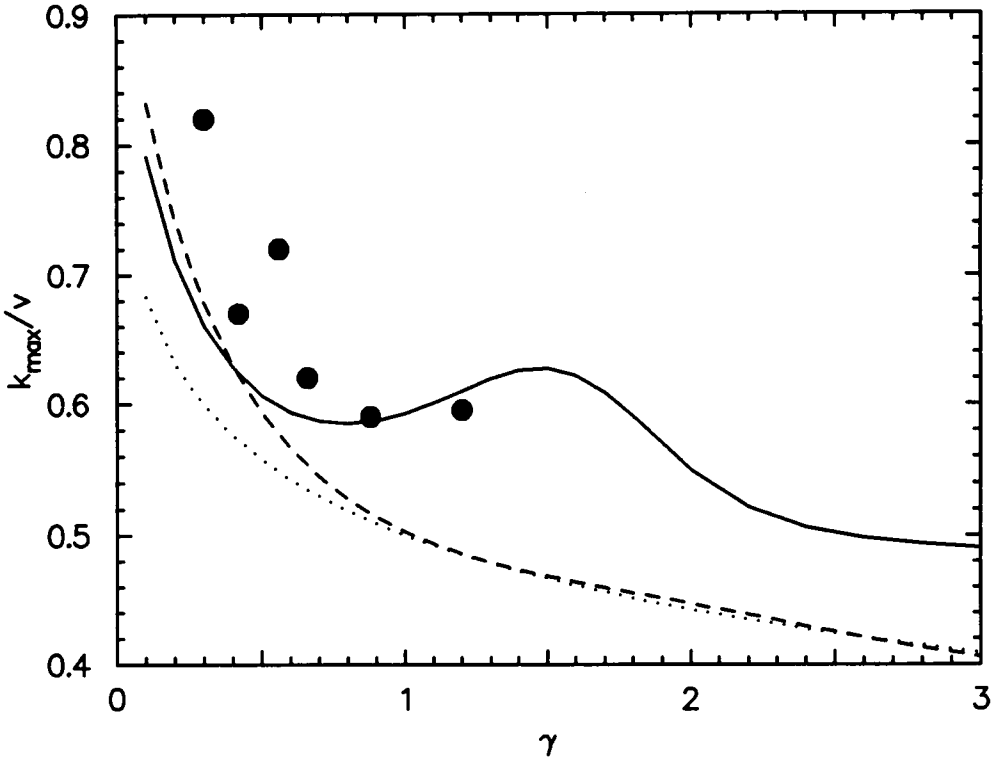

Figure 4.10: The peak position of the $v/2$ emission as a function of $\gamma = Z_P/Z_T$ for $v = 1$ (——), $v = 2$ (- - -), and the improper saddle ($\cdots\cdots$). •: Experimental data of Ref. [74] (see text).

in the 3D Coulomb problem [74, 16]. In the experiment [16] proton ($Z_P = 1$) and He^{++} ($Z_P = 2$) are incident on a variety of targets at 100 keV/u ($v = 2$). The peak position of the $v/2$ electrons is determined as a function of Z_P/Z_T, with Z_T being the effective target charge determined from Slater's screening constants. The result is shown in Fig. 4.10. For comparison we also show the peak position computed at $v = 2$ for the δ-model. It is surprising that the long range 3D Coulomb problem agrees qualitatively rather well with the short range δ-model in the γ dependence of the peak position.

We show now that the dependence is related to the motion of an improper "saddle" point in the δ-model. A proper saddle point is a point in space where the force due to a (analytical) potential is zero and the stability matrix has positive eigenvalues. Obviously there can be no proper saddle point in the

δ-model because of zero-ranged potentials. But there exists an "improper" saddle point in the weak-limit representation of the δ-potentials in terms of continuous functions. In the weak limit, the electronic potential (Eq. (2.1)) can be written as

$$\begin{aligned} V(x) &= -Z_T\delta(x) - Z_P\delta(x-R) \\ &= -\lim_{\eta\to 0}\frac{\eta}{\pi}\left[\frac{Z_T}{\eta^2+x^2}+\frac{Z_P}{\eta^2+(x-R)^2}\right]. \end{aligned} \tag{4.6}$$

The choice of a correlated limit ($\eta_T = \eta_P = \eta$ in (4.6)) preserves for any infinitesimal $\eta > 0$ and for a homonuclear system ($Z_T = Z_P$) the "gerade" symmetry of the molecular potential and for a heteronuclear system ($Z_T \neq Z_P$) the charge ratio $\gamma = Z_P/Z_T$ as the order parameter of the relative strength of the atomic potentials. Differentiation of $V(x)$ in (4.6) with respect to x gives for finite but small η the point of zero force

$$x_{saddle} = \frac{R}{1+\gamma^{1/3}} \tag{4.7}$$

independent of η, so that x_{saddle} remains well defined as $\eta \to 0$. The velocity of the improper saddle point is related to the collision speed via

$$v_{saddle} = dx_{saddle}/dt = \frac{dR/dt}{1+\gamma^{1/3}} = \frac{v}{1+\gamma^{1/3}}. \tag{4.8}$$

v_{saddle} (Eq. (4.8)) lies between 0 ($v_{saddle}(Z_P \to \infty) \to 0$) and v ($v_{saddle}(Z_T \to \infty) \to v$). The universal curve, v_{saddle}/v, for the classical motion of the saddle point is displayed in Fig. 4.10. It reproduces the overall dependence of the position of the $v/2$ peak qualitatively quite well. Clearly, the nonmonotonic behavior of the exact $v = 1$ curve is not described by this simple classical model. It is interesting to note that the motion of the saddle point in the 3D Coulomb problem follows from Eq. (4.8) simply by replacing the exponent 1/3 by 1/2. The behavior is qualitatively the same as the δ-model. To the extent that the experimental data are reliable (see Fig. 4.10), which is not clear at this time, the analogous behavior of the classical motion of the saddle point between the Coulomb problem and the δ-model would not only explain the qualitative agreement of k_{max} between theory and experiment, but would also underscore the notion that the electrons are "stranded" near the saddle

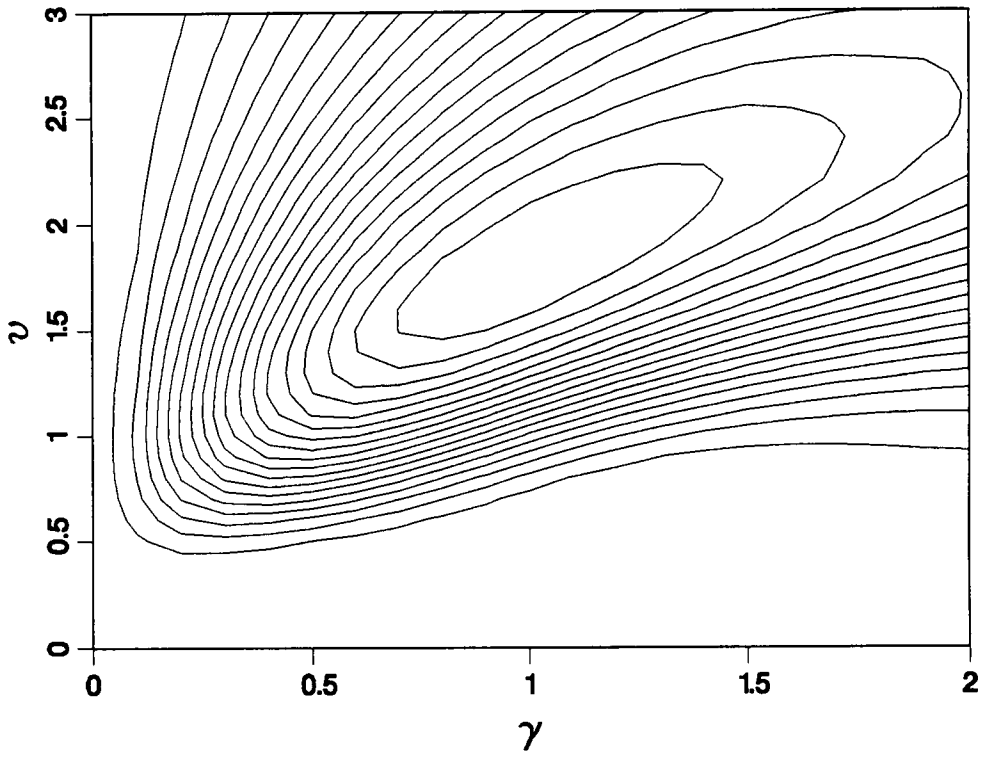

Figure 4.11: The contour plot for the yield of $v/2$ electron emission $P_{v/2}$ (Eq. (4.5)) as a function of $\gamma = Z_P/Z_T$ and v.

point and finally escape with a velocity comparable to v_{saddle}. We note that our results showing the strong three-body effects on the emission spectrum near $v/2$ region are valid irrespective of the recent controversy concerning the validity of the experimental data.

The yield of $v/2$ electrons defined by the integral probability $P_{v/2}$ (Eq. (4.5)) is shown by the contour plot in Fig. 4.11 as a function of γ and v. $P_{v/2}$ is largest at $[\gamma, v] \simeq [1.2, 1.8]$. There is a relatively flat plateau surrounding that point, which implies that the $v/2$ emission occurs predominantly for comparable interaction strengths at intermediate collision speeds. As γ increases, the interaction with the projectile becomes stronger. In order to maintain comparable interaction strengths for $v/2$ emission, the collision speed v must also increase appropriately. The net effect is to reduce the interaction time, thereby reducing the effective interaction strength of the

projectile. As illustrated in Fig. 4.11 the ridge (where $P_{v/2}$ has a local maximum) extends along an almost linear curve $v(\gamma)$. The contribution of the $v/2$ electron emission to the total ionization in the range of v, γ studied here varies from $\sim 0.1\%$ to $\sim 10\%$.

4.5 Multiple Scattering Peaks

The ionization spectra presented so far (Figs. 4.3 and 4.8) all have large forward and backward binary peaks. In Chapter 3 the formation of a sequence of multiple scattering peaks was discussed in connection with the solutions of the δ-model (see page 35). We show numerical evidence of it in this section.

Plotted in Fig. 4.12 are the multiple scattering peaks in the ionization spectrum of the 1D δ-model for two cases. In both cases the projectile charge is chosen to be large compared to the target charge for reasons which will become clear in a moment. There is clearly a sequence of higher order binary peaks. The ordinary binary encounter peak located at $k = 2v$ results from a single head-on collision between the target electron and the projectile. It is described by a first order expansion of the transition operator

$$T_1 = V_P \tag{4.9}$$

where $V_P = -Z_P\delta(x - vt)$ is the electronic interaction with the projectile. The transition amplitude can be written in the plane wave Born approximation as

$$a_1(k) = \langle k|T_1|\phi_T\rangle \tag{4.10}$$

where $|k\rangle$ denotes the plane wave and ϕ_T is the initial target bound state. Eq. (4.10) does not include any final state interaction with the target. The prominence of the binary encounter peak for ion-atom collisions with δ-potentials results from the fact that hard collisions are dominant for short range potentials as well as from the absence of ELC and ECC peaks. The peaks observed at $k = -2v$ correspond to double scattering by which the binary electrons travelling with $k = 2v$ are scattered again at the target. Since the target is infinitely heavy, the electrons are simply reflected to the backward direction at $k = -2v$. The double scattering corresponds to second order process

$$T_2 = V_T G_0^+ V_P \tag{4.11}$$

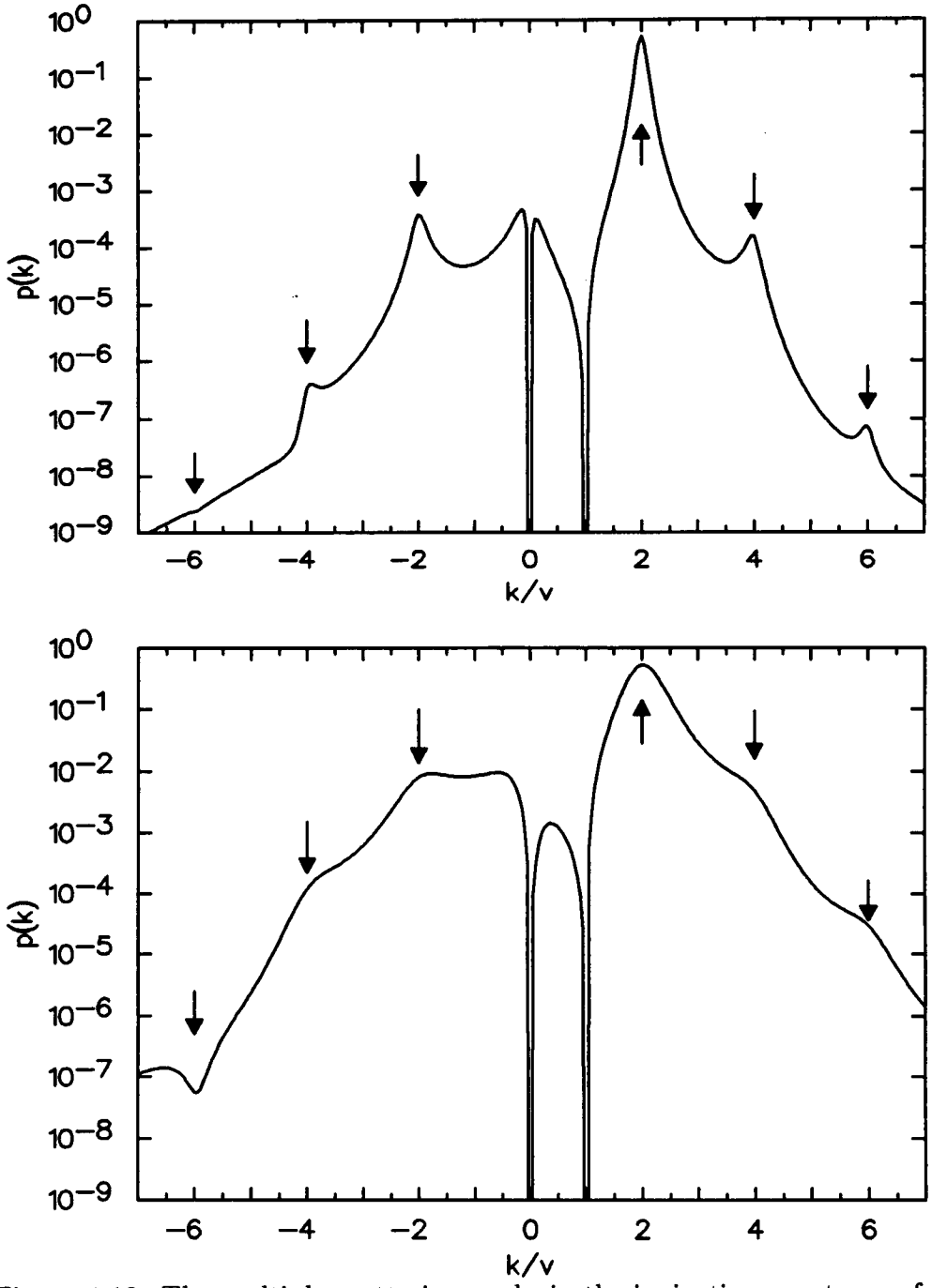

Figure 4.12: The multiple scattering peaks in the ionization spectrum of the 1D δ-model. The parameters chosen are $Z_P/Z_T = 16, v = 8$ for the top figure, and $Z_P/Z_T = 5, v = 2$ for the bottom figure. The arrows mark the expected positions of the scattering peaks (or dips).

where $V_T = -Z_T\delta(x)$ is the target potential and G_0^+ is the free-particle Green's operator.

The T operator expansions (4.9) and (4.11) contain contributions up to first order in both V_P and V_T. Without much additional effort an improvement can be made such that the T operator contains contributions to first order in V_P but to infinite order in V_T. One can do this simply by adding (4.9) and to (4.11) and replacing G_0^+ in (4.11) by G_T^+ (the Green's operator in the target potential) to obtain

$$T^{(1)} = T_1 + T_2 = (1 + V_T G_0^+)V_P \simeq (1 + V_T G_T^+)V_P. \tag{4.12}$$

The corresponding transition amplitude is given by

$$a_{B1}(k) = \langle k|T^{(1)}|\phi_T\rangle = \langle \psi_k^-|T_1|\phi_T\rangle, \tag{4.13}$$

which is the full first order Born approximation. Note that in (4.13) the application of the operator $(1 + G_T^+V_T)$ to a plane wave produces an exact continuum eigenstate of the target ψ_k. Consequently the final state interaction with the target is included exactly. The ionization spectrum to first order in V_P but zero order in V_T (plane wave final states Eq. (4.10)), and that to first order in V_P but infinite order in V_T (Eq. (4.13)) are shown in Fig. 4.13 for $Z_P/Z_T = 1$ and $v = 2$. The exact ionization spectrum is also shown for comparison. Both the first order expansion (4.10) and the Born approximation (4.13) reproduce the primary binary peak ($k = 2v$) very well. It confirms that major contribution to the primary binary peak comes from the operator V_P. In addition, the full Born approximation also gives a good description of the double binary peak ($k = -2v$) where Eq. (4.10) fails completely. This is so because the mechanism required for the generation of the double binary peak (i.e. primary binary electrons deflected once more at the target) is contained in (4.13) but missing in (4.10). The full Born approximation also describes well the ionization spectrum close to the target ($|k| \sim 0$) including the exact zero of $p(k)$ at $k = 0$. This is not surprising since (4.13) uses the exact scattering state of the target. However, it does poorly around the projectile ($k \sim v$) and around the $v/2$ region. The poor agreement for the former is understood because (4.13) is only first order in V_P. From Fig. 4.13 it can be seen that Eq. (4.10) is a good approximation only around the primary binary peak as expected. The non-orthogonality of the plane wave and the target continuum state is the main reason for the large discrepancy between

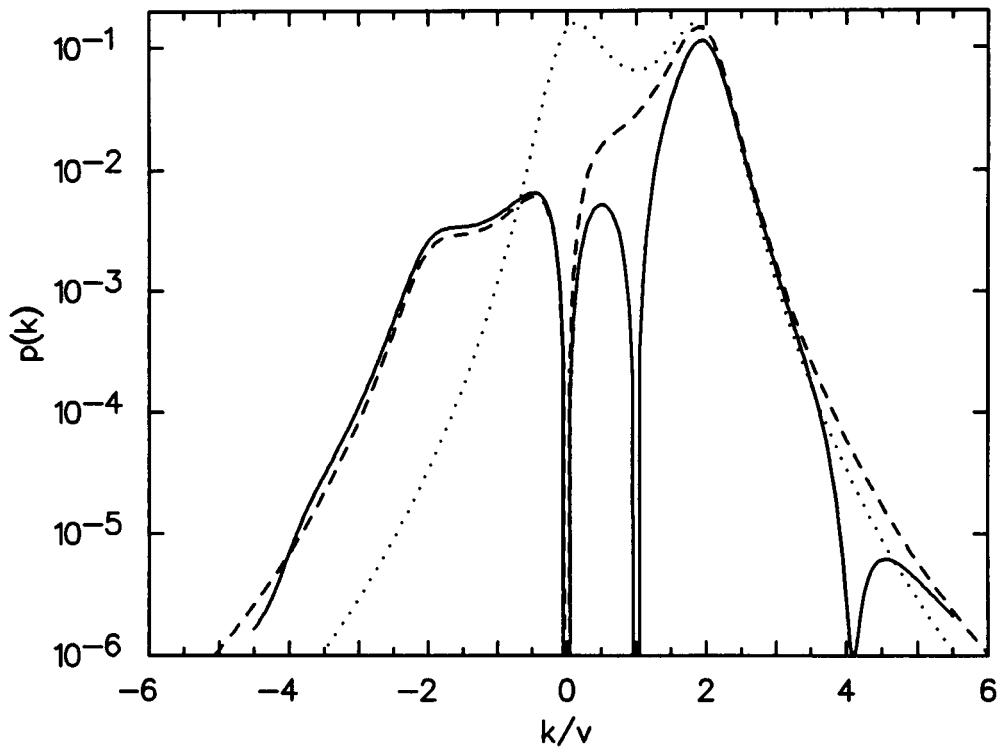

Figure 4.13: The Born approximation for the ionization spectrum of 1D δ-model for $Z_P/Z_T = 1$ and $v = 2$. The solid line (——) is the exact calculation, and the dashed line (- - -) is the full Born approximation (Eq. (4.13)). The dotted line ($\cdots\cdots$) shows the result of the plane wave Born approximation from Eq. (4.10).

Eq. (4.10) and the exact spectrum in the low momentum region around the target $k \sim 0$. It shows the importance that the final and initial states be orthogonal in order to describe the low energy electrons accurately in target ionization. The large deviations of the two approximations (Eqs. (4.10) and (4.13)) from the exact treatment at $v/2$ region indicates that $v/2$ emission is truly due to three-body dynamics which the finite order expansions in one of the two potentials (Eq. (4.9) and (4.12)) lack.

Following the line of argument leading to the primary binary and the double binary peaks, it can be seen that subsequent head-on collisions alternately with the projectile and the target lead to a sequence of resonant

structures in the forward and backward direction at momenta

$$k = \pm 2nv (n = 1, 2...) \tag{4.14}$$

with rapidly decreasing amplitudes. They originate from partial amplitudes T_{2n-1} in the forward direction and T_{2n} in the backward direction of the Born series. The resonant structures are either peaks or dips depending on the relative sign of these multiple scattering amplitudes and the first order amplitude they interfere with either constructively or destructively (see the dips at $k = -6v$ in the bottom figure of Fig. 4.12 and at $k = 4v$ in Fig. 4.13). The full Born approximation (4.12) (see Fig. 4.13) falls monotonically for $|k| > 2v$ and fails to describe the structures at $k = \pm 4v$ because they require terms of second order in V_P missing in (4.12). Note that going from the top figure of Fig. 4.12 to the bottom figure on to Fig. 4.13, the prominence of the peaks decreases. The peaks are most evident in the top figure of Fig. 4.12 where Z_P is the largest. The reason is that the generation of the primary binary electrons is the source to all the subsequent higher order peaks. The larger the Z_P, the more primary binary electrons are emitted. Since each additional scattering reduces the amplitude, Z_P must be large so that more peaks are visible.

For the δ-model in 3D one expects to see similar structures. Fig. 4.14 illustrates the ionization spectrum of the 3D δ-model for $Z_P = Z_T = 10, v = 2$. It is quite remarkable that the multiple knock-on structures are still observable in 3D in view of the rapid angular spread of the binary electron distribution for multiple binary collisions. Of course the choice of zero impact parameter accentuates the contributions from multiple scattering. For the same reason we have observed multiple knock-on peaks (and humps) in proton impact ionization of hydrogen in a third order Born expansion of the T operator (taking only the energy conserving on-shell parts).

Since the multiple knock-on process involves simultaneous collisional interactions with both the target and the projectile they are intrinsic three-body scattering effects as well. Thomas scattering for capture [75, 76] is a well-known example of this larger class of multiple scattering sequences. The sequence possesses a classical analog in terms of the Fermi cosmic-ray acceleration model [77] of a ball bouncing back and forth between a moving and a stationary wall. The fact that this sequence generates particles of very high energy has been used recently to estimate the unusually high fusion rates in cluster impact fusion at solid surfaces [78].

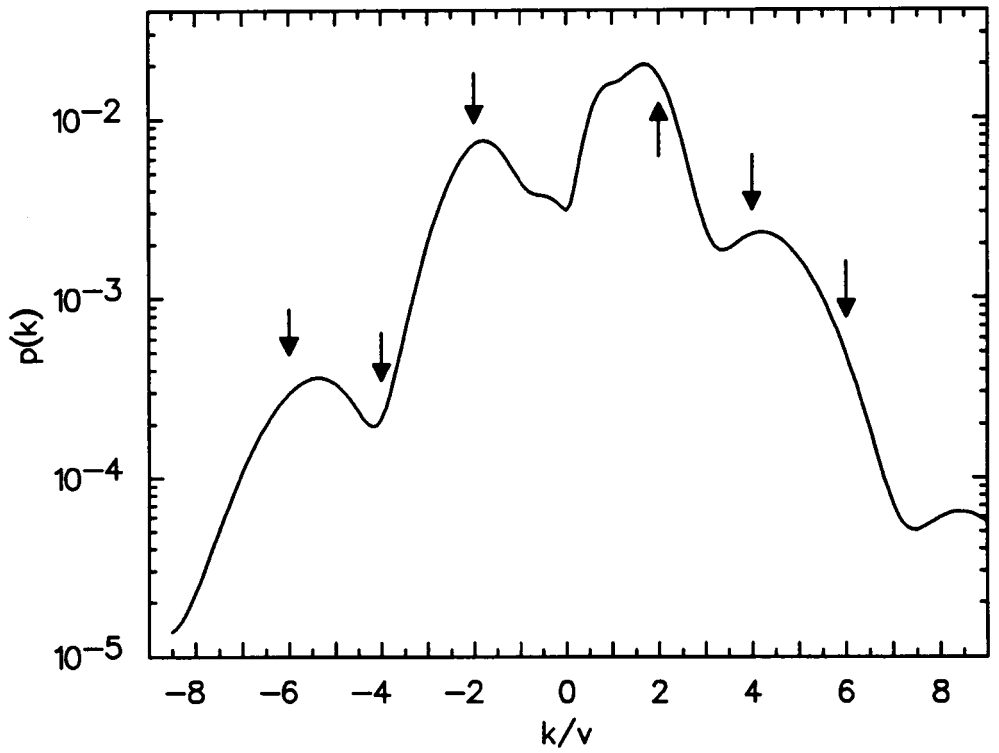

Figure 4.14: The multiple scattering peaks in the ionization spectrum of the 3D δ-model. The parameters chosen are $Z_P = Z_T = 10, v = 2$. The arrows mark the expected positions of the scattering peaks.

Chapter 5

Projectile Ionization in the Target Mean Field

5.1 Overview

In the previous chapter target ionization has been discussed in detail within the exactly solvable δ-model. It had been assumed that only one electron is present interacting with the bare projectile and the target centers. In the next two chapters we will discuss projectile ionization in three dimensions involving Coulomb interactions. Projectile ionization is, in its minimal form, an inelastic four-body problem (or can be reduced to one) because the target (the ionizing particle) is usually a structured atom (Eq. (1.2)). In this case both target and projectile ionization contribute to the total electron spectrum. Furthermore either of the colliding partners can be ionized with the other either staying in the ground state or being excited to a discrete or continuum state. In contrast to target ionization of the δ-model discussed in the preceding chapters, we can no longer solve this problem exactly. Rather, approximate methods must be employed. From now on, delineations of these methods and their applications will be our focus.

The pioneering experimental studies were carried out by Burch *et al.* [21] for heavy ion-atom collisions and by Wilson *et al.* [22] for molecular-ion - molecule collisions. A broad peak was discovered which was attributed to electrons ionized from the incident ion, frequently referred to as the electron loss peak (ELP). It should be noted, however, that the dominant ionizing

mechanisms that lead to the formation of the ELP are very different at either small or large angles. At forward angles the peak originates in a soft collision with the target and takes the form of a cusp at very small angles, the electron loss to the continuum ELC peak. On the other hand, the backward ELP is known to result from a head-on binary collision between a projectile electron and the target core. We note that the backward ELP is reminiscent of the backward binary peak discussed in Chapter 4 for target ionization. The difference is that the former results from a direct collision with the target, whereas the latter is due to electron capture by the (initially bare) projectile ion followed by a hard collision with the target nucleus.

The first theoretical treatment of projectile and target ionization in atom-atom collision was given by Bates and Griffing [37] using the first Born approximation. Burch *et al.* [21] proposed a simple model for the ELP peak which assumed that projectile electrons scatter elastically at the target. The final distribution of electrons lost from the projectile is obtained by convoluting the elastic scattering cross section with the Compton profile (i.e., its momentum distribution) of the initial state of the projectile electron. This model was subsequently modified [79] by using more realistic optical-model elastic scattering cross sections and is often called the elastic scattering model (ESM). Within a first Born approximation similarities between the ELP and target ionization have been shown to be related by a Galilei transformation from the projectile rest frame to the laboratory frame [28]. However, the first Born approximation is insufficient for heavy targets [80] due to the strength of the perturbation. In this case a higher-order theory is necessary [33, 36].

Recent studies of projectile electron loss [25, 36] have revealed large discrepancies between theory and experiment at backward angles ($\geq 90^0$) in fast collisions (0.5 MeV/u, or $v \sim 5$). However, as Fig. 4.13 shows, a simple first Born approximation reproduces the exact target ionization spectrum of the δ-model near the binary peak very well, in spite of the fact that the validity of the Born approximation is only marginally satisfied at $Z_P/v = 0.5$. Since the ELP at backward angles is composed of binary electrons, this discrepancy clearly contradicts the well-accepted notion that mechanisms for the generation of binary electrons are well understood. Apparently there seem to be some important physical processes present in projectile ionization that are not yet understood in terms of target ionization by structureless projectile impact. We therefore focus our effort on electron loss at large ejection angles. Bates and Griffing [37] first pointed out that two independent chan-

nels contribute to projectile ionization in atom-atom collisions: the projectile electron can be knocked out by the screened target nucleus or by a target electron. The former is usually referred to as the singly inelastic (SI) channel since the target can (but not always does) remain in its ground state. Similarly, the latter is referred to as the doubly inelastic (DI) channel since the target is, at the same time, excited or ionized. A more precise definition of these channels will be given in the next section. In this chapter we will discuss the treatment of the SI channel. In the next section we shall identify the DI channel and treat it in the next chapter.

5.2 Mean Field and Correlation

We consider a hydrogen-like projectile of nuclear charge Z_P, mass M_P and speed v incident on a target atom of nuclear charge Z_T and mass M_T. The geometry of the collision system is depicted in Fig. 5.1. We choose the

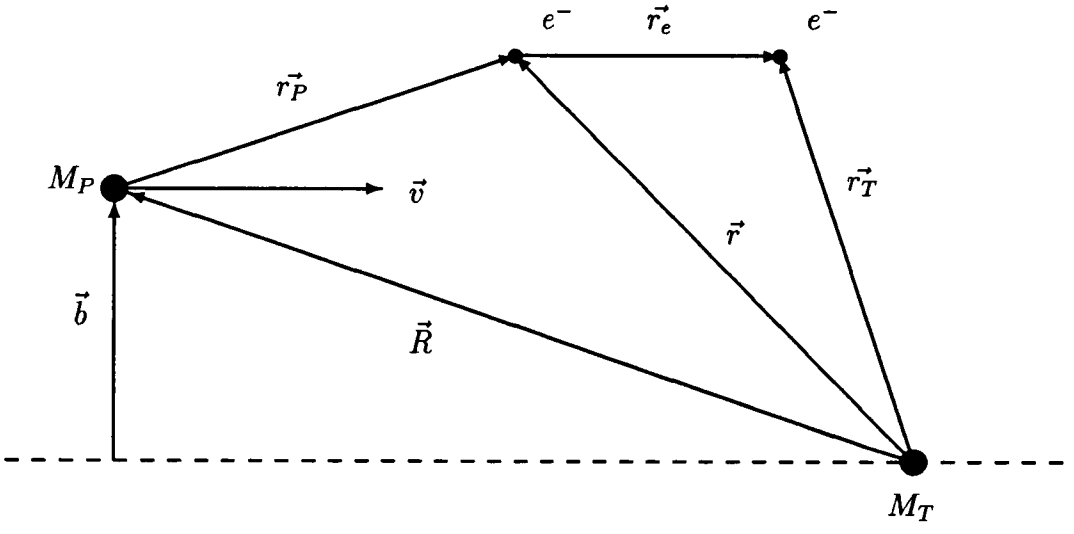

Figure 5.1: Geometry of the collision system for projectile ionization.

semiclassical approximation analogous to the one used in the δ-model. We use a reference frame with the target nucleus at rest. The internuclear motion in this frame is approximated by a straight-line trajectory with $\vec{R} = \vec{b} + \vec{v}t$ where $\vec{b}$ denotes the impact parameter (since we now are in 3D, $\vec{b}$ is not zero).

The coordinates of the projectile electron with respect to the target nucleus and the projectile nucleus are respectively given by $\vec{r}$ and $\vec{r_P} = \vec{r} - \vec{R}$. The coordinates of the target electron with respect to the target nucleus and the projectile electron are denoted by $\vec{r_T}$ and $\vec{r_e}$, respectively.

In most cases, with the exception of hydrogen targets, the target consists of many electrons. Fig. 5.1 represents then only the "active" participants in the collision while other electrons are treated as spectators which contribute to the effective screening of the target potential. The Hamiltonian for the electronic degrees of freedom is given by

$$H = H_0(P) + H_0(T) + V_P + V_T \tag{5.1}$$

with

$$H_0(P) = -\frac{1}{2}\nabla_r^2 - Z_P/r_P \tag{5.2}$$

the unperturbed Hamiltonian describing the initial bound state of the projectile electron,

$$H_0(T) = -\frac{1}{2}\nabla_{r_T}^2 + V_C(r_T) \tag{5.3}$$

the unperturbed Hamiltonian describing the initial bound state of the "active" target electron where V_C represents the effective one-body potential of the target core,

$$V_P(\vec{r}) = V_C(r) + 1/r_e \tag{5.4}$$

is the perturbation seen by the projectile electron during the collision, and

$$V_T(\vec{r_T}) = -Z_P/|\vec{R} - \vec{r_T}| \tag{5.5}$$

is the perturbation seen by the target electron, generated by the projectile nucleus. Since we study the projectile ionization and in order to avoid double counting we have included the electron-electron interaction $1/r_e$ ("correlation interaction") in (5.4) rather than in (5.5). Since the heavy particle motion in the straight-line impact parameter method is treated as being decoupled from the electronic degrees of freedom, the internuclear potential is neglected from the outset as it gives only rise to an overall phase factor upon a gauge transformation [3]. The small and large r limits of $V_C(r)$ are given by

$$V_C(r) \xrightarrow{r\to 0} -Z_T/r \tag{5.6}$$

$$V_C(r) \xrightarrow{r\to\infty} -1/r \tag{5.7}$$

such that $V_P(r)$ (Eq. (5.4)) represents the interaction with a neutral atom at large distances.

The solution to the Schrödinger equation with the Hamilton operator (Eq. (5.1)) is subject to the initial condition

$$\psi_i(t \to -\infty) = \phi_i^P(\vec{r}, t)\phi_i^T(\vec{r_T}, t) \tag{5.8}$$

where $\phi_i^{P,T}$ are the initial states (ground states) of the two electrons bound to the projectile and the target respectively. In Eq. (5.8) and in the following the usual translation factors (similar to that in Eq. (3.9)) are understood to be included. Projectile ionization, to be investigated in the following, requires the projection of the evolved state onto the subspace of final states

$$\psi_i(t \to \infty) = \phi_{\vec{k_f}}^P(\vec{r}, t)\phi_f^T(\vec{r_T}, t) \tag{5.9}$$

where $\phi_{\vec{k_f}}^P$ describes the emitted projectile electron with wave vector $\vec{k_f}$ and ϕ_f^T is the final state of the target electron. Unless the experiment resolves the final state of the target, the electron loss cross section contains the summation over the target final states. We group the final states into two channels: the singly inelastic (SI) channel consists of processes in which the projectile electron gets lost while the target electron remains in its ground state, i.e. $\phi_f^T = \phi_i^T$. In this case the effective perturbation (Eq. (5.4)) becomes

$$V_{eff}(r) = V_C(r) + \langle \phi_i^T | 1/r_e | \phi_i^T \rangle. \tag{5.10}$$

This is the effective potential experienced by the projectile electron in the mean field of the target. The target electrons play only the role of screening.

The second channel, the doubly inelastic (DI) processes leads to target excitation or ionization as well. It is important to distinguish between different pathways leading to DI processes. They can be illustrated most conveniently by using a Born series expansion for the transition (T) operator. With the help of Eqs. (5.4) and (5.5), we have

$$T = (V_C + 1/r_e + V_T) + (V_C + 1/r_e + V_T)G_0^+(V_C + 1/r_e + V_T) + ... \tag{5.11}$$

where $G_0^+ = [E - H_0(P) - H_0(T) + i\eta]^{-1}$ is the Green's operator describing the unperturbed propagation of the projectile and the target electrons. To first order, only the correlation operator $1/r_e$ can mediate DI process, in the

following referred to as correlated DI. To second (and higher) order, however, another pathway to simultaneous excitation of both collision partners becomes accessible: terms of the form $V_T G_0^+ V_C$ or $V_C G_0^+ V_T$ induce simultaneous but independent target and projectile ionization without involving the electron-electron interaction. Since the latter is obviously present within the independent particle model we refer to this process as the uncorrelated DI. In principle the two pathways are indistinguishable and should be added coherently, provided they would result in the same final state. However, since the two pathways give rise to very different energy, momentum and angular momentum distributions of the continuum electrons, they can be, for all practical purposes, treated as distinguishable. Thus, the two pathways can be added incoherently.

It is, furthermore, important to note that the uncorrelated DI process is, within the independent particle model, included in the calculation of the SI channel if we treat the latter as a one-electron problem. Denoting the probability for projectile ionization by $P_p(I)$ and the probability for occupation of the final target state f by $P_T(f)$ we have

$$P_p(I) = P_p(I)P_T(i) + P_p(I)\sum_{f\neq i} P_T(f) \tag{5.12}$$

where we denote the initial target state by i. Treating the electron loss problem as an effective one-electron problem (i.e. without taking into account the target electronic degrees of freedom) amounts therefore to summation over a complete set of final states of the second (target) electron. In the calculation of $P_p(I)$ the charge distribution of the target in its ground state is used. While this may be a crude approximation for a process involving also simultaneous target ionization with large energies of the ejected electron, Eq. (5.12) nevertheless shows that the uncorrelated DI processes, apart from the inaccuracy of the mean field potential (Eq. (5.10)), are implicitly included in the SI channel within the independent particle model.

The determination of $P_p(I)$ amounts to the calculation of projectile ionization by the effective potential (5.10). We refer to $P_p(I)$ thus obtained within the independent particle model as mean field projectile ionization, or simply mean field ionization. We shall use the terms SI channel and mean field ionization interchangeably. In the remainder of this chapter we devote our discussion to treating mean field ionization in order to determine to what extent projectile ionization can be described by mean field ionization alone.

Correlated DI processes due to electron-electron scattering, on the other hand, amount to a breakdown of the independent particle model and require explicit treatment. In Chapter 6 we will study for the first time correlated DI processes by a second order Born approximation. We shall refer to correlated DI processes as correlated ionization. This terminology is consistent with the more general definition of correlation in atomic physics: Correlation is the deviation from the independent particle approximation [81]. Correlated ionization is very difficult to treat since it is an intrinsic four-body process. We resort to a perturbation expansion of the transition operator T (Eq. (5.11)) and retain up to second order in correlation

$$T_{corr} = 1/r_e + 1/r_e G_0^+ V_C + V_C G_0^+ 1/r_e + 1/r_e G_0^+ 1/r_e. \tag{5.13}$$

The treatment of (5.13) will be the subject in the next chapter.

5.3 Approximation Methods for Mean Field Ionization

We outline in this section approximation methods for the treatment of mean field ionization. The ionization of the projectile is considered to be caused by the interaction of the projectile electron with a screened target. We shall therefore refer to the interaction as the perturbation, even though by no means the interaction is small in all cases. We shall discuss the impulse approximation [82] which is valid for strong perturbations encountered in asymmetric collisions with heavy targets $Z_P \ll Z_T$, and a continuum distorted wave method [83, 84] which is appropriate for comparable near-symmetric collisions $Z_P \sim Z_T$. The former method is often called a "one-center" approximation while the latter a "two-center" approximation for reasons which will become apparent later in the section. We will also briefly discuss a classical trajectory Monte Carlo method [85, 86].

5.3.1 Impulse Approximation

The basic quantity of interest is the transition amplitude which, in its exact form, can be rewritten from (3.45) for a given impact parameter $\vec{b}$ as

[87]

$$a_{fi}(b) = -i \int_{-\infty}^{\infty} dt \langle \phi_f(t) | V_{eff} | \psi_i^+(t) \rangle \tag{5.14}$$

where $\phi_f(t)$ is the final state of the ejected electron and $\psi_i^+(t)$ is the exact scattering wave function propagated from the initial state $\phi_i(t)$ with outgoing boundary conditions, V_{eff} is the interaction of the projectile electron with the target. We replace the exact wave function $\psi_i^+(t)$ by its impulse approximation (IA) [3],

$$\psi_i^+(t) = \int d\vec{q} \tilde{\phi}_i(\vec{q}, t) \psi_{\vec{q}}^+ \tag{5.15}$$

where $\tilde{\phi}_i(\vec{q}, t) = \langle \vec{q} | \phi_i(t) \rangle$ is the momentum space representation of the initial state and $\psi_{\vec{q}}^+$ represents the scattered electron wave of initial momentum $\vec{q}$

$$\left(-\frac{1}{2} \nabla^2 + V_{eff} \right) \psi_{\vec{q}}^+ = \frac{1}{2} q^2 \psi_{\vec{q}}^+ \tag{5.16}$$

satisfying outgoing boundary conditions. $\psi_{\vec{q}}^+$ describes the exact propagation in the target potential V_{eff} while the interaction with the projectile enters Eq. (5.15) only through its initial momentum distribution known as the Compton profile. The assumption leading to Eq. (5.15) implies that the projectile electron is scattered in the strong field of the target, V_{eff}, while the interaction with projectile during the scattering is neglected. In other words, the projectile electron is assumed to be ejected impulsively such that the projectile nucleus does not participate actively in the ionization process. This approximation therefore expected to be valid for $Z_P/v \ll 1$. Furthermore it has been suggested [88] that $Z_P/v \ll 1$ is a sufficient but not necessary condition and that IA should be valid for any impact speeds provided the target dominates in the "interaction region". This implies that the IA should be more accurate for heavy targets than for light targets at a given Z_P/v.

Substituting (5.15) into (5.14) and inserting a complete set of plane waves yields

$$a_{fi}^{IA}(b) = -i \int dt d\vec{p} d\vec{q} \tilde{\phi}_f^*(\vec{p}, t) \langle \vec{p} | V_{eff} | \psi_{\vec{q}}^+ \rangle \tilde{\phi}_i(\vec{q}, t) \tag{5.17}$$

where the integration limits are understood to extend over $\pm\infty$. In (5) the two-body T matrix element can be identified as

$$T_{fi}(\vec{p}, \vec{q}) = \langle \vec{p} | V_{eff} | \psi_{\vec{q}}^+ \rangle \tag{5.18}$$

which is the transition amplitude of a free electron with incident momentum $\vec{q}$ to a final momentum $\vec{p}$. In general $|\vec{q}| \neq |\vec{p}|$. Since $q^2/2$ and $p^2/2$ represent the kinetic energies, (5.18) is said to be off-energy-shell and is not directly related to any physical observable.

The solution to Eq. (5.16) can be cast into an integral representation incorporating the outgoing boundary conditions

$$|\psi_{\vec{q}}^{+}\rangle = |\vec{q}\rangle + g_0^{+} V_{eff} |\psi_{\vec{q}}^{+}\rangle \tag{5.19}$$

where g_0^{+} is the one-electron free particle Green's operator

$$g_0^{+} = (E + \nabla_r^2/2 + i\eta)^{-1} \tag{5.20}$$

in which the interaction with the projectile nucleus, $-Z_P/r_P$, is neglected. Iterations of Eq. (5.19) result in an explicit expression for $\psi_{\vec{q}}^{+}$,

$$|\psi_{\vec{q}}^{+}\rangle = \left[\sum_{n=0}^{\infty} (g_0^{+} V_{eff})^n\right] |\vec{q}\rangle. \tag{5.21}$$

In terms of the Born series (Eq. (5.11)), substitution of (5.21) into (5.18) implies the summation over terms to all order in V_{eff},

$$T = V_{eff} \sum_{n=0}^{\infty} (g_0^{+} V_{eff})^n. \tag{5.22}$$

After integration over time in (5) which gives rise to a delta function, we arrive at the exact transition amplitude in the IA,

$$\begin{aligned} a_{fi}^{IA}(b) &= -2\pi i \exp(i\vec{k_f} \cdot \vec{b}) \int d\vec{q} d\vec{p}\, \delta(\vec{q} \cdot \vec{v} - (k_f^2 + v^2 - 2\varepsilon_i)/2) \exp(-i\vec{q} \cdot \vec{b}) \\ &\quad \times T_{fi}(\vec{p} + \vec{v}, \vec{p} + \vec{v} + \vec{q} - \vec{k_f}) \tilde{\varphi}_f^{-*}(\vec{p}) \tilde{\varphi}_i(\vec{p} + \vec{q} - \vec{k_f}) \end{aligned} \tag{5.23}$$

with $\vec{k_f}$ being the ejected electron momentum in the laboratory frame and $\tilde{\varphi}_f^{-}(\vec{p})$ is the momentum space representation of the final continuum state given by an incoming Coulomb wave in the projectile rest frame with energy $\varepsilon_f = \frac{1}{2}(\vec{k_f} - \vec{v})^2$. Eq. (5.23) can be simplified by taking advantage of the fact that $\tilde{\varphi}_f^{-}(\vec{p})$ is strongly peaked at $\vec{p} = \vec{k_f} - \vec{v}$ [89]. Applying a peaking approximation to (5.23) produces (see Appendix C)

$$a_{fi}^{IA}(b) = -\frac{2\pi i}{v} \exp(i\vec{k_f} \cdot \vec{b}) \int d\vec{q_\perp} \exp(-i\vec{q} \cdot \vec{b}) T_{fi}(\vec{k_f}, \vec{q}) S_{fi}^{P}(\vec{q} - \vec{v}) \tag{5.24}$$

with $\vec{q} = \vec{q_\perp} + q_z^0 \hat{v}$ and

$$q_z^0 = (k_f^2 + v^2 - 2\varepsilon_i)/2v. \tag{5.25}$$

$S_{fi}^P(\vec{q} - \vec{v})$ is the so-called inelastic form factor

$$S_{fi}^P(\vec{p}) = \langle \varphi_f^- | \exp(-i\vec{p} \cdot \vec{r_P}) | \varphi_i \rangle. \tag{5.26}$$

Substituting (5.26) in (5.24) we find the doubly differential cross section (DDCS) as a function of the energy and angle of ejected electrons

$$\frac{d^2\sigma^{IA}}{dEd\Omega} = \frac{16\pi^4}{v} k_f \int d\vec{q}\, \delta(\vec{q}\cdot\vec{v} - (k_f^2 + v^2 - 2\varepsilon_i)/2) \left| T_{fi}(\vec{k_f}, \vec{q}) S_{fi}^P(\vec{q} - \vec{v}) \right|^2. \tag{5.27}$$

This is the final expression for the exact impulse approximation containing the exact off-shell two-body T matrix element (Eq. (5.18)). We will use the exact IA in the next chapter in order to compare with the correlated ionization.

For electron emission into backward angles $\theta \geq 90^0$ where $\vec{k}_f - \vec{v}$ is large the Coulomb wave $\tilde{\varphi}_f^{-*}$ can be replaced by a plane wave. Replacement of the Coulomb wave by a plane wave in (5.26) reduces the form factor $S_{fi}^P(\vec{q} - \vec{v})$ to the simple Compton profile $\tilde{\varphi}_i(\vec{q} - \vec{v})$. Our numerical checks confirm the validity of this replacement near the ELP as has been suggested in literature [28]. The DDCS of the exact impulse approximation (in the sense of the exact off-shell T matrix $T_{fi}(\vec{k_f}, \vec{q})$) with plane-wave final states reduces to

$$\frac{d^2\sigma^{PWIA}}{dEd\Omega} = \frac{16\pi^4}{v} k_f \int d\vec{q}\, \delta(\vec{q}\cdot\vec{v} - (k_f^2 + v^2 - 2\varepsilon_i)/2) \left| T_{fi}(\vec{k_f}, \vec{q}) \tilde{\varphi}_i(\vec{q} - \vec{v}) \right|^2. \tag{5.28}$$

This formula will be used in the remainder of this chapter to calculate DDCS for the mean field ionization.

5.3.2 On-Shell Approximations

For hydrogenlike projectiles the Compton profile $\tilde{\varphi}_i(\vec{q} - \vec{v})$ has a simple analytical expression. Thus, the evaluation of cross sections in the plane wave IA (5.28) amounts to the determination of the exact off-shell T matrix (5.18). This requires the knowledge of the scattering states $\psi_{\vec{q}}^+$ given by (5.16). $\psi_{\vec{q}}^+$ can be most conveniently obtained numerically by the standard partial wave

analysis [90] in the spherically symmetric potential V_{eff}. Therefore, $T_{fi}(\vec{k_f}, \vec{q})$ can be determined by an additional numerical integration upon substituting $\psi_{\vec{q}}^{+}$ thus obtained into Eq. (5.18). In practice this process is time consuming because for each DDCS we must evaluate $T_{fi}(\vec{k_f}, \vec{q})$ many times since the T matrix is inside a two-dimensional integral (Eq. (5.28)).

Various approximation methods have been devised to solve the problem. Frequently used approximations to (5.28) can be derived from (5.28) by invoking various forms of on-shell approximations. The underlying idea in each case is that the on-shell T matrix element, $|T_{fi}|^2$, becomes proportional to the elastic cross section for the scattering of an electron at the target core. Since the information necessary for the determination of elastic cross sections is fully contained in $\psi_{\vec{q}}^{+}$, no additional numerical integration is required to evaluate T_{fi}. The approach to the energy shell is not unique, and as will be shown below, it leads to discrepancies at backward angles.

Several choices for on-shell approximations (OSA) are frequently employed:

(a) One form of OSA to (5.28) proposed by Hartley and Walters [36] (HW) consists of keeping the exact momentum transfer $\vec{q} - \vec{k_f}$ and choosing an approximate energy according to $E = \max(k_f^2/2, q^2/2)$. This choice of E ensures that the largest possible momentum transfer for a given pair $(\vec{k_f}, \vec{q})$ is less than $2\sqrt{2E}$, a relation satisfied in elastic scattering with well defined energies. The T matrix element in (5.28) is therefore replaced by

$$16\pi^4 |T_{fi}(\vec{k_f}, \vec{q})|^2 \equiv \sigma_{el}(E, \cos(\theta_{eff})) \tag{5.29}$$

where the effective scattering angle for elastic scattering θ_{eff} is given by

$$\cos(\theta_{eff}) = 1 - |\vec{q} - \vec{k_f}|^2/4E. \tag{5.30}$$

It should be noted that the effective scattering angle resulting from the imposed constraints on E and on the momentum transfer is related to the true scattering angle $\theta = \cos^{-1}(\hat{q} \cdot \hat{k}_f)$ as follows,

$$\begin{aligned} \sin^2(\theta_{eff}/2) - \sin^2(\theta/2) &= (a^2 + b^2 - 2ab\cos\theta)/4a^2 - \sin^2(\theta/2) \\ &= -(a-b)(a+b-2a\cos\theta)/4a^2 \end{aligned} \tag{5.31}$$

where $a = \max(q, k_f)$ and $b = \min(q, k_f)$. For backward scattering angles $(\theta \geq \pi/2)$, $\sin^2(\theta_{eff}/2) - \sin^2(\theta/2)$ is always negative and since $\sin^2(\theta/2)$

is a monotonically increasing function for $0 \leq \theta \leq \pi$, the effective angle is smaller, i.e. $\theta_{eff} \leq \theta$. Finally, the DDCS in the HW approach is given by

$$\frac{d^2\sigma^{HW}}{dEd\Omega} = \frac{k_f}{v^2} \int d\vec{q_\perp} \sigma_{el}(E, \cos(\theta_{eff}))|\tilde{\varphi}_i(\vec{q} - \vec{v})|^2. \tag{5.32}$$

(b) An alternative OSA can be devised by noting that the momentum distribution (i.e., the Compton profile) is strongly peaked around $\vec{q} \approx \vec{v}$ or $\vec{q} - \vec{v} \approx 0$. Therefore the energy conserving δ function in (5.28) is modified such that

$$\delta(\vec{q} \cdot \vec{v} - vq_z^0) \approx \delta((q^2 + v^2)/2 - vq_z^0). \tag{5.33}$$

This leads to a constraint in the magnitude of q of the form

$$q_0^2/2 = k_f^2/2 - \epsilon_i. \tag{5.34}$$

Conservation of the exact momentum transfer $\vec{q} - \vec{k_f}$ requires the replacement of the off-shell T matrix in (5.28) by the elastic differential cross section

$$16\pi^4 \frac{q_0}{v} |T_{fi}(\vec{k_f}, \vec{q})|^2 \equiv \sigma_{el}(q_0^2/2, \cos(\theta_{eff})) \tag{5.35}$$

with

$$\cos(\theta_{eff}) = 1 - |\vec{q_0} - \vec{k_f}|^2/2q_0^2. \tag{5.36}$$

The effective scattering angle in this approximation is related to the true scattering angle θ through

$$\sin^2(\theta_{eff}/2) - \sin^2(\theta/2) = -(q_0 - k_f)(q_0 + k_f - 2q_0 \cos\theta)/2q_0^2. \tag{5.37}$$

As is the case in (a), the effective scattering angle is also smaller, i.e. $\theta_{eff} \leq \theta$. However, since $q_0 - k_f$ is small (Eq. (5.34)) θ_{eff} is closer to the true scattering angle than in a). The DDCS in this peaking approximation (PA) is now of the form

$$\frac{d^2\sigma^{PA}}{dEd\Omega} = k_f \int d\Omega_{q_0} \sigma_{el}(q_0^2/2, \cos(\theta_{eff}))|\tilde{\varphi}_i(\vec{q_0} - \vec{v})|^2. \tag{5.38}$$

The physical picture underlying (5.38) is that the doubly differential cross section is determined by a subset of the Compton profile lying on a surface of constant q_0 (Eq. (5.34)) which is scattered into the direction of $\vec{k_f}$. We point

out that the PA scheme represented by Eq. (5.38) is essentially equivalent to the ESM model proposed by Burch *et al.* [21]. The only difference appears to be that the initial binding energy of the projectile electron is explicitly taken into account in Eq. (5.38).

(c) In the binary encounter approximation (BEA) originally proposed by Bonsen and Vriens [91] the direction of the outgoing electron $\hat{k}_f$ rather than the momentum transfer is preserved. This implies the following replacement for the T matrix element in (5.28),

$$16\pi^4|T(\hat{k}_f q, \vec{q})|^2 \equiv \sigma_{el}(q^2/2, \cos\theta). \tag{5.39}$$

Unlike the two previous approximations the elastic cross section depends on the true scattering angle. The energy conserving δ function in (5.28) is now replaced by $\delta(q^2/2 - q'^2/2)$ where the energy $E = q'^2/2$ for elastic scattering is determined from the relation for an impulsive momentum transfer in the projectile field

$$(\vec{k_f} - \vec{v})^2/2 = (\vec{q'} - \vec{v})^2/2 - (\vec{q} - \vec{v})^2/2 + \epsilon_i. \tag{5.40}$$

The latter has an obvious physical interpretation: the kinetic energy of the scattered electron $(\vec{q'} - \vec{v})^2/2$, as seen in the projectile rest frame, must be equal to the asymptotic kinetic energy $(\vec{k_f} - \vec{v})^2/2$ after escaping from the projectile potential with a local value at the point of the collision, $V(r) = \varepsilon_i - (\vec{q} - \vec{v})^2/2$.

The corresponding BEA cross section is given by

$$\frac{d^2\sigma^{BEA}}{dEd\Omega} = \frac{k_f}{v}\int d\vec{q}\sigma_{el}(q^2/2, \cos\theta)|\tilde{\varphi}_i(\vec{q} - \vec{v})|^2\delta(q^2/2 - q'^2/2). \tag{5.41}$$

Defining $\vec{p} = \vec{q} - \vec{v}$ a simpler expression for the cross section can be obtained by integrating (5.41) over the angle $\cos\theta_p = \hat{p}\cdot\hat{v}$,

$$\frac{d^2\sigma^{BEA}}{dEd\Omega} = \frac{k_f}{v^2}\int_{p_{min}}^{p_{max}} dpp|\tilde{\varphi}_i(\vec{p})|^2\int_0^{2\pi} d\phi\sigma_{el}(q'^2/2, \cos\theta) \tag{5.42}$$

where ϕ is the azimuthal angle of $\vec{p}$ (or $\vec{q}$) and p_{min} and p_{max} are the minimum and maximum values for which Eq. (5.40) can be satisfied. It is important to note that $\sigma_{el}(q^2/2, \cos\theta)$ is not axially symmetric with respect to $\hat{v}$ and is therefore ϕ dependent.

5.3.3 Continuum Distorted Wave Method

As pointed out in the proceeding section, the IA is valid for asymmetric collisions $Z_P \ll Z_T$ (e.g. H^0 on Ar). For more symmetric collisions such as He^+ on He the validity of the IA becomes questionable. We have shown in Chapter 4 that three-body effects play an essential role in the electron emission spectrum of the δ-model. Analogous to the three-body effects in the δ-model we encounter here the so-called "two-center" effect which has been investigated in several recent studies dealing with target ionization [92, 93, 94, 95, 96]. This terminology arises from the fact that ionized electrons are moving in the combined field of both the target and the projectile. Since for symmetric collision systems the strengths of the two fields are comparable, the final state must take into account the interaction with both force centers in a symmetric form. The impulse approximation, on the other hand, is a "one-center" approximation since it assumes that the interaction of the electron with the weaker field (in this case the projectile) is negligible during the collision. We will analyze two-center effects for projectile ionization at large angles using the continuum distorted wave (CDW) model for the final state [83, 84] and the three-body classical trajectory Monte Carlo (CTMC) method [85, 86].

Within a first-order distorted wave approximation the ionization amplitude is given by

$$a_{fi} = -i \int dt \langle \eta_f^- | W_i | \zeta_i^+ \rangle \tag{5.43}$$

$$= -i \int dt \langle \eta_f^- | W_f^\dagger | \zeta_i^+ \rangle \tag{5.44}$$

where $W_{i,f}$ are the prior (post) residual potentials not already incorporated into the distorted waves $|\zeta_i^+\rangle, |\eta_f^-\rangle$ which satisfy the Schrödinger equations

$$\left[-\nabla_r^2/2 - Z_P/r + U_i\right] \zeta_i^+ = i\frac{\partial \zeta_i^+}{\partial t} \tag{5.45}$$

$$\left[-\nabla_r^2/2 - Z_P/r + U_f\right] \eta_f^- = i\frac{\partial \eta_f^-}{\partial t}. \tag{5.46}$$

Accordingly,

$$W_i = V_{eff} - U_i \tag{5.47}$$

$$W_f = V_{eff} - U_f. \tag{5.48}$$

We apply in the following the continuum distorted wave (CDW) model [85, 93], which has been previously studied extensively for target ionization by charged projectile impact, to projectile electron scattering at the neutral target. In the application of distorted-wave theory to atomic collisions it is convenient to reverse the usual strategy in finding approximate solutions: rather than choosing the distortion potential first and determining the distorted wave from the potential, we choose first a distorted wave that contains the presumably relevant physics and subsequently determine the distortion potential. Thus, the distortion potentials $W_{i,f}$ are implicitly determined by our choice of the distorted waves. The initial state is chosen to be identical to the unperturbed initial state

$$\zeta_i^+ = \phi_i^P(\vec{r}, t) \tag{5.49}$$

and

$$W_i = V_{eff}, \tag{5.50}$$

i.e. in the present case the CDW model reduces to a CDW approximation for the final state, namely, a product of a Coulomb wave in the projectile field and a scattering state in the effective potential V_{eff},

$$\eta_f^- = (2\pi)^{3/2} \exp(-i\epsilon_f t) \exp(-i\vec{k}_f^P \cdot \vec{r_P}) \psi_P^-(\vec{k}_f^P, \vec{r_P}) \psi_T^-(\vec{k_f}, \vec{r}) \tag{5.51}$$

where $\vec{k_f}$ and $\vec{k}_f^P$ denote the final momentum of the ejected electron with respect to the target and the projectile nuclei, respectively, and $\epsilon_f = k_f^2/2$. The continuum states in the projectile field and in the target field satisfying the incoming boundary conditions are denoted by ψ_P^- and ψ_T^-, respectively, which are δ-normalized in momentum space. This product guarantees the correct asymptotic behavior of the wavefuntion in the limit $t \to +\infty$. That is, it behaves as (i) a continuum state of the projectile for small values of r_P and (ii) a continuum state of the target distorted by a phase due to the Coulomb field of the projectile for small values of r. Choosing the prior form (Eq. (5.43)), the following final expression is obtained for the doubly differential cross section (DDCS) as a function of the energy and the angle of the electron in the laboratory frame,

$$\frac{d^2\sigma^{CDW}}{dEd\Omega} = \frac{k_f}{4\pi^2 v^2} \int d\vec{p_\perp} |S_{fi}^P(-\vec{p}) T_T|^2 \tag{5.52}$$

with

$$T_T = \int d\vec{r} \exp(-i\vec{p}\cdot\vec{r}) V_{eff}(r) \psi_T^{-*}(\vec{k_f}, \vec{r}) \exp(i\vec{k_f}\cdot\vec{r}) \qquad (5.53)$$

where $\vec{p}$ is the momentum transfer with a $\hat{z}$ component $p_z = -((\vec{k_f} - \vec{v})^2 - 2\varepsilon_i)/2v$. While the projectile form factor S_{fi}^P, given by Eq. (5.26), can be evaluated explicitly, the most difficult part of the calculation is the evaluation of T_T which contains the continuum wavefuntion of the target $\psi_T^{-*}(\vec{k_f}, \vec{r})$. This wave function and the integral are evaluated numerically using a partial wave expansion similar to the evaluation of T_{fi} in the IA.

As a side remark we note that the target continuum wave function could, in principle, be calculated including exchange corrections with electrons in the target core. For small values of k_f where exchange is expected to be most important an estimate can be derived from a recent calculation [97]. To this end, we note that for small values of k_f a good approximation to the cross section is obtained by factorizing $\psi_T^{-*}(\vec{k_f}, \vec{r})$ out of T_T. The resulting cross section can be written as a first Born (B1) cross section times a "normalization" factor of the target continuum,

$$\frac{d^2\sigma^{CDW}}{dEd\Omega} = |N_0|^2 \frac{d^2\sigma^{B1}}{dEd\Omega} \qquad (5.54)$$

$$N_0 = (2\pi)^{3/2} \psi_T^{-*}(\vec{k_f}, \vec{r} = 0) \qquad (5.55)$$

where the normalization N_0 gives rise to the well-known electron capture to the continuum peak. In the present case, N_0 is the normalization factor for a short ranged potential and represents capture to the neutral target.

5.3.4 The CTMC Method

Both the IA and the CDW approximation methods treat the collision dynamics quantum mechanically. The classical trajectory Monte Carlo method (CTMC) [85], on the other hand, determines the evolution of the collision system classically. It is exact in the sense that all interactions are treated to all orders in the collision. The CTMC approach consists of: (i) Choosing randomly the impact parameters b and the initial conditions of the classically described electron according to the classical phase space distribution approximating the quantum mechanical wave function. (ii) Numerical integration of classical equations of motion during the collision, at the end of which

it is determined what reaction, if any, has occurred, as well as the energy and the scattering angle of each particle. Details of our CTMC calculations performed in collaboration with Dr. Reinhold are given in Ref. [98].

5.4 Elastic Scattering

Since both the exact two-body T matrix element as well as its on-shell approximations determine the behavior of the electron loss cross section we shall investigate the elastic electron scattering in the effective target potential in detail. First of all we must choose an effective potential V_{eff} (Eq. (5.10)). In our calculation we have used a parameterized model potential [99] of the form

$$V_{eff}(r) = -\frac{Z}{r}\left[1 + a(\exp(br) - 1)/b\right]^{-1} \tag{5.56}$$

for the static potential of the Ar target shown in Fig. 5.2. The constants Z (the target nuclear charge), a, and b in (5.56) for a number of atoms can be found in Ref. [99]. For comparison the electrostatic potential calculated with the Hartree-Fock method is also displayed. It can be seen that for $r \leq 1$ they are virtually identical. Since at backward angles the small r region is most important the analytic model potential is therefore appropriate for our purposes.

The calculation of the exact scattered wave in V_{eff} (Eq. (5.16)) proceeds most easily with the help of a partial wave expansion. The resulting elastic scattering cross section for electrons on argon can be tested by comparison with experimental data. In Fig. 5.3 we display the elastic cross section for electrons on Ar with a typical energy of 200 eV. The calculation with the effective potential is seen to agree within 20% with experimental values. It indicates that exchange effects, which result from scattering of two identical particles (the projectile electron and the target electron) and are important at low collision speeds, are small in 0.5 MeV/u energy range [101, 102].

One characteristic feature of the scattering cross section is a rise at large angles ($\theta \geq 130^0$). Since this structure will eventually survive the convolution with the Compton profile (Eq. (5.28)) it is important to understand its origin. Fig. 5.4 displays the decomposition of the total elastic cross section into

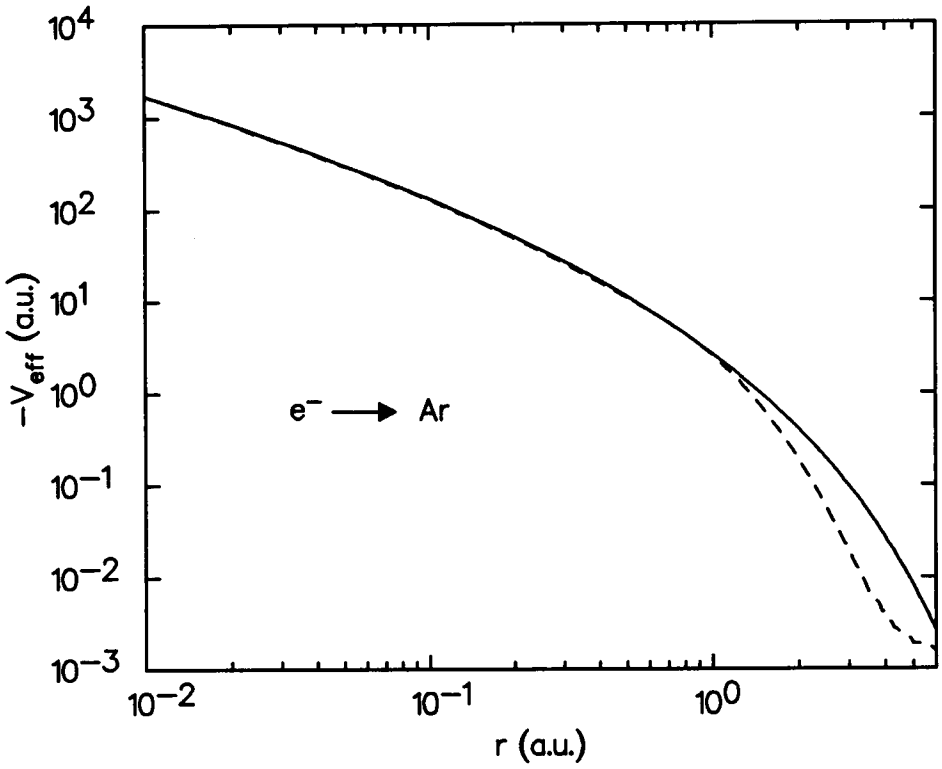

Figure 5.2: The negative of the effective potential of an electron in the field of Ar atom. Solid line (——), the model potential used for V_{eff} Ref. [99]; dashed line (- - -), Hartree-Fock electrostatic potential.

partial-wave components given by

$$\sigma_t = \sum_{l=0}^{\infty} \sigma_l = \frac{4\pi}{k^2} \sum_{l=0}^{\infty} (2l+1) \sin^2 \delta_l \tag{5.57}$$

where k is the electron momentum and δ_l is the phase shift for angular momentum l. The rapid decrease with l is characteristic for heavy neutral targets. For small l (or small impact parameter b) the electron sees a strong, only slightly screened, Coulomb potential. For moderately high l, however, the electron sees an essentially neutral target with which the interaction is, apart from polarization forces, negligible. The fact that only a few partial waves effectively contribute results in the oscillatory structures in the elastic differential cross section. In fact, in a simplified model with partial wave

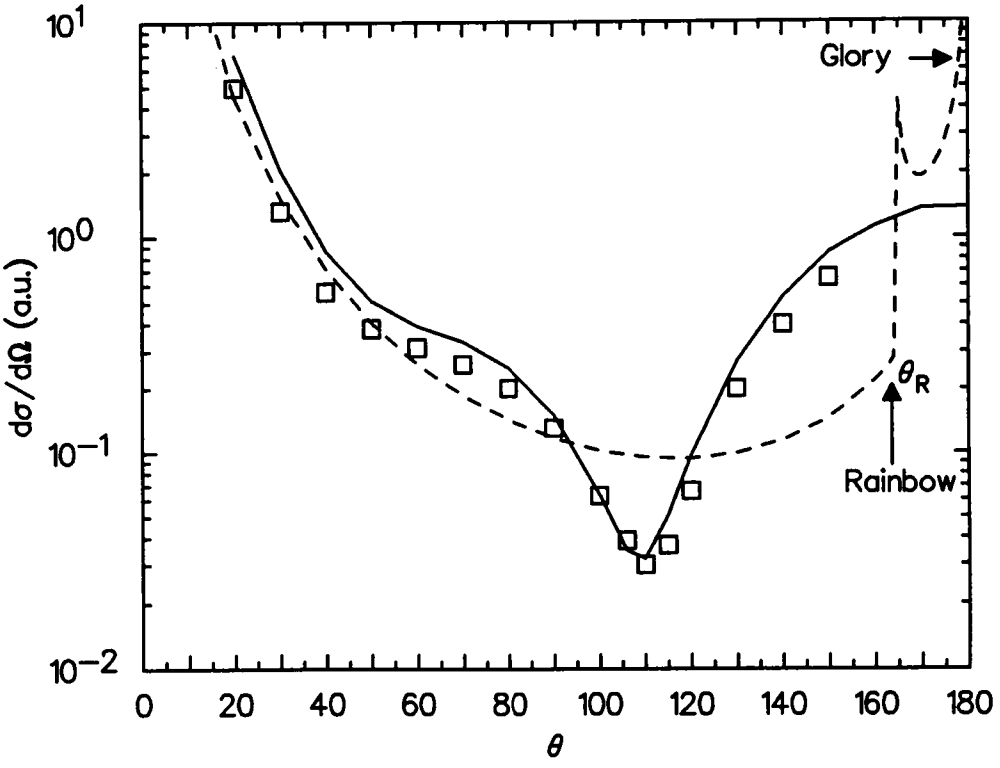

Figure 5.3: Quantum and classical cross section for elastic scattering of 200 eV electrons at Ar. ——, Quantum mechanical result; - - -, Classical result; □, expt. data of Ref. [100]. The classical curve shows a rainbow near $\theta_R \sim 160^0$ and a glory near 180^0 (see text (Eq. (5.58)) for definitions of rainbow and glory).

contributions only from $l = 0$ and $l = 2$ the angular distribution reflects the nodal structure of the Legendre polynomial P_2 with minima at $\theta \approx 54^0$ and 126^0 and maxima at 0^0 , 90^0 , and 180^0 . The latter accounts qualitatively for the structures seen in Fig. 5.3.

These structures are to be distinguished from classical rainbow and glory singularities present in the classical cross section also shown in Fig. 5.3. Its origin is traced to the classical deflection function shown in Fig. 5.5. Recalling that the classical cross section is given by

$$\frac{d\sigma}{d\Omega} = \frac{1}{\sin\theta} \sum_i b_i \left| \frac{db_i}{d\Theta} \right| \tag{5.58}$$

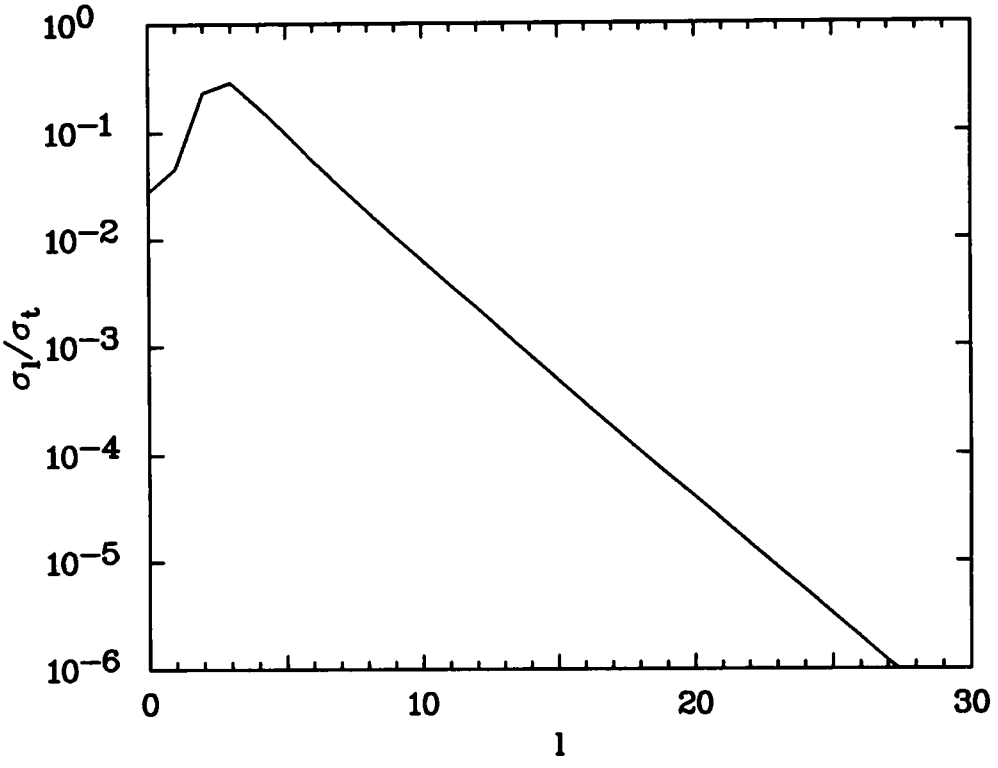

Figure 5.4: Partial wave decomposition of elastic cross section for 200 eV electrons on Ar. Each partial wave contribution σ_l (Eq. (5.57)) is normalized to the total cross section σ_t.

where i runs through all impact parameters contributing at a given observation angle θ, it is seen that a singularity can occur if either $d\Theta/db$ or $\sin\theta$ is zero. The former gives rise to a rainbow while the latter to a glory. In the neighborhood of the rainbow or the glory there are three impact parameters leading to the same θ (see Fig. 5.5). Since $\theta(b \to \infty) = 0$ and $\theta(b \to 0) = -\pi$ the occurrence of a rainbow for fast electron-atom collisions requires the decrease of the deflection function to below $-\pi$ at finite impact parameters. The prerequisite for the latter is a locally strong attractive potential as can be found near the nucleus of a heavy target. Thus, the strong variation of the target potential is the origin of both the interference of a limited number of partial waves in the quantum calculation and of the rainbow in the classical scattering process. However, the rise of the cross section is not a classical

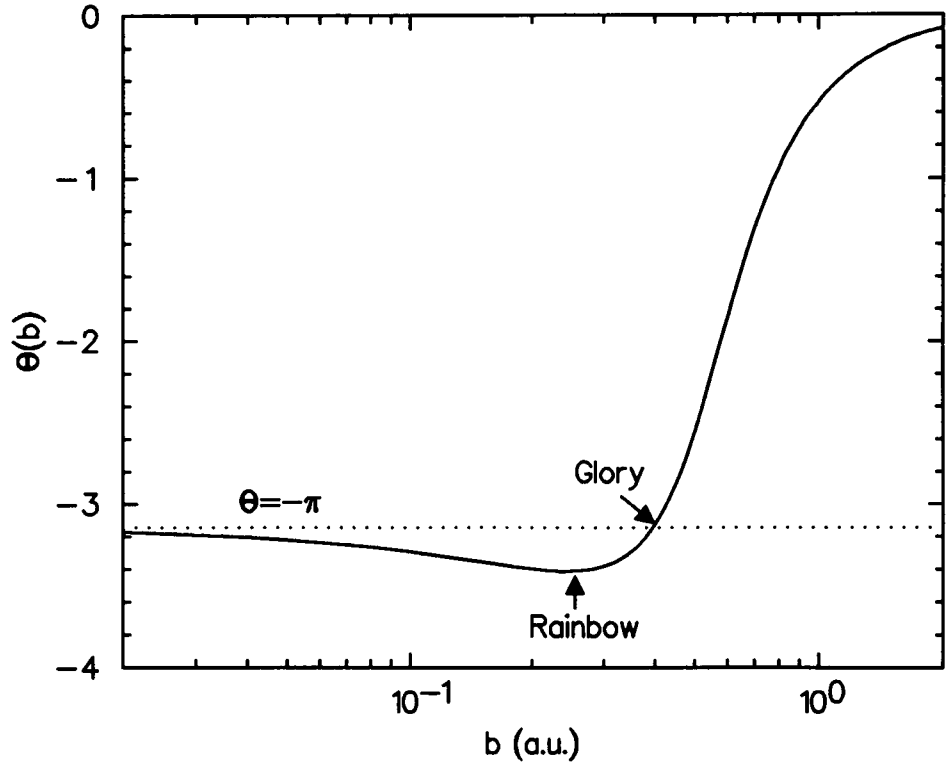

Figure 5.5: Classical deflection function for elastic scattering of 200 eV electrons by Ar. The rainbow occurs at an impact parameter $b \simeq 0.2$, corresponding to an angular momentum of $l \sim 1$. The glory is around $b \simeq 0.4$ where the curve crosses $\theta = -\pi$.

rainbow or a glory. In order to investigate the relation between the quantum mechanical and classical scattering cross section we have tested a semiclassical approximation [103, 104] which remains valid when the rainbow is close to π and overlaps with the glory. The results do not agree with the exact cross section in either shape or magnitude. In tracing the discrepancy we found that the first step of a semiclassical approximation, the replacement of the exact scattering phases δ_l in the elastic scattering amplitude $f(\theta)$,

$$f(\theta) = \frac{1}{2ik} \sum_{l=0}^{\infty} (2l+1) \left[\exp(2i\delta_l) - 1\right] P_l(\cos\theta), \tag{5.59}$$

by their Wentzel-Kramers-Brillouin (WKB) limit is valid, i.e. the resulting

cross section agrees to a very good approximation with the exact quantum mechanical result. The latter implies that the De Broglie wave length is still sufficiently small compared to the characteristic spatial variation of the potential. The break-down of the semiclassical approximation occurs in the second step: the replacement of the sum over partial waves by an integral over l (or b). In terms of the elastic scattering amplitude $f(\theta)$ (Eq. (5.59)), the second step implies the following replacement

$$\sum_l \rightarrow \int_0^\infty dl = k \int_0^\infty db. \tag{5.60}$$

The semiclassical break-down is an obvious consequence of the fact that only few partial waves contribute.

We conclude that the enhancement seen at backward angles is a pure quantum mechanical effect that can be traced to the fact that the cross section in Fig. 5.3 can be reproduced with very few partial waves. We note that due to the presence of classical singularities in the elastic cross section classical methods should be used with caution for calculating electron loss cross section for heavy targets. Furthermore, classical (or semiclassical) rainbow and glory structures will be reflected in the quantum mechanical cross section only when the deflection function for fast electrons resembles the one shown in Fig. 5.5 and, in addition, the range of impact parameters contributing to the rainbow and glory encompasses a wide range of angular momenta ($l \gg 1$).

5.5 Asymmetric Collisions: H^0 and He^+ on Ar

In this section we present results for H^0 and He^+ on Ar. Argon was chosen to be representative of heavy targets because of the availability of experimental data for these collision systems. Results presented in this section are based on the plane wave IA (Eq. (5.28)) and its various on-shell approximations (Eqs. (5.32), (5.38), and (5.41)).

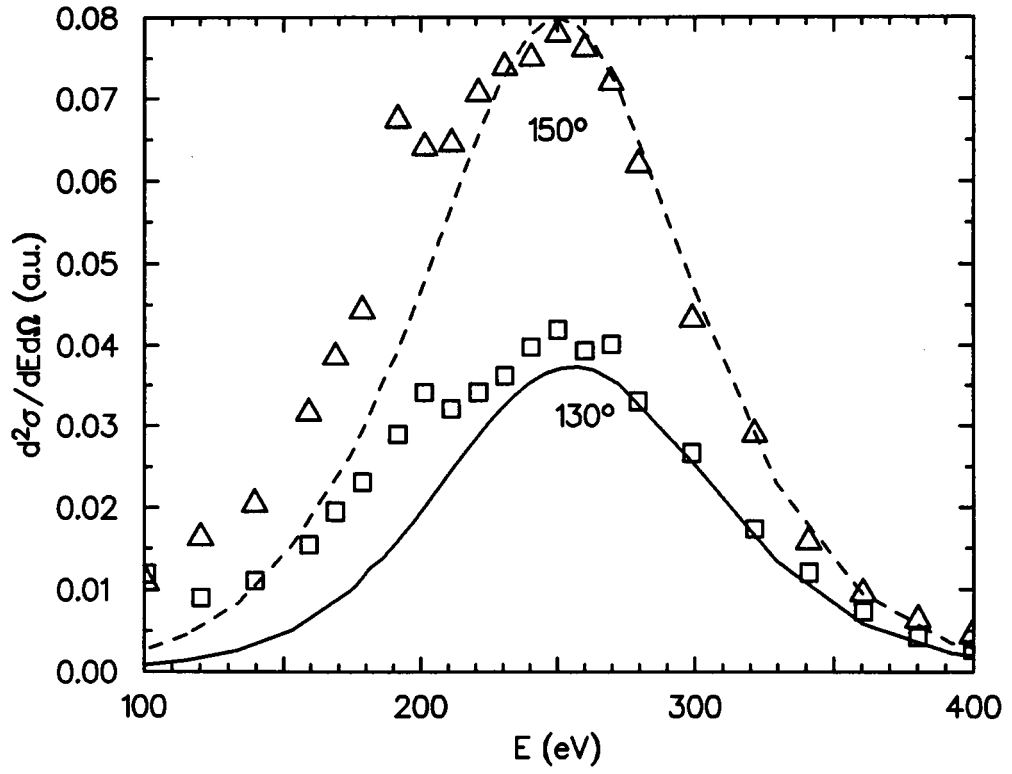

Figure 5.6: Absolute DDCS for H^0 + Ar at 0.5-MeV/u calculated by off-shell plane wave IA. —, 130^0 ; - - - 150^0 . Expt. data from Ref. [27], □, 130^0 ; △, 150^0 .

5.5.1 Doubly Differential Cross Sections

We first consider 0.5-MeV atomic hydrogen incident on Ar. Calculations of the doubly differential cross section (DDCS) for the mean field ionization at 130^0 and 150^0 are compared in Fig. 5.6 with recent measurements by Heil *et al.* [27]. A single, broad peak is observed and identified as the electron loss or binary peak resulting from projectile ionization. The shape of the ELP is nearly symmetric reflecting, to certain extent, the Compton profile of the projectile initial state (H(1s)). Even though the widths and positions of the ELP at the two angles are similar there is a large difference in the peak height. The ELP at 150^0 is almost twice as high as at 130^0 . This can be qualitatively understood by noting that the elastic cross section (Fig. 5.3) increases with

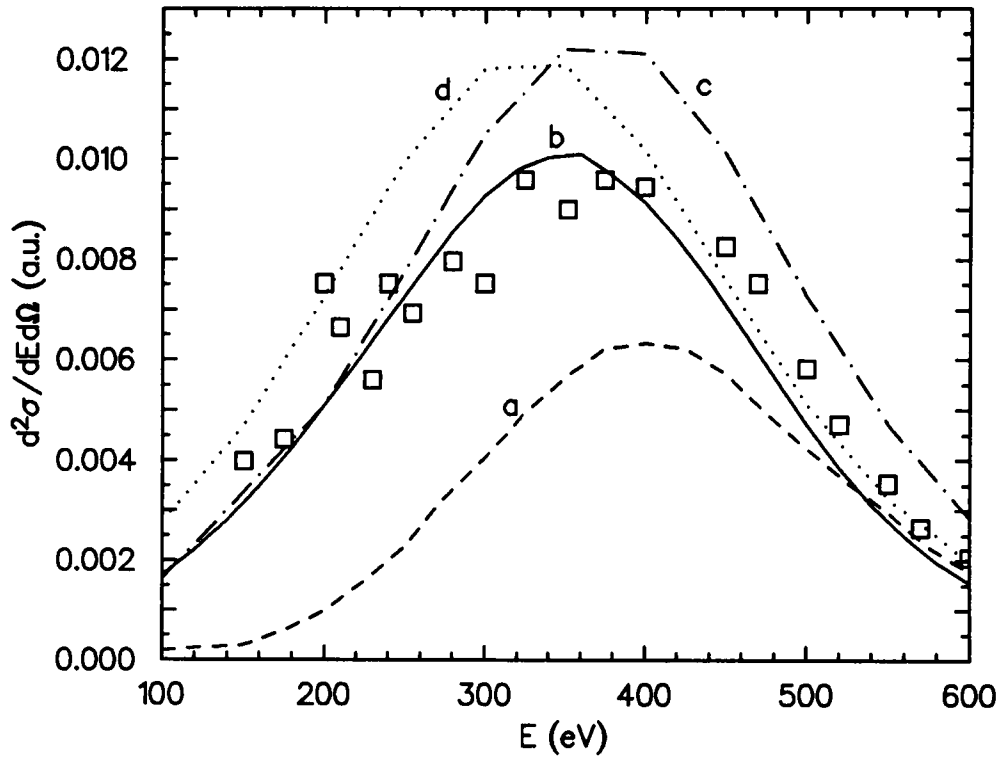

Figure 5.7: DDCS for He^+ + Ar at 0.8-MeV/u calculated with various on-shell approximations. (a) HW (Eq. (5.32)); (b) PA (Eq. (5.38)); (c) BEA (Eq. (5.41)); (d) off-shell plane wave IA (Eq. (5.28)). □, Expt. data from Ref. [24] normalized to our result.

angle in the backward direction. Overall, the agreement between theory and experiment is very good considering that the experimental data are absolute and no normalization factors are used in the comparison. At both angles the agreement with experiment is better on the higher energy side of the ELP than on the lower side. The latter is partly due to increasing target ionization contributions at lower energies. Another source could be the absence of the correlated ionization in the theory. We will explore this point further in the next chapter.

The above calculation has been performed using the full off-energy-shell T matrix elements ((5.28)). In Fig. 5.7 we compare the various on-shell approximations we discussed earlier with the plane wave IA for DDCS at

135^0 for He^+ on Ar at 0.8-MEV/u. The experimental data are normalized to curve (b) since they are relative. While the different on-shell approximations (curves a (HW), b (PA), and c (BEA) in Fig. 5.7) reproduce the shape of the ELP we find remarkable differences in the magnitude of the cross section. Obviously, the DDCS at backward angles is extremely sensitive to the on-shell approximations used. Again, its origin can be traced to the strong rise of the elastic scattering cross section at backward angles (Fig. 5.3). Since an on-shell approximation amounts, in a simplified picture, to an alteration of either the exact momentum transfer vector or the final momentum vector, one probes, in effect, the elastic cross section at different backward angles. In line with this analysis we find the DDCS at forward angles, i.e. smaller momentum transfers, is much less sensitive to choice of the on-shell approximation. In view of the simplicity of the PA given by Eq. (5.38) (curve b) and its good agreement with the exact off-shell plane wave IA (curve d), we use from now on this model for the calculation of the singly differential cross section and the peak position presented below.

5.5.2 Singly Differential Cross Sections

The angular distribution of loss electrons, i.e. the singly differential cross section (SDCS) is obtained by integrating the DDCS over all electron energies. Fig. 5.8 displays the SDCS for H^0 and He^+ on Ar at 0.5-MeV/u. The most important observation is that the SDCS closely resembles the elastic cross section. The rise at large angles following a minimum around 110^0 is seen to be present for both H^0 and He^+ projectiles. In addition, the magnitude for the two collision systems seems to be equal within experimental error bars although the theoretical calculations show that the SDCS is slightly higher for H^0 than for He^+ . The similarity in both shape and magnitude can be viewed as a direct experimental confirmation of the validity of the impulse approximation. Apart from the different width of the Compton profile, the loss cross section should be independent of the projectile and only determined by the interaction with the heavy target. Previous discrepancies, where theoretical cross sections are about a factor of 2 smaller than the experimental data [25, 36], are due to the choice of HW on-shell approximations rather than to an inadequate representation of the correlated ionization. Clearly, since only first Born calculations were available previously for the correlated ionization at backward angles more elaborate calculations including higher

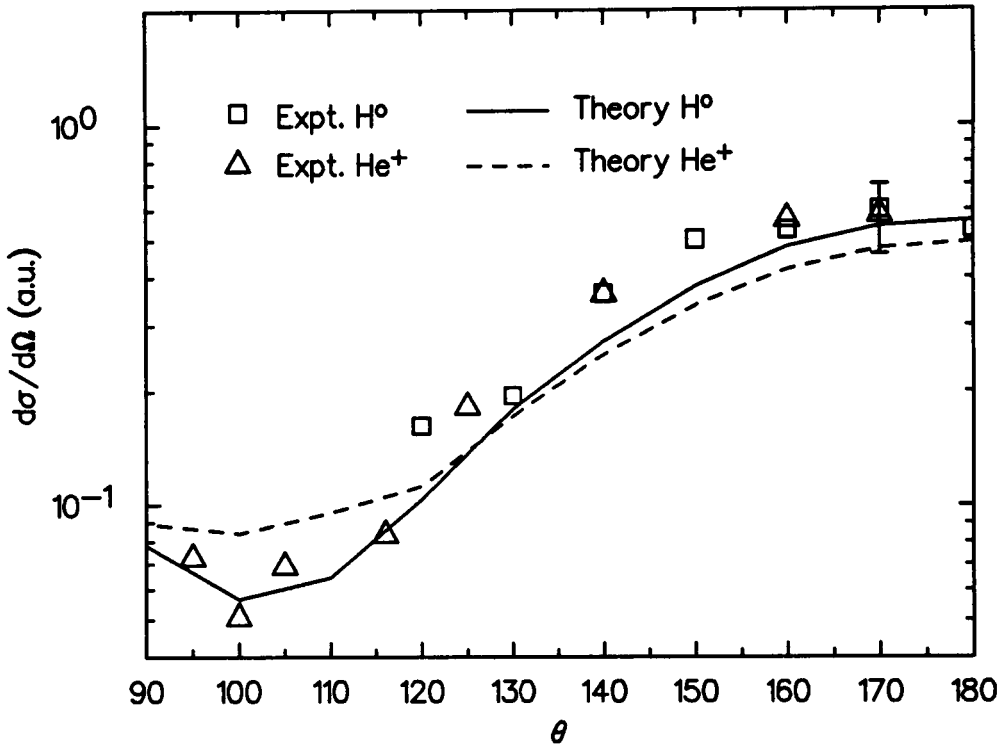

Figure 5.8: SDCS for H^0 (—), He^+ (- - -) + Ar at 0.5-MeV/u. Expt. data, H^0 from Ref. [27]; He^+ from Ref. [25].

order contributions should be performed before arriving at a more definitive conclusion. This aspect is dealt with in the next chapter.

5.5.3 Angular dependence of the peak position

In has been experimentally observed [25] that the dependence of the position in energy of the ELP on the ejection angle is non-monotonic. The expected position for elastic scattering of a free electron of well defined momentum v by a heavy particle (at rest) is $v^2/2$, independent of the scattering angle. The actual peak position is found to be shifted to energies below the expected position due to binding energy effect and the convolution of the Compton profile with a rapidly decreasing elastic cross section as a function of energy. This shift is displayed in Fig. 5.9 for the case of He^+ on Ar at

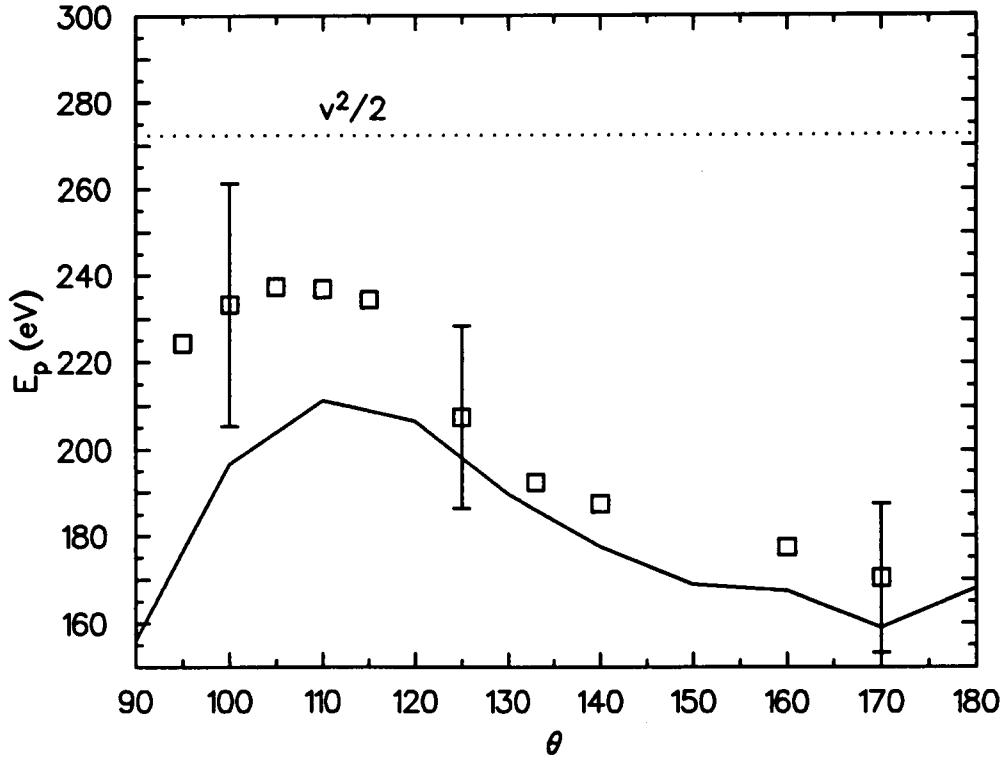

Figure 5.9: Angular variation of the peak position E_p for He^+ + Ar at 0.5-MeV/u. □, Expt. data of Ref. [25]. The free electron energy $v^2/2$ corresponds to 272 eV.

0.5MeV/u for which we find qualitative agreement between experiment and theory. We note that the peak position displays a local maximum around 110^0 , i.e. the shift is reduced by a factor of ~ 2. This angle is found to correspond to the minimum of the SDCS (Fig. 5.8) which, in turn, is related to the minimum of the elastic cross section. We therefore analyze the dependence of the elastic cross section on the electron energy around this angle as depicted in Fig. 5.10. The 110^0 curve shows a minimum due to the strong destructive partial wave interference at an energy below the free electron energy $v^2/2$. In contrast, the cross section decreases monotonically at large electron energies ($k > 5$), as intuitively expected. The net effect is a reduction of the cross section on the low-energy tail and an enhancement on the high-energy tail, and hence, a partial suppression of the peak shift to

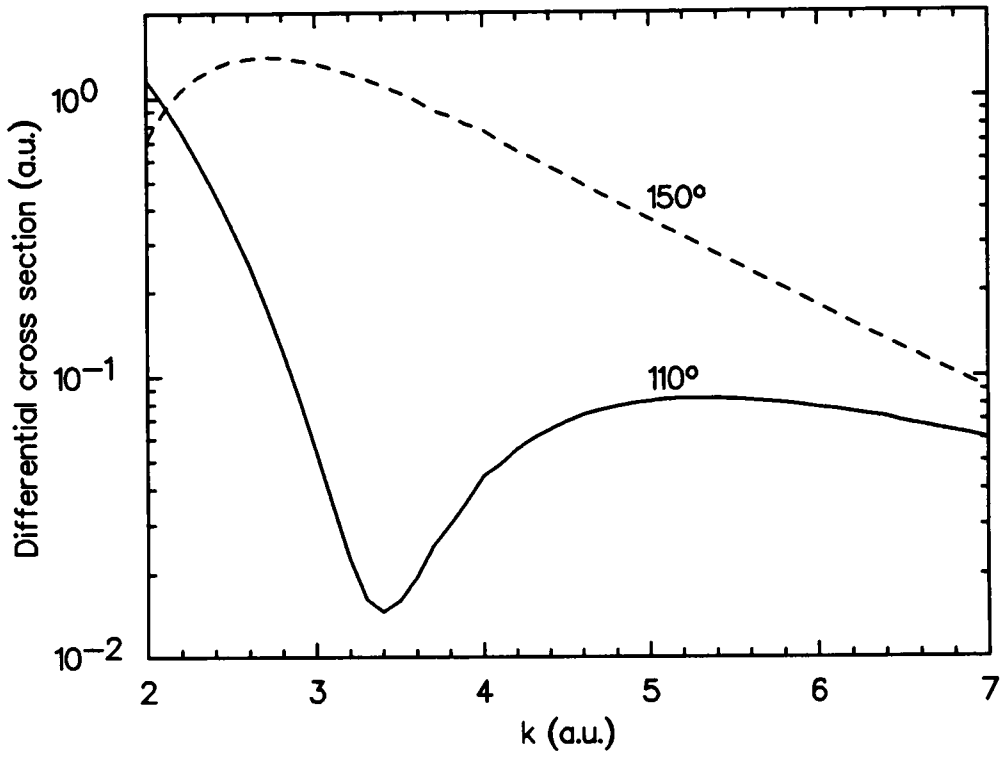

Figure 5.10: Differential cross section for elastic scattering of electrons by Ar as a function of the incident momentum k. —, 110^0 ; - - -, 150^0 .

lower energies at $\theta \approx 110^0$.

The increase of the peak shift (Fig. 5.9) at large angles reflects the fact that the slope of the elastic cross section (Fig. 5.10) as a function of k (or E) becomes steeper with increasing E, such that the opposite trend becomes operative: the high-energy tail of the ELP is reduced relative to the low-energy tail resulting in an increased peak shift.

The anomalous energy dependence of elastic cross section seen in the 110^0 curve in Fig. 5.10 has interesting implications for heavier targets. First of all, the same behavior is expected to be found at more than one angle since more minima in the elastic cross sections are present [105], which has indeed been observed for H^-,He^+ + Kr collisions [106]. Furthermore, as the target becomes heavier the minimum (as a function of energy) becomes sharper. The physical reason is that the effective electron energy is lower

for heavier targets. In general interference effects become stronger at lower energies. The stronger interference effect thus produces a sharper minimum. Since ultimately the DDCS is determined as a convolution of the elastic cross section and the Compton profile (Eq. (5.38)), the sharpness of the minimum will be reflected in the form of a "hole" in the resulting DDCS. If this would happen, the DDCS would show two peaks instead of one. This phenomenon has been demonstrated experimentally and theoretically in a recent study of the forward binary peak splitting [107, 108] by partially stripped heavy ion impact.

We conclude this section by pointing to one further implication of these findings. The forward binary peak in target ionization is, upon a frame transformation, just the electron loss peak at backward angles. By the same token the enhancement seen at backward angles for electron loss is also reflected in the forward binary electron production where the magnitude of the cross section for partially stripped ion-impact exceeds that for the fully stripped ion-impact [109, 110, 111]. It is caused by the rising elastic scattering cross section for partially-stripped ions at backward angles (Fig. 5.3). Our present study for electron loss at backward angles therefore provides a unified description of the backward and forward binary electron production mechanism, whose origin is largely dominated by the elastic scattering in the respective target or projectile fields.

5.6 Symmetric Collisions: He^+ on He

5.6.1 Two-Center Effects

For the collision system He^+ + He (0.5-MeV/u) a large disagreement has been reported between theory and experiment for the angular distribution of ejected electrons [25]. In Fig. 5.11 we display the DDCS at 180^0 using the IA, the CDW approximation and the CTMC method. The most striking feature is the importance of two-center effects at backward angles: The results of CDW and CTMC agree with each other rather well but they differ considerably from that of the IA. The CDW and the CTMC calculations, both of which contain two-center effects, show an enhancement with respect to the IA (Fig. 5.11). These effects are seen to change considerably the shape and magnitude of the DDCS at 180^0 with respect to the IA results. In fact, the

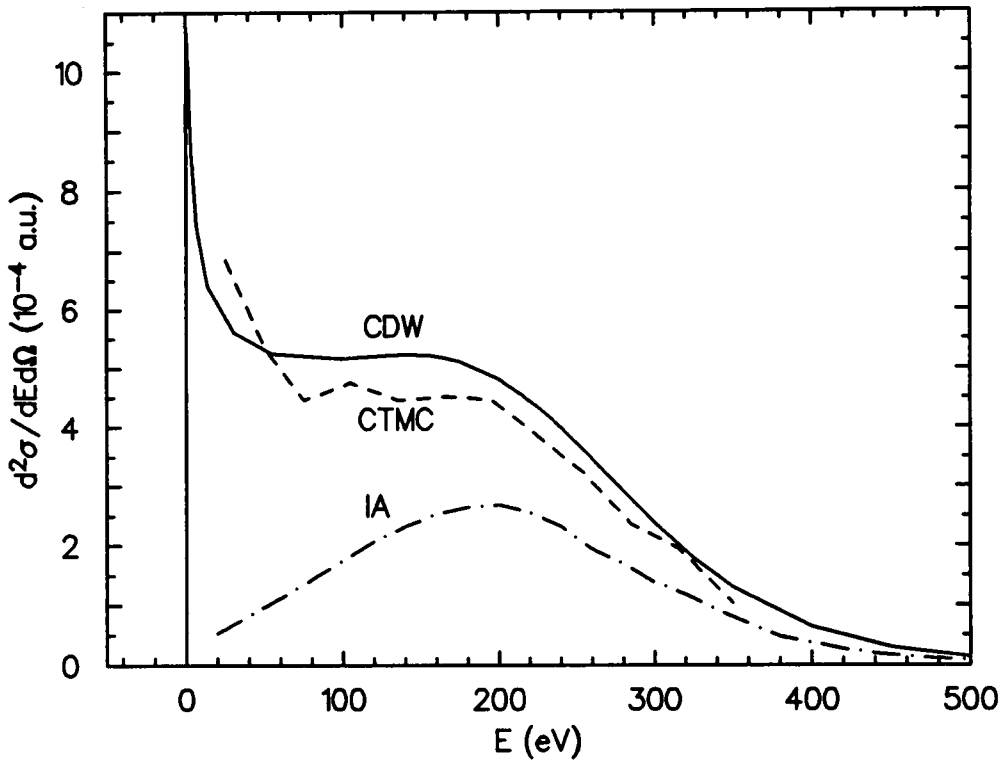

Figure 5.11: The doubly differential cross section for ejection of projectile electrons at 180^0 in 0.5-MeV/u He^+ + He collisions. Various approximations are: the CDW approximation (——) without exchange; plane wave IA (— · — · —); and the CTMC (- - -).

ELP is replaced by a shoulder at large ejection angle (180^0). Two-center effects, which have been shown to be essential in the $v/2$ electron emission for target ionization of the δ-model, are again found to be very important for projectile ionization in symmetric collisions.

To see the relative importance of two-center effects we show in Fig. 5.12 the CDW calculation of the DDCS at several angles. The ELP can be easily recognized at smaller ejection angles and clearly becomes the dominant feature of the spectrum at 90^0 . This is due to the fact that for electrons with ELP energies ($\sim v^2/2 - \varepsilon_i$) the elastic cross section for the scattering of an electron by the target core increases very rapidly for decreasing ejection angles. The large difference between the IA and the CDW calculations at 180^0

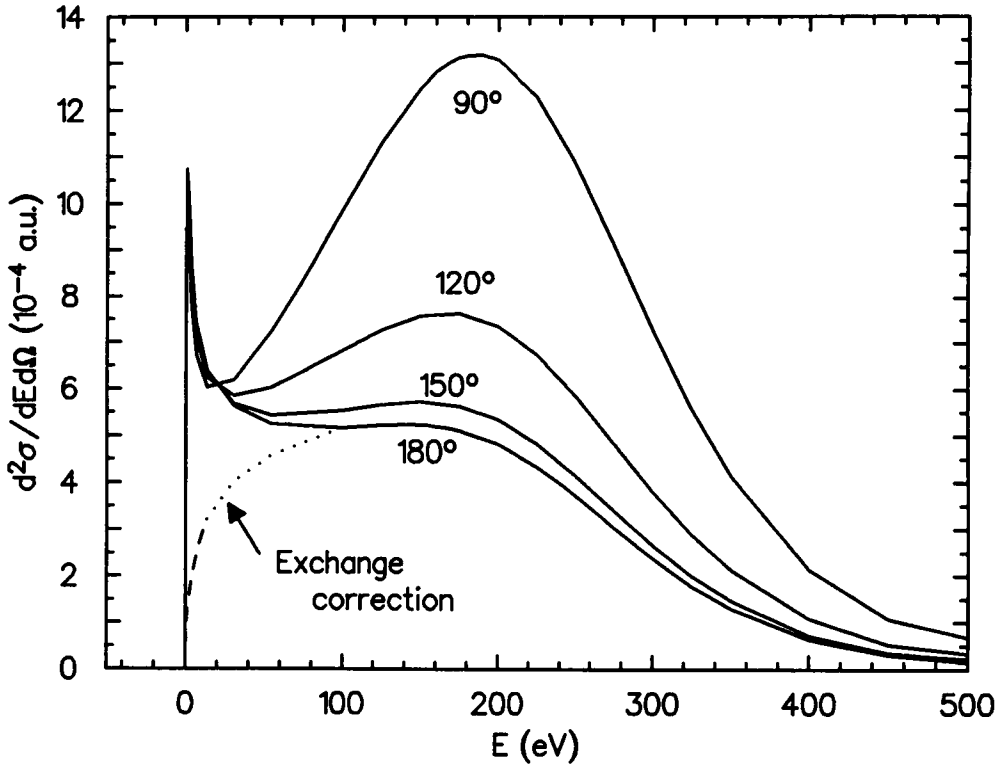

Figure 5.12: The DDCS for projectile ionization at various ejection angles in 0.5-MeV/u He^+ + He collisions by the CDW approximation. The result at 180^0 is shown with exchange corrections using the normalization factor of Ref. [97] (dashed line) (see Eq. (5.55)). The dotted line represents our extrapolation of the normalization factor of Ref. [97].

(Fig. 5.11) can be viewed as a result of the combined effect of two-center effects and the width of the projectile Compton profile for He^+ . Similar results have been reported earlier for C^+ + He collisions using the CTMC method [98] which we find here to predict very similar cross sections to the ones obtained with the CDW model.

It is interesting to note that at low electron energies the CDW cross sections exhibit a very narrow peak (Fig. 5.11 and 5.12). This peak can be readily attributed to the process of electron capture to the continuum of the neutral target core and it arises from the normalization of the target continuum wave function at low electron energies (Eq. (5.55)). Because the

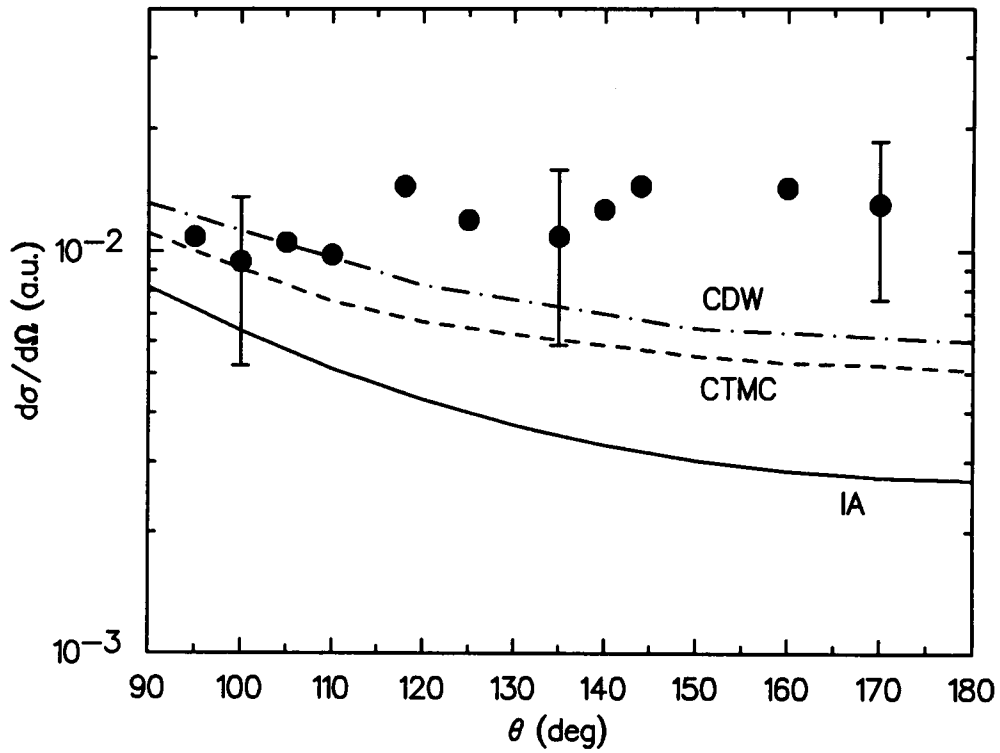

Figure 5.13: The singly differential cross section for ejection of projectile electrons in He^+ + He collisions at 0.5-MeV/u. Expt. data (•) from Köver *et al.* [25].

interaction with the target core is of short range this normalization factor is bounded and the DDCS tends to zero for extremely small electron energies ($E \rightarrow 0$). We note that the height and width of the capture to continuum peak depend very strongly on exchange. By using the continuum normalization previously calculated including exchange [97], we find that the capture to the continuum peak in the target reference frame is not visible (dashed curve in Fig. 5.12).

5.6.2 Angular Distribution

To compare our results with the experiment we display in Fig. 5.13 the SDCS as a function of the angle of the ejected electrons which is obtained

by integration of the DDCS over all electron energies. The lowest curve in the figure corresponds to the IA. Unlike in the case of heavy targets [39], the IA is not capable to account for the experimental cross sections. A clear disagreement exists in both the trend and magnitude of the cross sections. When two-center effects are accounted for, a substantial improvement is observed in both the trend and magnitude of the SDCS. This is evidenced by both the CDW and CTMC cross sections displayed in the figure. Additional improvement due to correlated ionization will be discussed in the next chapter.

Chapter 6

Projectile Ionization by Electron-Electron Interaction

6.1 Scattering Correlation

In the preceding chapter we have shown that for heavy targets, such as argon, the impulse approximation with proper treatment of the off-shell T matrix can, by and large, account for the experimentally observed cross sections for electron loss at large angles. In this case, quasi-elastic scattering of the projectile electron in the strong field of the target is found to be the dominant process for projectile ionization. However we have noticed that the IA underestimates the cross section on the lower energy side of the DDCS for H^0 on Ar. It was attributed to a combination of target ionization in the experiment and the lack of correlated ionization in the IA. For more symmetric collision systems such as He^+ on He, we have found that two-center effects enhance the cross section by a factor of 2 over the one-center IA theory. But when compared with experimental data, the enhancement is still not enough to explain the observed SDCS.

Apparently correlated ionization not accounted for by the IA, CDW, and CTMC for the mean field ionization must play an important role in reconciling the discrepancies. Correlated ionization, which is a manifestation of "scattering correlation" [81], involves the electron-electron interaction mediating directly ionization. This is to be contrasted with the electron-electron interaction generating a "mean-field" for a screened electron-nucleus interac-

tion. Ionization by direct electron-electron interaction is therefore sometimes referred to as "antiscreening" [112, 113]. Since it leads to simultaneous excitation or ionization of the target it is frequently characterized as the "doubly inelastic (DI)" process [37, 30, 31]. In order to distinguish this process from simultaneous target excitation which can, within the independent particle model, result from simultaneous interaction of the projectile electron with the (screened) target core and of the target electron with the (screened) projectile, we will refer to it as correlated DI process. The importance of the inclusion of the explicit electron-electron interaction has been demonstrated for the total ionization cross section for multiply charged hydrogenic ions [114]. The magnitude of the correlated DI has been previously analyzed within the first Born approximation and was shown to be negligible at backward emission angles [36]. We show in the following that the yield of electrons ejected at backward emission angles is significantly enhanced via a double scattering mechanism by which the projectile electron collides successively at a target electron and at the screened target nucleus. As will be shown below, this second order term dominates over the contribution of the first order. The obvious reason is that emission in the backward direction requires a large momentum transfer which is more efficiently accomplished in a double scattering event rather than in a single collision.

6.2 Approximation Method to Correlation

6.2.1 Second Born Approximation: Double Scattering

Obviously, the explicit treatment of two-electron processes for the correlated DI channel is theoretically a challenging task. Here we restrict ourselves to a second Born approximation. The subset of relevant terms of Eq. (5.11) as given by (5.13) are

$$T^{(B2)} = T^{(1)} + T^{(2)} \tag{6.1}$$

with

$$T^{(1)} = r_e^{-1} \tag{6.2}$$

$$T^{(2)} = V_C \tilde{G}_0^+ r_e^{-1} + r_e^{-1} \tilde{G}_0^+ V_C + r_e^{-1} \tilde{G}_0^+ r_e^{-1} \tag{6.3}$$

and

$$\tilde{G}_0^+ = (E + \nabla_r^2/2 - H_0(T) + i\eta)^{-1}. \tag{6.4}$$

The Green's operator $\tilde{G}_0^+$ (Eq. (6.4)) describes the propagation of the projectile electron as a free particle while the target electron propagates in the effective target field. The physical picture represented by the Born expansion (6.2) and (6.3) is schematically illustrated in Fig. 6.1. Previously, only the first order term (Eq. (6.2)) has been evaluated [30, 32, 35]. It corresponds to a single scattering depicted in Fig. 6.1. The DDCS in the first Born approximation (B1) has been shown to dominate the SI channel in the forward direction. The DI contribution quickly diminishes with increasing angles and becomes negligible at backward angles [36]. The obvious reason is that the electron-electron interaction is ineffective for emission at backward angles. In fact, classical free electron-electron scattering confines the emission to the forward hemisphere. The ejection of the projectile electron in the backward direction is therefore only due to the extremely small tail of large momentum components in the Compton profile of the target states. For this reason, the second order term in r_e^{-1} in (6.3) contributes little. However, we keep this term in order to preserve the overall asymptotic charge neutrality of the perturbation operator. The latter would be important near the forward direction and for the integral cross section. The important observation is now that the mixed terms in (6.3) describing a sequence of one collision with a target electron followed by one with the target core (or vice versa) turn out to be dominant. In Fig. 6.1 the double scattering term $V_C \tilde{G}_0^+ r_e^{-1}$ is shown as an example. The projectile electron is slowed down and deflected (to an intermediate state $\vec{k}$) in the first collision with the target electron, then is elastically scattered at the target core. This double scattering sequence mediates the large momentum transfer necessary for emission of projectile electrons at backward angles.

Numerous examples illustrate the importance of multiple-scattering in atomic collisions, particularly the double scattering. The Thomas scattering for capture [75] is a unique example that connects the classical double-scattering to its quantum mechanical counterparts [76, 115]. Double scattering is also responsible for generating backward binary electron observed in the δ-model. There have been suggestions that double scattering is important in the deflection of protons in double ionization of helium [116, 117, 118]. Of course, the importance of double scattering is not confined only to atomic

Single Scattering r_e^{-1}

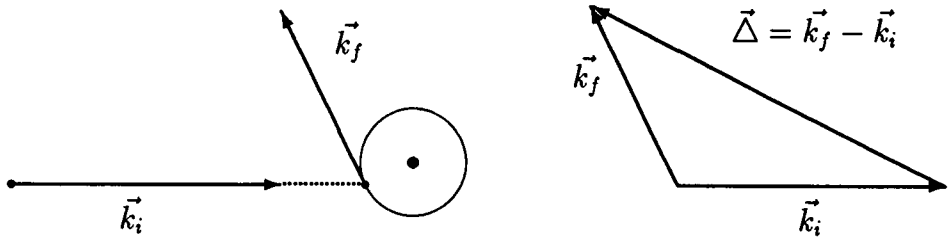

Double Scattering $V_C \tilde{G}_0^+ r_e^{-1}$

$\vec{\Delta} = \vec{\Delta}_1 + \vec{\Delta}_2$

$\vec{\Delta}_1 = \vec{k} - \vec{k}_i, \quad \vec{\Delta}_2 = \vec{k}_f - \vec{k}$

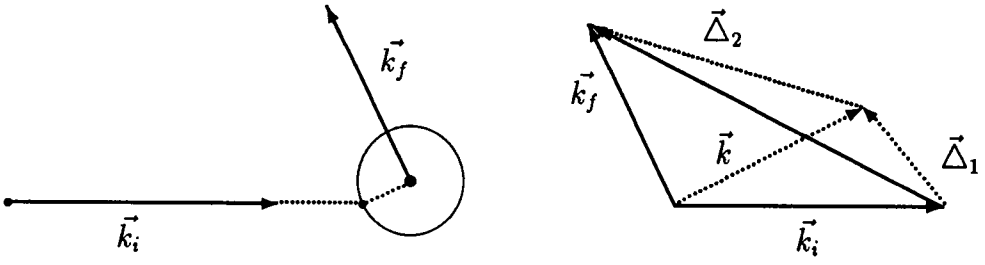

Figure 6.1: The diagrams represent schematically single scattering and double scattering of the Born expansion series for correlated ionization. The diagrams on the left depict the geometric arrangement while these on the right illustrate the addition of momenta for a given momentum transfer $\vec{\Delta} = \vec{k}_f - \vec{k}_i$. The target atom is represented by a circle with the target core at the center and the active target electron orbiting on the circle. The projectile electron of initial momentum $\vec{k}_i$ is scattered to a final momentum $\vec{k}_f$. For single scattering this can be achieved only through correlation r_e^{-1} in a single step. For double scattering, the momentum transfer is mediated in two steps via the intermediate state $\vec{k}$.

collisions or electron-atom collisions [119, 120, 121]. Other two-step processes include capture into the wake in solids [122], electron energy loss spectroscopy in solids [123], and ion neutralization at surfaces [124]. In each case, higher-order Born series dominate over the first-order term since the required large energy and momentum transfer is prohibited by the kinematics of a single collision. Therefore a two (or multi) step mechanism becomes dominant.

6.2.2 Evaluation of Cross Sections

The evaluation of (6.3) is a formidable task and requires additional simplifying approximations. We first replace the core potential by a Coulomb potential

$$V_C = -Z_T/r \tag{6.5}$$

which is valid for hydrogen (or hydrogen-like targets). The DDCS expressed in terms of the transition amplitudes as a function of the perpendicular momentum component, $\vec{q}_\perp$, is given by (see Appendix B)

$$\frac{d^2\sigma^{B2}(f)}{dEd\Omega} = \frac{2\pi}{v^2} k_f \int d\vec{q}_\perp \left| f_1(\vec{q}_\perp) + f_2(\vec{q}_\perp) \right|^2 . \tag{6.6}$$

Eq. (6.6) describes the emission of a projectile electron with wave vector $\vec{k_f}$ while the target electron is excited or ionized to the final state (f) to be specified later. The evaluation of the first order amplitude f_1 resulting from Eq. (6.2) is straight-forward yielding

$$f_1(\vec{q}_\perp) = F_{f,i}(\vec{k_f} - \vec{q})\tilde{\varphi}_i(\vec{q} - \vec{v}) \tag{6.7}$$

with

$$\begin{aligned} \vec{q} &= \vec{q}_\perp + q_0\hat{z} \\ q_0 &= (v^2/2 + \Delta E)/v \end{aligned} \tag{6.8}$$

and the inelasticity of the collision

$$\Delta E = k_f^2/2 - \varepsilon_i + \varepsilon_f^T - \varepsilon_i^T . \tag{6.9}$$

ΔE depends on both the excitation energy of the projectile electron $k_f^2/2 - \varepsilon_i$ and of the target electron. The dependence of (6.9) on ε_f^T and hence on the

summation index in Eq. (6.6) complicates the evaluation of the DDCS when the sum over all final states of the target is to be taken. In (6.7) $F_{m,n}$ is given by

$$F_{m,n}(\vec{p}) = \left[S^T_{mn}(\vec{p}) - Z_T\delta_{mn}\right]\tilde{V}_c(\vec{p}) \tag{6.10}$$

in terms of the (for $m \neq n$, inelastic) form factor S^T_{mn} of the target defined as

$$S^T_{mn}(\vec{p}) = \langle m|\exp(-i\vec{p}\cdot\vec{r_T})|n\rangle \tag{6.11}$$

and $\tilde{V}_c$ is the Coulomb potential in momentum representation

$$\tilde{V}_c(\vec{p}) = \frac{1}{(2\pi)^{3/2}}\int d\vec{r}\frac{\exp(-i\vec{p}\cdot\vec{r})}{r} = \left[\frac{2}{\pi}\right]^{1/2}\frac{1}{p^2}. \tag{6.12}$$

For hydrogenic targets the form factor can be determined analytically. Only the integral over the magnitude of the transverse momentum (Eq. (6.6)) must be performed numerically.

The evaluation of the second-order amplitude, f_2, poses, however, additional complications. Inserting a complete set of intermediate states of the target eigenstates and free particle states of the projectile electron with respect to which the Green's operator (6.4) is diagonal, gives

$$f_2(\vec{q}_\perp) = \int d\vec{p}\sum_n \frac{F_{f,n}(\vec{k_f}-\vec{p})F_{n,i}(\vec{p}-\vec{q})}{k_f^2/2+\varepsilon_f^T - p^2/2 - \varepsilon_n^T + i\eta}\tilde{\varphi}_i(\vec{q}-\vec{v}). \tag{6.13}$$

The sum in (6.13) extends over a complete set of target eigenstates including the continuum.

In order to reduce (6.13) to a manageable form we invoke a closure approximation for the sum over intermediate states referred to in the following as intermediate-states closure. The underlying idea of a closure approximation is the following: Assume that we wish to evaluate an expression of the form

$$S = \sum_{n=0}^{\infty} a(n)\langle f|n\rangle\langle n|g\rangle \tag{6.14}$$

where $a(n)$ is a state dependent coefficient and f and g are arbitrary functions. It is impractical to sum (6.14) over a large number of states. If $a(n)$ were not present, the sum can be evaluated using the completeness (closure) relation of the states

$$\sum_{n=0}^{\infty}|n\rangle\langle n| = 1 \tag{6.15}$$

to give $S = \langle f|g\rangle$. This suggests to approximate $a(n)$ by some n independent average $\langle a(n)\rangle$ in order to pull it out of the sum. Thus,

$$S \simeq \langle a(n)\rangle \sum_{n=0}^{\infty} \langle f|n\rangle\langle n|g\rangle = \langle a(n)\rangle\langle f|g\rangle. \tag{6.16}$$

In the present case, this approximation achieves completeness of the sum over intermediate states at the price of neglecting the energy differences amongst the intermediate states by replacing individual energy ε_n^T with an average energy $\langle\varepsilon_n^T\rangle$. Applying the closure to (6.13) and using the relation

$$\sum_n S_{fn}^T(\vec{p}) S_{ni}^T(\vec{q}) = S_{fi}^T(\vec{p}+\vec{q}) \tag{6.17}$$

yields

$$f_2(\vec{q}_\perp) = H_{f,i}(\vec{k_f},\vec{q})\tilde{\varphi}_i(\vec{q}-\vec{v}) \tag{6.18}$$

with

$$\begin{aligned} H_{f,i}(\vec{k_f},\vec{q}) &= \frac{1}{(2\pi)^{3/2}} \int d\vec{p} \frac{\tilde{V}_c(\vec{k_f}-\vec{p})\tilde{V}_c(\vec{p}-\vec{q})}{k_f^2/2 + \varepsilon_f^T - p^2/2 - \langle\varepsilon_n^T\rangle + i\eta} \\ &\quad \times \left[S_{fi}^T(\vec{k_f}-\vec{q}) - Z_T S_{fi}^T(\vec{k_f}-\vec{p}) - Z_T S_{fi}^T(\vec{p}-\vec{q})\right] \end{aligned} \tag{6.19}$$

where $\langle\varepsilon_n^T\rangle$ denotes the "average" energy of intermediate states used in the closure approximation. In our numerical calculations we have used $\langle\varepsilon_n^T\rangle = 0$ and we have verified that the results are not sensitive to small variations around this value. When $\langle\varepsilon_n^T\rangle$ is varied between -0.2 to 0.2 (an interval of the order of the first excitation threshold), the cross section varies within 10%. With (6.6), (6.7) and (6.18) the DDCS for ejection of projectile electron to $\vec{k_f}$ and simultaneous excitation of the target to a given final state f due to correlated DI can be expressed as

$$\frac{d^2\sigma^{B2}(f)}{dEd\Omega} = \frac{2\pi}{v^2} k_f \int d\vec{q_\perp} |\tilde{\varphi}_i(\vec{q}-\vec{v})|^2 \left|F_{f,i}(\vec{k_f}-\vec{q}) + H_{f,i}(\vec{k_f},\vec{q})\right|^2 \tag{6.20}$$

with $\vec{q}$ given by Eq. (6.8).

Since in most experiments the final state of the target is not resolved, the comparison with experiment requires summation over all target final states,

$$\frac{d^2\sigma^{B2}}{dEd\Omega} = \sum_f \frac{d^2\sigma^{B2}(f)}{dEd\Omega} \tag{6.21}$$

where the sum is understood to extend over all final states of the target including those in the continuum. This step alone presents a problem even in the first Born approximation. The sum is therefore usually performed with the help of a closure approximation [30, 31, 34] which we call final-state closure in the following. One obvious choice would be to use a final-state closure approximation similar to the one used for the intermediate states (Eq. (6.17)). However this approach would seem to be inappropriate based on results for electron impact ionization of hydrogen where it has been shown that the kinematic coupling to the final state is important [125]. Even though that calculation applies to a particular coplanar geometry, it suggests one should keep the information of the ionized state. Another alternative would be the approach used in Ref. [31] where the sum is broken into three parts. In the first part the sum is calculated exactly from the first excited state up to some state $N \gg 1$. In the second part an approximate formula is used for $n = N + 1$ to ∞. The third part is performed by integrating over the continuum states which is also exact. This method is inapplicable here for two reasons. Firstly, analytic forms of the B2 transition amplitude are not known rendering it difficult to find an approximate formula for $n = N + 1$ to ∞. Secondly, and more seriously, the question of how large N must be arises in our case. The method is practical only if N is not too large. Extensive B2 calculations of electron impact excitation of H and He [126] reveal that for large deflection angles the cross sections are very small for the first few excited states thereby indicating that a large N would be required.

We propose here an alternative method for final-state closure in which the complete set of target eigenstates is replaced by a complete set of free-particle (plane wave) eigenstates. Consequently, the sum over all final states is replaced by an integration over the momentum space. It is important, however, that the target final state be orthogonal to its initial state. This can be accomplished by Schmidt orthogonalization, i.e. by replacing $|\vec{k}\rangle$ by $|\vec{k}\rangle - |1s\rangle\langle 1s|\vec{k}\rangle$. With this choice of the final state, the target form factor (Eq. (6.11) with $|f\rangle = \vec{k}\rangle$ and $|i\rangle = \phi_i^T = |1s\rangle$) between the final state and the initial state is given by

$$S_{fi}^T(\vec{p}) = \frac{2\sqrt{2}Z_T^{5/2}}{\pi}\left[\frac{1}{[Z_T^2 + (\vec{k} - \vec{p})^2]^2} - \frac{16Z_T^4}{[Z_T^2 + k^2]^2[4Z_T^2 + p^2]^2}\right] \qquad (6.22)$$

where Z_T is the effective charge of $|1s\rangle$ state. The DDCS for projectile

electron emission with energy $E = k_f^2/2$ into the solid angle Ω, summed over all target final states is given by

$$\frac{d^2\sigma^{B2}}{dEd\Omega} = \frac{2\pi}{v^2} k_f \int d\vec{q_\perp} |\tilde{\varphi}_i(\vec{q} - \vec{v})|^2 \int d\vec{k} \left| F_{\vec{k},i}(\vec{k_f} - \vec{q}) + H_{\vec{k},i}(\vec{k_f}, \vec{q}) \right|^2 \quad (6.23)$$

In this approach the kinematic information characterizing the ionized state (momentum and energy) is preserved while the final state interaction with the target is neglected.

We can test the accuracy of this approximation for the first-order term, $F_{\vec{k},i}$, in (6.23) by comparing the differential cross section for electron impact ionization of hydrogen evaluated with free-particle final states and with Coulomb final states of the target electron. The latter takes the final state interaction with the target nucleus into account. To this end we replace in Eq. (6.23) the Compton profile of the projectile initial state by a delta function, $\delta(\vec{q} - \vec{v})$, for a monoenergetic beam. We compare the plane wave result with the Coulomb wave result for the angular distribution in Fig. 6.2. The former is higher at small angles up to around 30^0. At larger angles, the order is reversed. At small deflection angles excitation to discrete states and ionization to continuum states are known to be equally important [31]. Therefore the plane wave closure gives higher values reflecting the contribution from the excitation to discrete states implicitly taken into account through the completeness of the plane wave set (unlike the Coulomb continuum states). As the angle increases, ionization dominates over the excitation because of the large momentum transfer required in a hard collision. Only the extreme tail of the target Compton profile contributes and, therefore, the cross section becomes sensitive to the final state interactions. However, the intensity is very small with little contribution from electron-electron scattering to the DDCS at large angles since in the second-order process, we are interested in, the angular deflection is primarily effected by scattering at the target nucleus. The overall agreement suggests the usefulness of the plane-wave closure approximation.

The evaluation of (6.23) requires a considerable computational effort due to the presence of $H_{\vec{k},i}$ which must be calculated using a two-dimensional integral for every $\vec{q}$ and $\vec{k}$. However, since we are interested only in electrons ejected at the backward angles, $H_{\vec{k},i}$ can be simplified by a peaking approximation. In the backward direction $|\vec{k_f} - \vec{q}|$ is large since $\vec{q}$ points

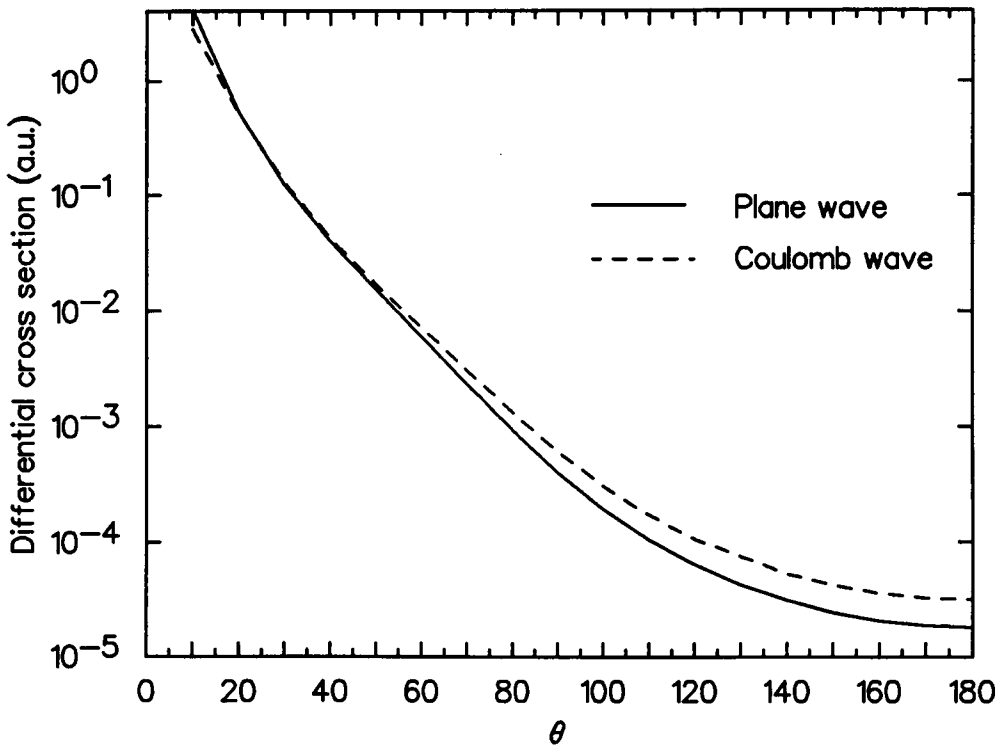

Figure 6.2: Angular distribution of incident electrons at $v_e = 4.475$ a.u. for ionization of atomic hydrogen. ——, the final target electron assumed to be a plane wave; - - -, the final target electron assumed to be a Coulomb wave.

to the forward direction by virtue of a positive q_z component in (6.8) and consequently $\tilde{V}_c(\vec{k_f} - \vec{p})$ and $\tilde{V}_c(\vec{p} - \vec{q})$ in (6.19) are localized in well-separated regions in the $\vec{p}$ space. With this approximation and using the relation (6.22), Eq. (6.19) can be reduced to a sum consisting of terms of the form

$$I_{1,2} = \int d\vec{p} \frac{1}{p^2 - k^2 - i\eta} \frac{1}{[\alpha^2 + (\vec{p} - \vec{A})^2][\beta^2 + (\vec{p} - \vec{B})^2]^2} \tag{6.24}$$

which can then be calculated using the Dalitz integral techniques [90] (see Appendix D).

Finally, in order to extend the DI model for the correlated DI process to many-electron targets, additional approximations are required to keep the model computationally affordable. First of all, the explicit interaction

between target electrons will be neglected. Therefore, the total cross section is multiplied by the number of (active) electrons in the target. Secondly, a choice of an effective target charge $Z_T(T)$ entering the target eigenstates (Eq. (6.11)) and target eigenenergies (Eq. (6.9)) has to be made to represent the interaction of the target electron with its core. In addition, an effective charge $Z_T(P)$ has to be chosen to represent the interaction of the projectile electron with the target core (Eq. (6.5)).

We will study helium and argon targets. For the case of He the ambiguities in the extension of the model to many electrons are not too severe. In this case we use the well-known variational results for the ground state of He. That is, the initial target state is assumed to be a single-zeta $1s$ wave function with an effective charge of $Z_T(T) = 1.69$ a.u., the binding energy is $-\varepsilon_i^T = (1.69)^2/2 = 1.43$ a.u., and the effective charge $Z_T(P)$ is approximated by $Z_T(P) = 2$ a.u. and the number of active target electrons is two. We have analyzed the uncertainty of our model due to the choice of $Z_T(T)$ by changing ε_i^T to the ionization potential of He ($\varepsilon_i^T = -0.904$ a.u.) and we find the results to be unchanged within an error of about 10 %.

For Ar targets the additional approximations mentioned above are much more problematic. Our results are therefore only intended to give an order of magnitude of the contribution of double scattering to the electron loss process and its limitations will be discussed below. In this case we assume that only the M shell electrons of Ar are active participants, each of which is described by an $1s$-like wave function with an effective charge $Z_T(T) = (-2\varepsilon_i^T)^{1/2} = 1.08$ a.u., corresponding to the first ionization potential. The effective interaction strength with the projectile electron $Z_T(P)$ will be treated as a free parameter.

6.3 Correlated Ionization for Near Symmetric Collisions: H^0 and He^+ on He

6.3.1 H^0 + He

To illustrate the general features of correlated ionization at backward angles, we display in Fig. 6.3 the doubly differential cross section (DDCS) at 180^0 for 0.5-MeV/u H^0 on He. For mean field ionization we use the IA which gives rise to a single peak normally referred to as the electron loss peak

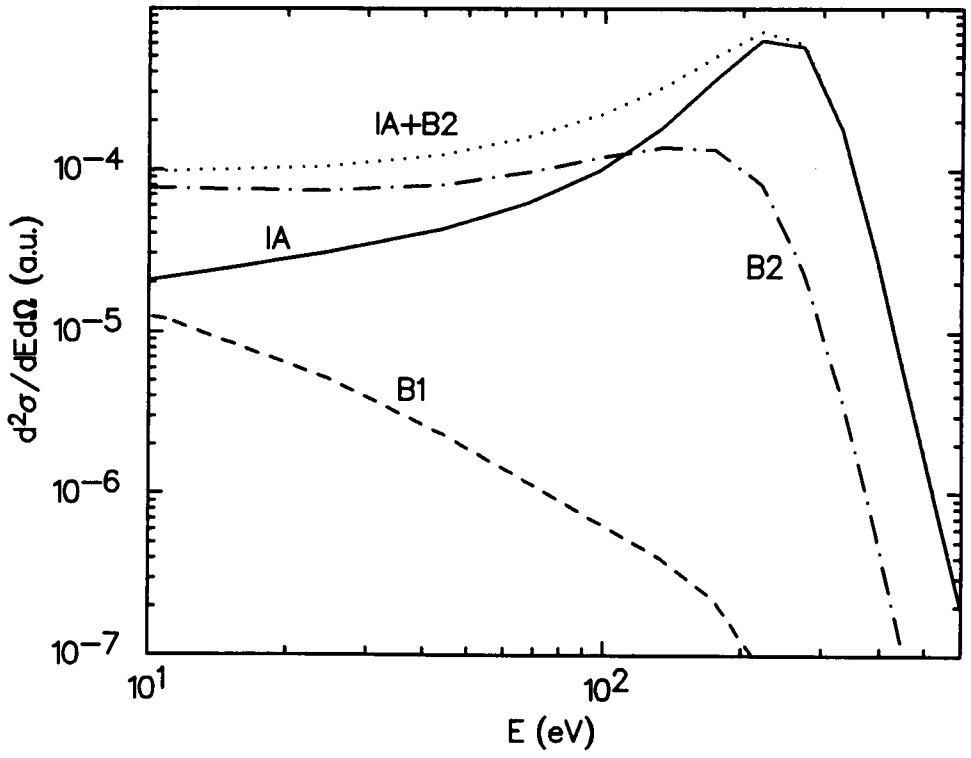

Figure 6.3: The doubly differential cross section for ejection of projectile electrons in 0.5-MeV/u H^0 + He collisions. ——, plane wave IA for the SI channel; · · · · ·, the first Born (B1) and — · — · —, the second Born (B2) approximation for the correlated DI channel.

(ELP). The position of the peak which arises from conservation of energy and momentum in a head-on binary collision between the electron and the target is approximately given by the free electron energy $v^2/2$ less the binding energy of the projectile. The exact position of the peak is usually shifted from this value because of the convolution of the momentum distribution of the projectile (Compton profile) with the elastic cross section for the scattering of the electron at the target core which decreases as a function of the energy. The width of the peak is mainly determined by the width of the Compton profile as has been discussed in the preceding chapter.

Also shown in Fig. 6.3 are the first (B1) and second Born (B2) approximation for the correlated DI process. The most striking feature is the large

difference in magnitude between the results obtained to first and second order. In accordance with previous findings [36, 119], the correlated DI cross section calculated in the B1 approximation is seen to be negligible in comparison with the IA for the SI channel. However, inclusion of double scattering in the correlated DI enhances the cross section by almost two orders of magnitude. In other words, the first Born approximation becomes completely inappropriate in this regime. Thus, double scattering is demonstrated again to be an important process whenever momentum mismatch is so large that a two-step collision is favored over a single-step one [119, 127]. In contrast to other two-step processes such as the classical Thomas double scattering for electron capture [75] there is no geometric constraint (such as the Thomas angle) for the correlated DI process. It should be noted that the approximations underlying the evaluation of the B2 terms become invalid for small k_f. The presentation of the cross section at small ejection energies, $E \lesssim 100$ eV, is for illustrative purpose only.

As can be seen in Fig. 6.3 the SI channel dominates the DDCS around the ELP and, therefore, will produce the main contribution to the singly differential cross section (SDCS) integrated over all electron energies. However, its importance quickly diminishes for lower electron energies for which the correlated DI channel eventually becomes the dominant contribution. The main reason for these different energy dependencies is that in the SI process no energy sharing between the projectile electron and the target electron takes place and, therefore, low energy electrons can originate only from the rapidly decreasing tail of the Compton profile. The picture is very different in the DI channel where the projectile electron gives off some energy to excite or ionize the target and, as a result, is slowed down and deflected to backward angles. We furthermore note that the DI channel possesses a threshold collision velocity v below which its contribution becomes negligible. This behavior has been recently observed experimentally in total loss cross sections [112].

To conclude our discussions on H^0 + He collisions we note that we have also investigated the effect of using a final two-center continuum state (CDW) for the SI channel. For the electron energies studied in Fig. 6.3 our CDW calculations only predict a very small enhancement of the DDCS with respect to the IA calculation at low electron energies (not shown in Fig. 6.3). Thus, two-center effects are not found to be very important for this case.

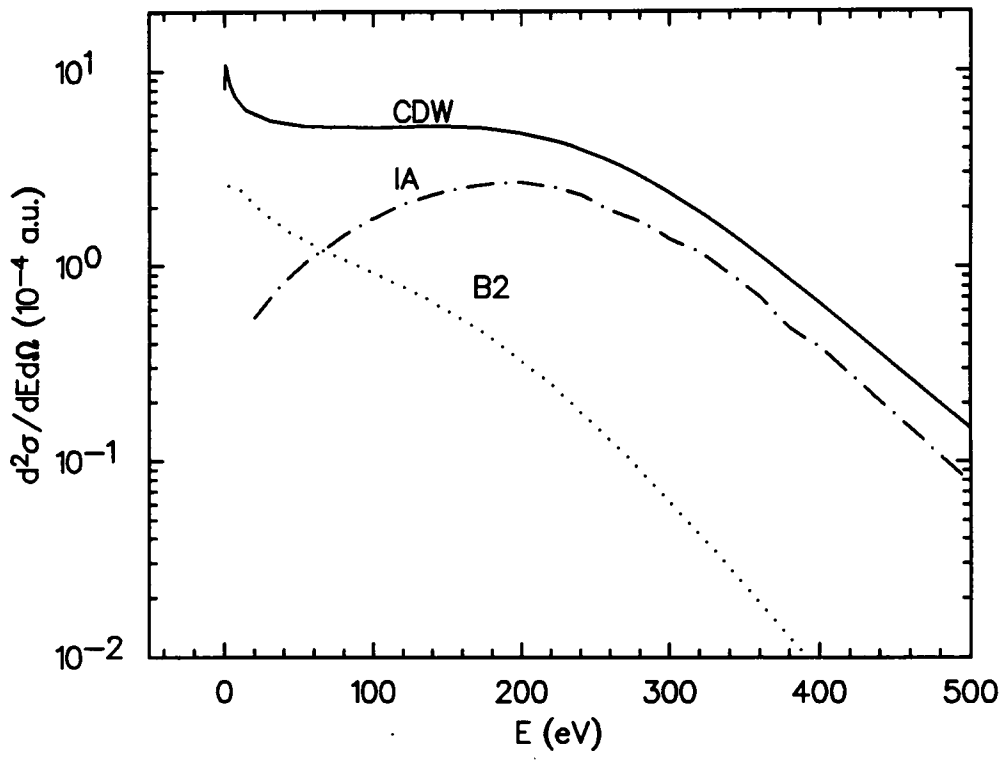

Figure 6.4: The DDCS for ejection of projectile electrons at 180^0 in 0.5-MeV/u He^+ + He collisions. The B2 (·····) approximation for the correlated DI channel is plotted together with the CDW approximation (——) without exchange and IA (– · – · –) for mean field ionization.

6.3.2 He^+ + He

For the collision system He^+ + He (0.5-MeV/u) the orbital speed of the emitted electron is twice that of H^0 and therefore the (scaled) collision speed is lower. It has been shown that even though the enhancement of the cross section due to two-center effects is large, theoretical results still lie below experimental data. In order to see how much correlated ionization contributes, we display in Fig. 6.4 the DDCS at 180^0 for the correlated DI channel using the second Born approximation. Mean field ionization for the SI channel using the IA and the CDW approximation (CTMC results already shown in Fig. 5.11 are omitted in Fig. 6.4) is also shown for comparison. The various

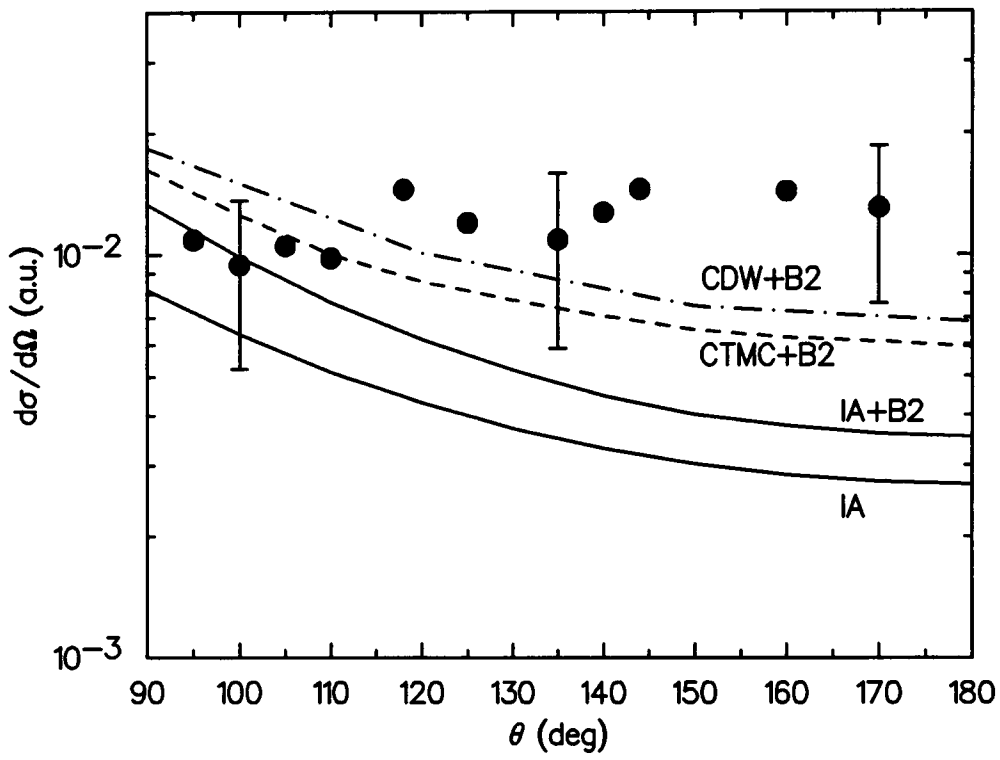

Figure 6.5: The singly differential cross section for ejection of projectile electrons in He^+ + He collisions at 0.5-MeV/u. The notation of theoretical curves is the same as in Fig. 5.13 except that correlated ionization has been added to each curve. Expt. data (•) from Köver *et al.* [25].

contributions to the cross section for the present case are very different from the ones for H^0 projectiles. The correlated DI cross section is found to peak at very small electron energies. This different behavior is related to the fact the Compton profile of He^+ is broader than the one for H^0 . Consequently the initial kinetic energy of the electron is not as well defined as for H^0 and the average energy lost by the electron in its interaction with the target turns out to be larger. The first Born term B1 (not shown in Fig. 6.4) lies again far below the B2 curve except at very low energies.

The contribution of the correlated ionization to the SDCS is displayed in Fig. 6.5. Unlike in Fig. 5.13, we have to add incoherently here the B2 results to the mean field ionization calculated with (CDW, CTMC) and without (IA)

two-center effects. When the DI channel is added to the IA results the SDCS are systematically increased by about 20% at all angles. This contribution brings the theoretical results somewhat closer to experiment in magnitude. A substantially better agreement in the total SDCS is obtained by adding the correlated DI contribution to the mean field ionization obtained with two-center effects (CDW and CTMC). At the largest angle ($\sim 170^0$) the best theoretical result (CDW + B2 curve in Fig. 6.5) nearly coincides with the lower edge of the experimental error bar. We note that the present theoretical results still appear to slightly underestimate the experimental cross sections at large angles. However, the deviations do not significantly exceed the size of the experimental error.

6.3.3 Correlated Ionization for heavy targets

The question of the importance of correlated double scattering has also been raised for collisions involving heavy targets [26, 128]. In an attempt to separate the projectile electron loss component of the ejected electron spectra coincidence techniques [26, 128] have been used for 0.5-MeV/u He^+ , H^0 + Ar collisions. By measuring the yield of ejected electrons in coincidence with ionized projectiles, these authors have demonstrated that simultaneous projectile and target ionization is very important in the low electron energy part of the spectra.

In order to understand the mechanisms responsible for this simultaneous ionization process, first order calculations were performed [26] for both target and projectile ionization including the possibility of simultaneous uncorrelated ionization of the projectile and the target. It was found that there could be a relatively large contribution to projectile ionization related to target excited states in the lower part of electron energy spectrum. However the agreement between theory and experiment was rather poor. In particular simultaneous ionization of both collision partners was severely underestimated. It is not clear from this study whether the failure of this model is due to the fact that only a first order approximation was used or because the correlated double inelastic process was neglected.

In the following we attempt to estimate the size of the correlated DI contribution to DDCS for Ar target at backward angles. For the SI channel we try to be as accurate as possible by using the exact IA (Eq. (5.27)) rather than a first Born approximation or the plane wave IA (Eq. (5.28)). It

is obviously problematic to extend our B2 calculation to the correlated DI channel to many electron targets such as Ar. One reason is the assumption of a Coulomb interaction V_T between the target core and the projectile electron (Eq. (6.5)) resulting in some ambiguity as to the choice for a suitable effective charge $Z_T(P)$ to represent the screening of the nucleus of Ar produced by the spectator electrons. A second and more important limitation of the model arises from the possibly large value of the Sommerfeld parameter $Z_T(P)/v$ which calls the validity of the Born series expansion into question.

With these difficulties in mind, our calculations for heavy targets are only intended to give a trend for the effect of including the electron-electron interaction. Fig. 6.6 displays the experimental data of Ref. [128] for collisions of 0.5-MeV H^0 on Ar. In order to assess the possible contribution from the correlated DI process we pursue the following strategy: We subtract from the experimental data all contributions from other channels we can account for. The remainder is then tentatively ascribed to the correlated DI process. We first subtract the SI cross section calculated in IA, also shown in Fig. 6.6. Furthermore, the contribution due to independent target ionization with electron emission into the same final state has to be subtracted from the data for proper comparison with our calculation for projectile ionization. We have therefore subtracted the experimental yield of target electrons emitted in H^+ + Ar collisions from the total yield of electrons ejected in H^0 + Ar collisions, furnished by Heil *et al.* [128] and also shown in Fig. 6.6. The latter provides an upper limit for the uncorrelated DI contribution since it presumes that target ionization in H^0 + Ar with electron emission at 180^0 and energies > 100eV is accompanied by projectile ionization with unit probability. Only if these coincidence requirements are met is target ionization contained in the projectile charge-state coincidence data. The peak position at $\simeq$ 200 eV in the target ionization cross section is due to target Auger emission which contributes significantly at backward angles because of its (near) isotropic angular distribution. The resulting difference represents therefore quite likely a lower limit of the correlated DI contribution with caveat, however, that the IA approximation may be inaccurate particularly because of the neglect of exchange. We find the correlated DI contribution to display a binary-like peak, shifted to lower energies by $\simeq$ 80eV. It is now quite remarkable that our B2 calculation for the correlated DI process reproduces this structure quite well. It should be noted that the shape and position of the peak is independent of the effective charge $Z_T(P)$ used as the only free parameter.

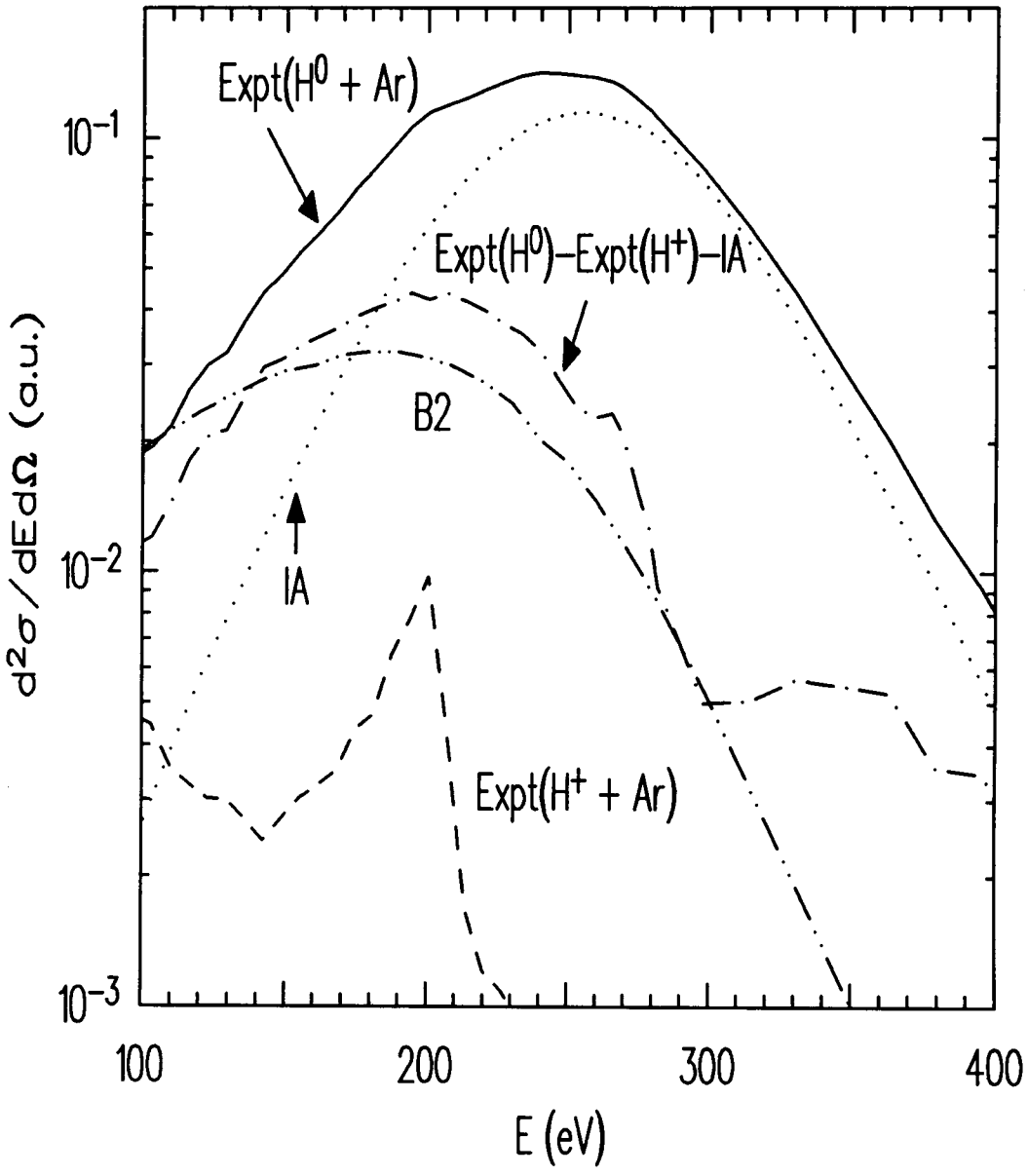

Figure 6.6: The exact IA (·····) for the SI channel and the second Born (B2 – · · – · · –) approximation for correlated DI channel estimate of the DDCS in 0.5-MeV/u H^0 + Ar collisions at 180^0 . ——, total expt. yield for H^0 +Ar and - - -, background for H^++Ar by Heil *et al.* [27]. – · – · –, the residual spectrum obtained by subtracting from the total yield the background and the exact IA.

The latter determines only the absolute magnitude and was chosen in Fig. 6.6 as $Z_T(P) = 12$. The latter choice was motivated by the observation that elastic scattering into the backward direction requires impact parameters $b \leq b_c = 0.4$. The strength of the Hartree-Fock field at a distance of $r \approx b_c$ corresponds to an effective $Z_T(P) \approx 12$. Clearly the procedure does not provide a reliable quantitative estimate for the cross section. The excellent agreement in shape and position and the order of magnitude agreement in size seems to provide, however, evidence for the identification of the residual component of the experimental spectrum as originating from the correlated DI channel.

Chapter 7

Conclusions

We have presented theoretical studies of electron emission spectra resulting from ionizing collisions between an ion (or atom) and an atom. Target ionization is investigated using an exactly solvable δ-model involving zero-range potentials represented by the Dirac δ function. Projectile ionization at backward angles is studied for H^0 and He^+ incident on target atoms He and Ar.

The integral probabilities for elastic scattering, capture, and ionization in the δ-model have been calculated as a function of Z_P/Z_T and v. The oscillatory structures in capture and elastic scattering show a remarkable resemblance to the same effects observed experimentally in 3D Coulomb problems.

The exact electron emission spectrum for target ionization in the δ-model shows an enhancement of electrons in-between the target and the projectile in velocity space at intermediate collision speeds. The enhancement is identified as $v/2$ electron emission. It is shown that $v/2$ emission is due to promotion to the continuum of the molecular orbitals and due to strong interference between the molecular orbitals. The antibinding molecular orbital is promoted into the continuum when the distance between the two centers is too close to support two bound states. The disappearance of the antibinding state is analogous to the reduction of the number of bound states in a potential well when the width of the well decreases. Consequently the electrons initially in the antibinding state are released primarily into the continuum with the possibility of being recaptured as the centers recede from each other. The peak of the $v/2$ electrons is strongly influenced by the relative interaction strengths of the electron with the two centers. Its position shows a non-

monotonic behavior as a function of the the charge asymmetry parameter Z_P/Z_T. We have shown the existence of an improper saddle point in the weak limit. The improper saddle point describes approximately the overall trend of the $v/2$ peak position as a function Z_P/Z_T. That trend is in qualitative agreement with experimental findings. Three-body effects are found to be important to the yield of the $v/2$ electron emission. The largest yield is found for near symmetric collisions at intermediate collision speeds.

The electron emission spectrum depends sensitively on the collision speed. In slow collisions, the single $v/2$ hump bifurcates into two peaks due to interference effects. In fast collisions multiple scattering peaks are shown to be a dominant feature in the ionization spectrum. The mechanism is closely related to the Fermi acceleration map where successive collisions of a particle between a moving wall and a stationary wall gives rise to peaks at multiples of the collision speed. It is a manifestation of three-body effects at high energies. In particular, double scattering has been shown to lead to the formation of a backward binary peak which resembles closely the electron loss peak at backward angles.

Projectile ionization spectrum in three dimensions involving Coulomb interactions has been shown to be composed of two parts, mean field ionization and correlated ionization. The former is caused by the interaction of projectile electron with the screened target core and the latter by the electron-electron interaction.

Mean field ionization was assumed to be caused by an effective potential, much like target ionization by a structureless projectile. It was treated in an impulse approximation (IA), continuum distorted wave (CDW approximation, and the classical trajectory Monte Carlo (CTMC) method. For asymmetric collisions ($Z_P \ll Z_T$) using the IA we have shown that proper treatment of the effective potential and the off-energy-shell scattering matrix element is required to describe experimental data. The theoretical angular distribution of ejected electrons, as well as the peak position, are in good agreement with experimental data. However, it is pointed out that the low energy side of the DDCS as given by the IA is poorly described by mean field ionization alone. For more symmetric collisions ($Z_P \sim Z_T$) two center effect has been shown to enhance the cross section considerably. This has been evidenced by the fact that approximations with two-center effects included like CDW and CTMC contribute twice as much to the cross section as the IA does. Three-body effects, the importance of which has been clearly demon-

strated in $v/2$ electron emission in the δ-model, is again found to be the essential mechanism for production of electrons in near symmetric collisions.

For the correlated ionization we have used the concept of multiple scattering developed in the $\delta-$model. Correlated ionization is treated in terms of a double scattering mechanism represented by a second Born approximation. Our treatment for projectile ionization is applicable to atomic collision problems involving structured projectile and structured target for either symmetric or asymmetric collision systems. We find that the double scattering mechanism, by which the projectile electron scatters first at the target electron followed by another scattering at the target core (or vice versa), is dominant over the direct electron-electron scattering. The large momentum transfer necessary to eject the projectile electron to backward angles is mediated through two steps rather than a single step. For heavy targets (Ar), the contribution of correlated ionization resolves the observed discrepancy on the low energy side of the DDCS. Together with the mean field ionization, they give excellent agreement for electron loss of H^0 on Ar. Inclusion of correlated ionization and two center effects improves significantly the agreement between theory and experiment for He^+ on He.

In closing, we point out that many results derived from the study of the δ-model including the capture and elastic scattering oscillations, $v/2$ electron emission, and multiple scattering peaks are quite generic. Furthermore, they could prove useful for the study of collisions with negative ions (e.g. H^-) as projectiles. Electrons lost from the projectile thus would be moving in the field of two short ranged asymptotically-neutral potentials. Complications arising from final state Coulomb interactions are therefore absent. Our results stress the symmetry between target ionization and projectile ionization in general, and between the forward binary and backward binary peaks in particular. They provide a unified description of projectile ionization and target ionization.

Bibliography

Bibliography

[1] N. Stolterfoht. *Structure and Collisions of Ions and Atoms* 5, *Topics in Current Physics*, ed. I. A. Sellin, (Springer-Verlag, Berlin, 1978) p. 155.

[2] M. E. Rudd and J. H. Macek. *Case Stud. in Atomic Phys.* 3, 47 (1972).

[3] M. R. C. McDowell and J. P. Coleman. *Introduction to the theory of ion-atom collisions*, (North-Holland, Amsterdam, 1970).

[4] A. Salin. *J. Phys. B* 2, 631 (1969).

[5] J. Macek. *Phys. Rev. A* 1, 235 (1970).

[6] C. B. Crooks and M. E. Rudd. *Phys. Rev. Lett.* 25, 1599 (1970).

[7] R. E. Olson. *Phys. Rev. A* 27, 1871 (1983).

[8] R. E. Olson. *Phys. Rev. A* 33, 4397 (1986).

[9] G. Bandarage and R. Parson. *Phys. Rev. A* 41, 5878 (1990).

[10] T. G. Winter and C. D. Lin. *Phys. Rev. A* 29, 3071 (1984).

[11] W. Meckbach, P. J. Focke, A. R. Goni, S. Suarez, J. Macek, and M. G. Menendez. *Phys. Rev. Lett.* 57, 1587 (1986).

[12] G. Bernardi, S. Suarez, P. F. Fainstein, C. Garibotti, W. Meckbach, and P. Focke. *Phys. Rev. A* 40, 6863 (1989).

[13] V. D. Irby, T. J. Gay, J. Wm. Edwards, E. B. Hale, M. L. McKenzie, and R. E. Olson. *Phys. Rev. A* 37, 3612 (1988).

[14] T. J. Gay, H. G. Berry, E. B. Hale, V. D. Irby, and R. E. Olson. *Nucl. Instrum. Meth. B* 31, 336 (1988).

[15] G. Bernardi, P. Fainstein, and C. Garibotti S. Suarez. *J. Phys. B* 23, L139 (1990).

[16] T. J. Gay, M. W. Gealy, and M. E. Rudd. *J. Phys. B* 23, L823 (1990).

[17] G. Bernardi, S. Suarez, C. Garibotti, W. Meckbach, and P. Focke. *J. Phys. B* 23, L829 (1990).

[18] J. Burgdörfer, J. Wang, and A. Bárány. *Phys. Rev. A* 38, 4919 (1988).

[19] J. Wang, J. Burgdörfer, and A. Bárány. *Nucl. Instrum. Meth. B*40/41, 65 (1989).

[20] J. Wang, J. Burgdörfer, and A. Bárány. *Phys. Rev. A* 43, 4036 (1991).

[21] D. Burch, H. Wieman, and W. B. Ingalls. *Phys. Rev. Lett.* 30, 823 (1973).

[22] W. E. Wilson and L. H. Toburen. *Phys. Rev. A* 7, 1535 (1973).

[23] M. M. Duncan and M. G. Menendez. *Phys. Rev. A* 16, 1799 (1977).

[24] Á. Kövér, D. Varga, Gy Szabó, D. Berényi, I. Kádár, , S. Ricz, J. Végh, and G. Hock. *J. Phys. B* 16, 1017 (1983).

[25] Á. Kövér, Gy Szabo, L. Gulyás, K. Tökési, D. Berényi, O. Heil, and K. O. Groeneveld. *J. Phys. B* 21, 3231 (1988).

[26] R. D. DuBois and S. T. Manson. *Phys. Rev. A* 42, 1222 (1990).

[27] O. Heil. *Private communication*, 1991.

[28] F. Drepper and Briggs J. S. *J. Phys. B* 9, 2063 (1976).

[29] M. Breinig, S. B. Elston, H. Huldt, L. Liljeby, C. R. Vane, S. D. Berry, G. A. Glass, S. Schauer, I. A. Sellin, G. D. Alton, S. Datz, S. Overbury, R. Laubert, and M. Suter. *Phys. Rev. A* 25, 3015 (1982).

[30] J. S. Briggs and M. H. Day. *J. Phys. B* 13, 4797 (1980).

[31] M. H. Day. *J. Phys. B* 14, 231 (1981).

[32] A. K. Kaminsky, N. G. Myakishev, and M. I. Popova. *J. Phys. B* 13, 1161 (1980).

[33] D. H. Jakubassa. *J. Phys. B* 13, 2099 (1980).

[34] J. Burgdörfer, M. Breinig, S. B. Elston, and I. A. Sellin. *Phys. Rev. A* 28, 3277 (1983).

[35] R. D. DuBois and S. T. Manson. *Phys. Rev. Lett.* 57, 1130 (1986).

[36] H. M. Hartley and H. R. J. Walters. *J. Phys. B* 20, 3811 (1987).

[37] D. R. Bates and G. Griffing. *Proc. Phys. Soc. A*67, 663 (1954).

[38] D. R. Bates and G. Griffing. *Proc. Phys. Soc. A*68, 90 (1955).

[39] J. Wang, C. O. Reinhold, and J. Burgdörfer. *Phys. Rev. A* 44, (in press, 1991).

[40] J. Wang, C. O. Reinhold, and J. Burgdörfer. *Phys. Rev. A* , (in press, 1991).

[41] H. A. Bethe and E. E. Salpeter. *Quantum Mechanics of One- and Two-Electron Atoms*, (Springer, Berlin, 1957).

[42] G. Breit. *Phys. Rev.* 71, 215 (1947).

[43] M. L. Goldberger and F. Seitz. *Phys. Rev.* 71, 294 (1947).

[44] H. Bethe and R. Peierls. *Proc. Roy. Soc. A*148, 146 (1935).

[45] H. A. Bethe and C. Longmire. *Phys. Rev.* 77, 647 (1950).

[46] Yu. N. Demokov and V. N. Ostrovskii. *Zero-range Potentials and Their Applications in Atomic Physics*, (Plenum, New York, 1958).

[47] B. H. Armstrong. *Phys. Rev.* 131, 1132 (1963).

[48] K. Dettmann and G. Leibfried. *Phys. Rev.* 148, 1271 (1966).

[49] R. Aaron, R. Amado, and B. W. Lee. *Phys. Rev.* 121, 319 (1961).

[50] S. Susskind and R. Jensen. *Phys. Rev. A* 38, 711 (1988).

[51] K. J. LaGattuta. *Phys. Rev. A* 40, 683 (1989).

[52] G. Scheitler and M. Kleber. *Z. Phys. D* 9, 267 (1988).

[53] S. K. Zhdanov and A. S. Chikhachev. *Sov. Phys. Dolk.* 19, 696 (1975).

[54] W. Dappen. *J. Phys. B* 10, 2399 (1977).

[55] H. Danared. *J. Phys. B* 17, 2619 (1984).

[56] S. M. Blinder. *Phys. Rev. A* 37, 973 (1988).

[57] P. R. Wallace. *Mathematical Analysis of Physical Problems*, (Dover Pub. Inc, New York, 1984).

[58] S. M. Blinder. *J. Math. Phys.* 22, 306 (1981).

[59] K. Gottfried. *Quantum Mechanics*, (Benjamin, New York, 1966).

[60] W. H. Press, B. P. Flannery, S. A. Teukolsky, and W. T. Vetterling. *Numerical Recipes: The Art of Scientific Computing*, (Cambridge Univ. Press, Cambridge, 1986).

[61] A. Jain, C. D. Lin, and W. Fritsch. *Phys. Rev. A* 36, 2041 (1987).

[62] D. A. Park. *Introduction to the quantum theory*, (McGraw-Hill, New York, 1974) p.624.

[63] M. Rakovic and E. Solovev. *Phys. Rev. A* 41, 3635 (1990).

[64] D. C. Lorents and W. Aberth. *Phys. Rev.* 139, A1017 (1966).

[65] H. F. Helbig and E. Everhart. *Phys. Rev.* 136, A674 (1964).

[66] R. P. Marchi and F. T. Smith. *Phys. Rev.* 139, A1025 (1965).

[67] T. A. Green and R. E. Johnson. *Phys. Rev.* 152, 9 (1966).

[68] M. L. Goldberger and K. M. Watson. *Collision Theory*, (Wiley, New York, 1964).

[69] C. Garibotti and J. Miraglia. *Phys. Rev. A* 21, 572 (1980).

[70] M. Brauner and J. Briggs. *J. Phys. B* 19, L325 (1986).

[71] J. Delos. *Rev. Mod. Phys.* 53, 287 (1981).

[72] P. van der Straten, R. Morgenstern, and A. Niehaus. *in 15th International Conference on the Physics of Electronic and Atomic Collisions, Abstracts of Contributed Papers*, ed. J. Geddes et al., (Brighton, UK, 1987) p. 605.

[73] R. G. Newton. *Scattering theory of waves and particles*, (McGraw-Hill, New York, 1966).

[74] T. J. Gay, M. W. Gealy, and M. E. Rudd. *in 16th International Conference on the Physics of Electronic and Atomic Collisions, Abstracts of Contributed Papers*, ed. A. Dalgarno et al., (New York, 1989) p. 436.

[75] L. H. Thomas. *Proc. R. Soc. (London) A* 114, 561 (1927).

[76] R. Shakeshaft and L. Spruch. *Rev. Mod. Phys.* 51, 369 (1979).

[77] E. Fermi. *Phys. Rev* 75, 1169 (1949).

[78] J. Burgdörfer, J. Wang, and R. Ritchie. *Physica Scripta*, in press (1991).

[79] M. M. Duncan and M. G. Menendez. *Phys. Rev. A* 19, 49 (1979).

[80] H. R. J. Walters. *J. Phys. B* 8, L54 (1975).

[81] J. H. McGuire. *Phys. Rev. A* 36, 1114 (1987).

[82] G. F. Chew. *Phys. Rev.* 80, 196 (1950).

[83] Dz Belkic. *J. Phys. B* 11, 3529 (1978).

[84] D. S. F. Crothers and J. F. McCann. *J. Phys. B* 16, 3229 (1983).

[85] R. Abrines and I. C. Percival. *Proc. Phys. Soc. London* 88, 861 (1966).

[86] R. E. Olson and A. Salop. *Phys. Rev. A* 16, 531 (1977).

[87] K. Dettmann. *Springer Tracts in Modern Phys,* 58, 119 (1971).

[88] J. S. Briggs. *J. Phys. B* 10, 3075 (1977).

[89] J. C. Y. Chen and A. C. Chen. *Advances in atomic and molecular physics* 8, ed. D. R. Bates and I. Easterman, (Academic, New York, 1972) p. 78.

[90] C. J. Joachain. *Quantum collision theory,* (North-Holland, Amsterdam, 1983).

[91] T. F. M. Bonsen and L. Vriens. *Physica* 47, 307 (1970).

[92] N. Stolterfoht, D. Schneider, J. Tanis, H. Altevogt, A. Salin, P. D. Fainstein, R. Rivarola, J. P. Grandin, J. N. Scheurer, S. Andriamonje, D. Bertault, and J. F. Chemin. *Europhys. Lett.* 4, 899 (1987).

[93] P. D. Fainstein, V. H. Ponce, and R. D. Rivarola. *J. Phys. B* 21, 287 (1988).

[94] R. E. Olson, T. J. Gay, H. G. Berry, E. B. Hale, and V. D. Irby. *Phys. Rev. Lett.* 59, 36 (1987).

[95] C. A. Falcon C. O. Reinhold and J. E. Miraglia. *J. Phys. B* 20, 3737 (1987).

[96] C. O. Reinhold and R. E. Olson. *Phys. Rev. A* 39, 3861 (1989).

[97] D. H. Jakubassa-Amundsen. *J. Phys. B* 19, 3989 (1989).

[98] L. H. Toburen, R. D. DuBois, C. O. Reinhold, D. R. Schultz, and R. E. Olson. *Phys. Rev. A* 42, 5338 (1990).

[99] R. H. Garvey, C. J. Jackman, and A. E. S. Green. *Phys. Rev. A* 12, 1144 (1975).

[100] R. D. DuBois and M. E. Rudd. *J. Phys. B* 9, 2657 (1976).

[101] K. Taulbjerg. *J. Phys. B* 23, L761 (1990).

[102] Z. Chen, D. Madison, and C. D. Lin. *Preprint,* 1991.

[103] P. Pechukas. *Phys. Rev.* 181, 166 (1969).

[104] M. V. Berry and K. E. Mount. *Rep. Prog. Phys.* 35, 315 (1972).

[105] I. E. McCarthy, C. J. Noble, B. A. Phillips, and A. D. Turnbull. *Phys. Rev. A* 15, 2173 (1977).

[106] M. M. Duncan and M. G. Menendez. *Phys. Rev. A* 23, 1085 (1981).

[107] C. Kelbch, S. Hagmann, S. Kelbch, R. Mann, R. E. Olson, S. Schmidt, and H. Schmidt-Böcking. *Phys. Lett. A*139, 304 (1989).

[108] C. O. Reinhold, D. R. Schultz, R. E. Olson, C. Kelbch, R. Koch, and H. Schmidt-Bocking. *Phys. Rev. Lett.* 66, 1842 (1991).

[109] P. Richard, D. H. Lee, T. J. M. Zouros, J. M. Sanders, and J. L. Shinpaugh. *J. Phys. B* 23, L213 (1990).

[110] C. O. Reinhold, D. R. Schultz, and R. E. Olson. *J. Phys. B* 23, L591 (1990).

[111] R. Shingal, Z. Chen, K. R. Karim, C. D. Lin, and C. P. Bhalla. *J. Phys. B* 23, L637 (1990).

[112] H. P. Hulskotter, W. E. Meyerhof, E. Dillard, and N. Guardala. *Phys. Rev. Lett.* 63, 1938 (1989).

[113] J. H. McGuire, N. Stolterfoht, and P. R. Simony. *Phys. Rev. A* 24, 97 (1981).

[114] E. C. Montenegro and W. E. Meyerhof. *Phys. Rev. A* 43, 2289 (1991).

[115] J. H. McGuire, P. R. Simony, O. L. Weaver, and J. Macek. *Phys. Rev. A* 26, 1109 (1982).

[116] E. Horsdal, B. Jensen, and K. O. Nielsen. *Phys. Rev. Lett.* 57, 1414 (1986).

[117] J. P. Giese and E. Horsdal. *Phys. Rev. Lett.* 60, 2018 (1988).

[118] J. F. Reading, A. L. Ford, and X. Fang. *Phys. Rev. Lett.* 62, 245 (1989).

[119] V. S. Potapov. *Zh. Eksp. Teor. Fiz.* 63, 2094 (1972).

[120] B. D. Buckley and H. R. J. Walters. *J. Phys. B* 7, 1380 (1974).

[121] B. D. Buckley and H. R. J. Walters. *J. Phys. B* 8, 1693 (1975).

[122] J. Burgdörfer, J. Wang, and J. Müller. *Phys. Rev. Lett.* 62, 1599 (1989).

[123] P. Ascarelli and M. Tomellini. *Solid State Comm.* 68, 683 (1988).

[124] U. Thumm and J. S. Briggs. *Nucl. Instr. Meth. B*43, 471 (1989).

[125] F. W. Byron Jr, C. J. Joachain, and B. Piraux. *J. Phys. B* 16, L769 (1983).

[126] J. Wang and J. Burgdörfer. *Unpublished*, (1990).

[127] R. Shakeshaft. *Phys. Rev. A* 16, 1458 (1977).

[128] O. Heil, R. D. DuBois, R. Maier, M. Kuzel, and K. O. Groeneveld. *Nucl. Instrum. Meth. B* 56/57, 282 (1991).

Appendices

Appendix A

Evaluation of $\frac{\partial \psi}{\partial t}$ and $\frac{\partial^2 \psi}{\partial x^2}$ in 3.2.1

The partial derivatives of ψ with respect to t and x can be calculated from (3.10) as

$$\begin{aligned}\frac{\partial \psi}{\partial t} &= \exp(ivx/2 - iv^2t/8)\sum_n a_n\left[\frac{\partial u_n}{\partial x_P}\frac{\partial x_P}{\partial t} + \frac{\partial u_n}{\partial t} - i\frac{v^2}{8}u_n\right] \\ &+ \exp(-ivx/2 - iv^2t/8)\sum_n b_n\left[\frac{\partial w_n}{\partial x_T}\frac{\partial x_T}{\partial t} + \frac{\partial w_n}{\partial t} - i\frac{v^2}{8}w_n\right] \quad \text{(A.1)}\end{aligned}$$

and

$$\begin{aligned}\frac{\partial \psi}{\partial x} &= \exp(ivx/2 - iv^2t/8)\sum_n a_n\left[\frac{\partial u_n}{\partial x_P}\frac{\partial x_P}{\partial x} + i\frac{v}{2}u_n\right] \\ &+ \exp(-ivx/2 - iv^2t/8)\sum_n b_n\left[\frac{\partial w_n}{\partial x_T}\frac{\partial x_T}{\partial x} - i\frac{v}{2}w_n\right]. \quad \text{(A.2)}\end{aligned}$$

Differentiation of (A.2) with respect to x again yields

$$\begin{aligned}\frac{\partial^2 \psi}{\partial x^2} &= \exp(ivx/2 - iv^2t/8)\sum_n a_n \times \\ &\left[\frac{\partial^2 u_n}{\partial {x_P}^2}\left(\frac{\partial x_P}{\partial x}\right)^2 + \frac{\partial u_n}{\partial x_P}\left(\frac{\partial^2 x_P}{\partial x^2} + iv\frac{\partial x_P}{\partial x}\right) - \frac{v^2}{4}u_n\right]\end{aligned}$$

$$+ \quad \exp(-ivx/2 - iv^2t/8)\sum_n b_n \times \tag{A.3}$$
$$\left[\frac{\partial^2 w_n}{\partial x_T{}^2}\left(\frac{\partial x_T}{\partial x}\right)^2 + \frac{\partial w_n}{\partial x_T}\left(\frac{\partial^2 x_T}{\partial x^2} - iv\frac{\partial x_T}{\partial x}\right) - \frac{v^2}{4}w_n\right].$$

Inserting Eqs. (A.1) and (A.3) into (3.3) and making use of the relation $\partial^2 x_{T,P}/\partial x^2 = 2\delta(x \pm vt/2)$, one obtains the following identity

$$\begin{aligned}
0 &= \left[i\frac{\partial}{\partial t} + \frac{1}{2}\frac{\partial^2}{\partial x^2} + Z_T\delta(x+vt/2) + Z_P\delta(x-vt/2)\right]\psi \\
&= \exp(ivx/2 - iv^2t/8)\sum_n a_n\left[i\frac{\partial u_n}{\partial t} + \frac{1}{2}\frac{\partial^2 u_n}{\partial x_P{}^2}\right] \\
&+ \exp(-ivx/2 - iv^2t/8)\sum_n b_n\left[i\frac{\partial w_n}{\partial t} + \frac{1}{2}\frac{\partial^2 w_n}{\partial x_T{}^2}\right] \qquad \text{(A.4)} \\
&+ \exp(-iv^2t/8)\delta(x-vt/2)\times \\
&\quad \sum_n\left[\exp(ivx/2)a_n\left(\frac{\partial u_n}{\partial x_P} + Z_P u_n\right) + \exp(-ivx/2)b_n Z_P w_n\right] \\
&+ \exp(-iv^2t/8)\delta(x+vt/2)\times \\
&\quad \sum_n\left[\exp(-ivx/2)b_n\left(\frac{\partial w_n}{\partial x_T} + Z_T w_n\right) + \exp(ivx/2)a_n Z_T u_n\right]
\end{aligned}$$

To satisfy Eq. (A.4), the first two terms must be identically zero since the δ functions vanish everywhere except at $x = \pm vt/2$. This condition can be met if we require for u_n and w_n to satisfy the following equations

$$i\frac{\partial u_n}{\partial t} + \frac{1}{2}\frac{\partial^2 u_n}{\partial x_P{}^2} = 0. \tag{A.5}$$

$$i\frac{\partial w_n}{\partial t} + \frac{1}{2}\frac{\partial^2 w_n}{\partial x_T{}^2} = 0. \tag{A.6}$$

The fact that Eq. (A.4) must also be zero at $x = \pm vt/2$ implies the following conditions to hold

$$\sum_n\left[\exp(ivx/2)a_n\left(\frac{\partial u_n}{\partial x_P} + Z_P u_n\right) + \exp(-ivx/2)b_n Z_P w_n\right]_{x=vt/2} = 0. \tag{A.7}$$

$$\sum_n \left[\exp(-ivx/2) b_n \left(\frac{\partial w_n}{\partial x_T} + Z_T w_n \right) + \exp(ivx/2) a_n Z_T u_n \right]_{x=-vt/2} = 0. \tag{A.8}$$

Appendix B

Second Born Approximation

This appendix provides a few details on the derivation of (6.6) from (6.2) and (6.3) in Chapter 6.

The second Born approximation to the transition amplitude in a time dependent approach follows directly from the time independent formulation by replacing the Green's operator $\tilde{G}_0^+$ in (6.3) with the time evolution operator $U(t,t')$. From Eqs. (6.1), (6.2) and (6.3) the transition matrix elements from the initial state ϕ_i (Eq. (5.8)) to the final state ϕ_f (Eq. (5.9)) are given by

$$T_{fi}^{(B2)} = T_{fi}^{(1)} + T_{fi}^{(2)}, \tag{B.1}$$

$$T_{fi}^{(1)} = -i \int dt \langle \phi_f(t) | r_e^{-1} | \phi_i(t) \rangle, \tag{B.2}$$

and

$$\begin{aligned} T_{fi}^{(2)} \;=\; & -\int dt \int_{-\infty}^{t} dt' \times \Big[\langle \phi_f(t) | V_C U(t,t') r_e^{-1} | \phi_i(t') \rangle + \\ & \langle \phi_f(t) | r_e^{-1} U(t,t') V_C | \phi_i(t') \rangle + \langle \phi_f(t) | r_e^{-1} U(t,t') r_e^{-1} | \phi_i(t') \rangle \Big] \end{aligned} \tag{B.3}$$

where

$$U(t,t') = \exp[-i(-\nabla_r^2/2 + H_0(T))(t-t')] \tag{B.4}$$

is equivalent to the Green's operator (6.4) in time domain. Since $U(t,t')$ describes the propagation of the projectile electron in its intermediate state as a free particle while the target electron propagates in the effective target field , it is diagonal in the basis set composed of the product of a plane wave $|\vec{q}\rangle$ and the eigenstate of the target $|n\rangle$. Inserting this basis set into (B.2)

and (B.3) and performing the integration over time as is done in (5.23), one finds

$$T_{fi}^{(1)} = -\frac{1}{\sqrt{2\pi}} i \int d\vec{q} \exp(-i\vec{q}\cdot\vec{b}) \delta(\vec{q}\cdot\vec{v} - v^2/2 - \Delta E) F_{f,i}(\vec{k_f} - \vec{q}) \tilde{\varphi}_i(\vec{q} - \vec{v}) \quad \text{(B.5)}$$

$$\begin{aligned} T_{fi}^{(2)} &= -\tfrac{1}{\sqrt{2\pi}} i \int d\vec{q} d\vec{p} \exp(-i\vec{q}\cdot\vec{b}) \delta(\vec{q}\cdot\vec{v} - v^2/2 - \Delta E) \\ &\quad \times \sum_n \frac{F_{f,n}(\vec{k_f} - \vec{p}) F_{n,i}(\vec{p} - \vec{q})}{k_f^2/2 + \varepsilon_f^T - p^2/2 - \varepsilon_n^T + i\epsilon} \tilde{\varphi}_i(\vec{q} - \vec{v}) \end{aligned} \quad \text{(B.6)}$$

where $\Delta E = k_f^2/2 + \varepsilon_f^T - \varepsilon_i - \varepsilon_i^T$, n is a state label of $H_0(T)$ with eigenenergy ε_n^T and

$$F_{m,n}(\vec{p}) = \left[S_{mn}^T(\vec{p}) - Z_T \delta_{mn} \right] \tilde{V}_c(\vec{p}). \quad \text{(B.7)}$$

S_{mn}^T is the form factor of the target defined as

$$S_{mn}^T(\vec{p}) = \langle m | \exp(-i\vec{p}\cdot\vec{r_T}) | n \rangle. \quad \text{(B.8)}$$

$\tilde{V}_c$ is the Coulomb potential in momentum representation

$$\tilde{V}_c(\vec{p}) = \frac{1}{(2\pi)^{3/2}} \int d\vec{r} \frac{\exp(-i\vec{p}\cdot\vec{r})}{r} = \left[\frac{2}{\pi}\right]^{1/2} \frac{1}{p^2}. \quad \text{(B.9)}$$

The sum over n in (B.6) extends over all the discrete and continuum eigenstates of $H_0(T)$.

$T_{fi}^{(1)}$ and $T_{fi}^{(2)}$ as given by (B.5) and (B.6) are only functions of $\vec{q}_\perp$ because of the δ function. We can rewrite Eqs. (B.5) and (B.6) by integrating over the $\hat{z}$ component of $\vec{q}$ as

$$T_{fi}^{(1)} = -\frac{1}{\sqrt{2\pi} v} i \int d\vec{q}_\perp \exp(-i\vec{q}\cdot\vec{b}) f_1(\vec{q}_\perp) \quad \text{(B.10)}$$

$$T_{fi}^{(2)} = -\frac{1}{\sqrt{2\pi} v} i \int d\vec{q}_\perp d\vec{p} \exp(-i\vec{q}\cdot\vec{b}) f_2(\vec{q}_\perp) \quad \text{(B.11)}$$

where

$$\begin{aligned} \vec{q} &= \vec{q}_\perp + q_0 \hat{z} \\ q_0 &= (v^2/2 + \Delta E)/v, \end{aligned} \quad \text{(B.12)}$$

$$f_1(\vec{q}_\perp) = F_{f,i}(\vec{k_f} - \vec{q})\tilde{\varphi}_i(\vec{q} - \vec{v}), \tag{B.13}$$

and

$$f_2(\vec{q}_\perp) = \int d\vec{p} \sum_n \frac{F_{f,n}(\vec{k_f} - \vec{p})F_{n,i}(\vec{p} - \vec{q})}{k_f^2/2 + \varepsilon_f^T - p^2/2 - \varepsilon_n^T + i\eta}\tilde{\varphi}_i(\vec{q} - \vec{v}). \tag{B.14}$$

From (B.10) and (B.11) the doubly differential cross section can be obtained by integrating over all impact parameters

$$\begin{aligned} \frac{d^2\sigma^{B2}(f)}{dEd\Omega} &= k_f \int d\vec{b} \left| T_{fi}^{(1)} + T_{fi}^{(2)} \right|^2 \\ &= \frac{2\pi}{v^2} k_f \int d\vec{q}_\perp \left| f_1(\vec{q}_\perp) + f_2(\vec{q}_\perp) \right|^2 . \end{aligned} \tag{B.15}$$

Appendix C

Peaking Approximation

This appendix explains the basic concept of peaking approximations used in some places in this thesis.

The purpose of peaking approximations used in present context is to simplify integrals. Assume an integral of the form

$$I = \int dx f(x) g(x) \tag{C.1}$$

whose analytic expression is unknown. However, if one of the functions in the integrand $f(x)$ is strongly peaked at $x = x_0$ and the other one $g(x)$ is smooth around $x = x_0$, then we can approximate the integral (C.1) by

$$I \simeq g(x_0) \int dx f(x). \tag{C.2}$$

The Dirac δ function is a well-known example of this kind, i.e., $f(x) = \delta(x - x_0)$, then $I = g(x_0)$. This concept can be readily generalized to spaces of arbitrary dimensions.

Another example can be found in deriving (5.24) from (5.23). Since $\tilde{\varphi}_f^{-*}(\vec{p})$ in (5.23) is strongly peaked at $\vec{p} = \vec{k_f} - \vec{v}$, we can set $T_{fi}(\vec{p} + \vec{v}, \vec{p} + \vec{v} + \vec{q} - \vec{k_f})$ at $\vec{p} = \vec{k_f} - \vec{v}$ and pull it out of the integral on $\vec{p}$,

$$\begin{aligned} a_{fi}^{IA}(b) &= -2\pi i \exp(i\vec{k_f} \cdot \vec{b}) \int d\vec{q}\, \delta(\vec{q} \cdot \vec{v} - (k_f^2 + v^2 - 2\varepsilon_i)/2) \exp(-i\vec{q} \cdot \vec{b}) \\ &\quad \times T_{fi}(\vec{k_f}, \vec{q}) \int d\vec{p}\, \tilde{\varphi}_f^{-*}(\vec{p}) \tilde{\varphi}_i(\vec{p} + \vec{q} - \vec{k_f}) \end{aligned} \tag{C.3}$$

$$= -2\pi i \exp(i\vec{k_f}\cdot\vec{b}) \int d\vec{q}\,\delta(\vec{q}\cdot\vec{v} - (k_f^2 + v^2 - 2\varepsilon_i)/2) \exp(-i\vec{q}\cdot\vec{b})$$
$$\times T_{fi}(\vec{k_f}, \vec{q}) S_{fi}^P(\vec{q} - \vec{v}). \qquad \text{(C.4)}$$

Eq. (C.4) is just (5.24).

Appendix D

Dalitz Integral

It can be shown [90] that the general three-dimensional Dalitz integral

$$I_{m,n} = \int d\vec{p} \frac{1}{p^2 - k^2 - i\eta} \frac{1}{[\alpha^2 + (\vec{p} - \vec{A})^2]^m [\beta^2 + (\vec{p} - \vec{B})^2]^n} \tag{D.1}$$

can be reduced to a one dimensional integral of the form

$$I_{m,n} = \frac{(m+n-1)!}{(m-1)!(n-1)!} \int_0^1 t^{m-1}(1-t)^{n-1} K_{m+n}(t) dt \tag{D.2}$$

where K_l are defined as

$$K_1 = \frac{i\pi^2}{x} \log \left[\frac{k + x + iy}{k - x + iy} \right], \tag{D.3}$$

$$K_l = -\frac{1}{2(l-1)y} \frac{\partial K_{l-1}}{\partial y}, \; l \geq 2 \tag{D.4}$$

with x and y given by

$$x = |t(\vec{A} - \vec{B}) + \vec{B}|, \tag{D.5}$$

$$y = \alpha^2 t + (1-t)(\beta^2 + t|\vec{A} - \vec{B}|^2). \tag{D.6}$$

In our case (Chapter 6) the relevant type of integral can be identified by substituting (6.22) into (6.19). Then the sum (6.19) consists of terms of the form

$$I_{1,2} = \int d\vec{p} \frac{1}{p^2 - k^2 - i\eta} \frac{1}{[\alpha^2 + (\vec{p} - \vec{A})^2] [\beta^2 + (\vec{p} - \vec{B})^2]^2} \tag{D.7}$$

with $n = 1$ (due to $\tilde{V}_c$) and $m = 2$ (due to S_{fi}^T). It is clear from (D.2) that the explicit expression for K_3 is required. Differentiating K_1 twice with respect to y yields

$$K_3 = \frac{\pi^2}{4} \frac{3y^2 + x^2 - k^2 - 4iky}{y^3[k^2 - x^2 - y^2 + 2iky]^2}. \tag{D.8}$$

Since x and y (Eqs. (D.5) and (D.6)) are functions of t, K_3 is also a function of t. Finally, $I_{1,2}$ follows from (D.2)

$$I_{1,2} = 2 \int_0^1 (1 - t) K_3 dt. \tag{D.9}$$

Curriculum Vitae

Jianyi Wang was born on Sep. 12, 1962 in a rural village of Rushanzhai, Shandong province, P.R. China. He is the youngest in the family of five, with one brother and one sister.

He graduated from high school in 1979. With the strong encouragement of his whole family, he spent the entire summer of that year preparing for the national college entrance examination. He passed the examination at the end of a long sweaty summer and became one of the lucky 7% of all high school graduates in the country that year to be accepted by colleges and universities nationwide. In the fall of 1979 he chose to enter Lanzhou University located in the north-west part of the country (geographically at the center of China in the middle of the historically famous silky way), some 2,400 kilometers ($\sim$ 1,500 miles) away from home. He obtained the bachelor of science degree in August 1983 majoring in nuclear physics. After about one year of training in spoken English at Lanzhou University (LU), he embarked on a long journey to study at the University of Tennessee (UT) in October 1984 through an exchange program coordinated by Dr. Jingye Zhang of LU and Dr. Lee Riedinger of UT. In early 1987 he joined the theoretical atomic physics group of Dr. Joachim Burgdörfer at the department of physics and pursued research in the theory of atomic collisions. He expects to receive his Ph.D. in physics from the University of Tennessee in December, 1991.